POLITECNICO
MILANO 1863

SCUOLA DI INGEGNERIA INDUSTRIALE
E DELL'INFORMAZIONE

A preliminary study on the prediction of as-built surface quality in complex L-PBF parts using thermal imaging-based in-situ monitoring

TESI DI LAUREA MAGISTRALE IN
MANAGEMENT ENGINEERING
INGEGNERIA GESTIONALE

Authors: **Antonio SCARPITTI**
Elena Luna TOCCI

Student IDs:	944892
	953444
Advisor:	Professor Bianca Maria COLOSIMO
Co-advisor:	PhD Candidate Matteo BUGATTI
Academic Year:	2020-2021

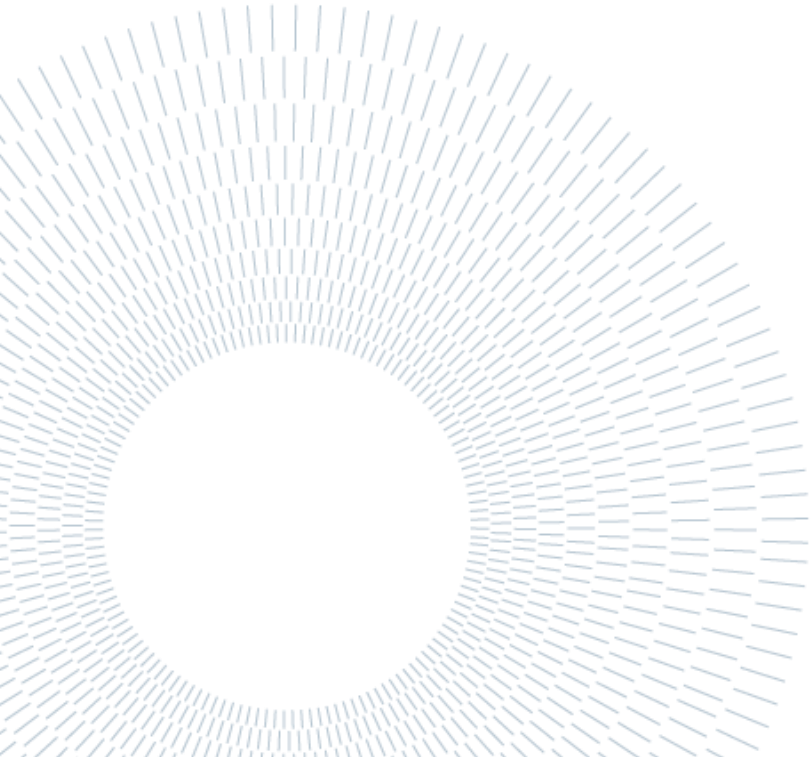

Abstract

Additive Manufacturing (AM) has gained an extreme importance in the recent years in the production of metal components, especially in the medical and aerospace sectors. However, the mechanical components used in these industries have to comply with very specific quality standards in terms of final surface roughness, which are not yet reachable with the current AM technologies.

The major challenge that AM is attempting to address is the in-time control of the production with the aim of keeping monitored the final surface quality of the printed part and reducing the post-processing operations. The current literature recognizes the influence of two important characteristics on the roughness formation mechanism of downskin surfaces, respectively the angle of inclination and the thermal stresses caused by the high temperatures registered during the printing process. What it is still unexplored is how to directly link the in-situ thermal signature with the ex-post surface roughness.

This thesis strives to address this limitation by analyzing the Time Above Threshold (TAT) indication of specific areas on the surface, i.e. the amount of time each point shows a temperature higher than certain limits. This new indicator is used as input variable of a proposed regression model with the purpose of estimating the expected value of roughness. The novelty is represented by the combination of both indicators, a design one (the value of inclination) and an in-situ one (TAT) to assess the final surface quality. The impact of this novel indicator is tested on two different materials, AISI 316L and AlSi10Mg to validate the analysis.

The last part of the work is dedicated to an experimentation conducted on samples printed again with AlSi10Mg but using different scan strategies. The idea is to induce different thermal properties and analyze how the thermal indication influences the final quality of the part.

Key-words: L-PBF; In-situ monitoring; Surface roughness; Thermal imaging.

Sommario

Nel corso degli ultimi anni, la Manifattura Additiva (AM) ha raggiunto una notevole importanza per quanto riguarda la produzione di componenti metallici, in particolar modo nell'ambito medico ed aerospaziale. Tuttavia, le parti meccaniche impiegate in questi settori devono rispettare standard di qualità molto stringenti in termini di rugosità superficiale, non ancora interamente conseguiti dalle tecnologie AM esistenti.

La sfida principale con cui la Manifattura Additiva deve confrontarsi è il controllo della produzione in tempo reale, con l'obiettivo di monitorare la qualità superficiale finale dei prodotti stampati, e ridurre così le lavorazioni post-produzione. Le caratteristiche trovate in letteratura che influenzano maggiormente la formazione di rugosità sulle superfici sporgenti riguardano l'angolo di inclinazione e gli stress termici causati dalle alte temperature di lavorazione. La diretta relazione tra la firma termica del processo e la rugosità finale del prodotto, invece, rimane ancora inesplorata.

Il presente lavoro di tesi si pone l'obiettivo di colmare questa limitazione analizzando il parametro di Time Above Threshold (TAT) di una specifica area superficiale, ovvero il tempo in cui i punti analizzati mantengono una temperatura più alta della soglia fissata. Questo indicatore è usato come variabile di input del modello di regressione proposto, con l'intento di stimare il valore di rugosità previsto. L'innovazione è espressa dalla combinazione di entrambi gli indicatori, il dato progettuale (il valore di inclinazione) e di produzione (TAT) per valutare così la qualità superficiale finale. La significatività di questo indicatore è verificata su due materiali differenti, AISI 316L and AlSi10Mg.

L'ultima parte del lavoro è invece dedicata a una sperimentazione eseguita su dei provini in AlSi10Mg, differenziandosi dai precedenti tramite diverse strategie di scansione. La finalità è di indurre proprietà termiche diverse e analizzare come l'indicatore termico influenza la qualità finale del prodotto.

Parole chiave: L-PBF; Monitoraggio in-situ; Rugosità superficiale; Termografia.

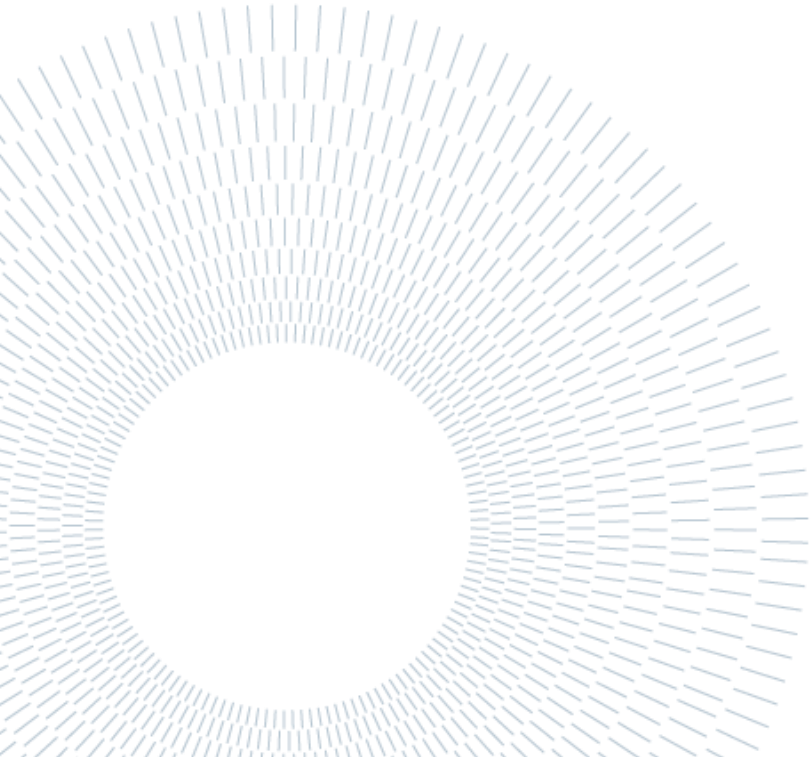

Contents

Introduction

The strong importance and the large adoption of the Additive Manufacturing technologies are mostly due to their great advantages respect to traditional production processes. These technologies enable an intense reduction of raw materials, the possibility to produce particular geometries and a simplification of the steps necessary for the production itself.

The combination of these features has ensured that the applicability and the endorsement of AM processes embraced an ever-increasing number of sectors, first of all the aerospace one where the typical productions include complex and intricate structures. These parts have to respect precise quality standards, particularly with regard to the final surface roughness. This defect is very challenging especially in the down-facing areas which typically present the as-built roughest surfaces, for two main causes: the stair-stepping effect and the influence of gravity (defect known as sagging).

Post-processing operations are meant for reducing these surface imperfections: the principal ones are heat treatment, polishing and milling. The main drawbacks regard their high cost and the risk of reducing the mechanical properties of the printed parts. The final goal of Additive Manufacturing is then to reduce as much as possible the adoption of these post-treatment activities and to obtain as-built parts more and more performant. It is fundamental to keep in control the on-going production by monitoring some in-situ parameters which can be directly correlated to the final surface roughness.

Different factors have an effect on the resulting final quality of the downskin surfaces, such as the inclination of the surface itself and the heat effects caused by the abrupt changes in temperature during the production. The focus is both on the first characteristic (a design parameter) and on the in-situ thermal feature.

The objective of this work is the finding of a direct correlation between such indications and the registered ex-situ roughness, with the aim of keeping it monitored during the production in progress. The main goal is how to compare the two information by exploiting regression models. The experimentation is conducted on 4 L-PBF printed samples, each one with a different value of

inclination. The adopted materials are two: a stainless-steel powder (AISI 316L) and an aluminum alloy (AlSi10Mg).

The Thesis is organized as follows:

Chapter 1 presents an overview of Additive Manufacturing and the techniques exploited in this field, with a focus on Laser Powder Bed Fusion. The main defects that can originate from the process are also illustrated.

Chapter 2 provides an analysis on the current literature of L-PBF on three main topics: surface roughness, how it is influenced by process parameters and overhang angles, in-situ monitoring, to understand the utilized techniques, and lastly how the correlation between the two has been explored.

Chapter 3 illustrates the details of the experiments executed in this Thesis, the used machinery and the adopted tools.

Chapter 4 is the core section of the work in which the data analysis procedure is explained. The main phases regard the data acquisition, the data cleaning, and the extraction of the necessary parameters. Finally, the results of a statistical investigation are presented and correlated.

At the end the major conclusions and future works are reviewed.

1 Background Knowledge

1.1. Additive Manufacturing

By quoting the words of ASTM International, Additive Manufacturing can be defined as "the process of joining materials to make objects from 3D model data, usually layer upon layer, as opposed to subtractive manufacturing methodologies". (Yakout et al., 2018)

Even though the two terms are used as synonyms, Additive Manufacturing (AM) and Rapid Prototyping (RP) have a peculiar difference: AM in fact can be considered an evolution of the RP, born in 1980 with the aim of creating physical prototypes of products, before the release of the original part on the market. In the recent years, the improvements in the final quality of this type of production permitted to directly produce the final product with this technology. For this reason, the term Additive Manufacturing seems to be more appropriate and commonly accepted (Gibson et al., 2015).

The production of a part through AM can be divided in 3 main phases (Calignano et al., 2019), (Abdulhameed et al., 2019):

1. The design phase, which encompasses the creation of the 3D CAD model of the product and the conversion in a file format readable by AM machines (STL format).
2. The production or manufacturing phase, comprehending the preparation of the machine, the determination of optimal parameters and the printing itself.
3. Lastly, the post-processing step, in which some heat treatments and finishing of the product can be performed.

In the recent years, AM gained more and more importance because of its main advantages respect to traditional manufacturing processes. This new technology allows to significantly reduce the number of resources and the steps or processes necessary for the production, meaning benefits in terms of weight of material used, a strong reduction in the wastes and a simplification of the supply chain (Gibson et al., 2015). For this reason, AM is considered a principal enabler for the realization of a circular economy (Hettiarachchi et al., 2022).

The benefits are then amplified considering the flexibility of AM: it permits to frequently change the design of the parts and to produce pieces with very complex geometries (Abdulhameed et al., 2019), (Bhuvanesh Kumar & Sathiya, 2021). These advantages enabled AM processes to become extensively used in an ever-increased number of sectors, such as the aerospace, medical, automotive and defense (Schoinochoritis et al., 2017), (Calignano et al., 2019), as represented in Figure 1.1.

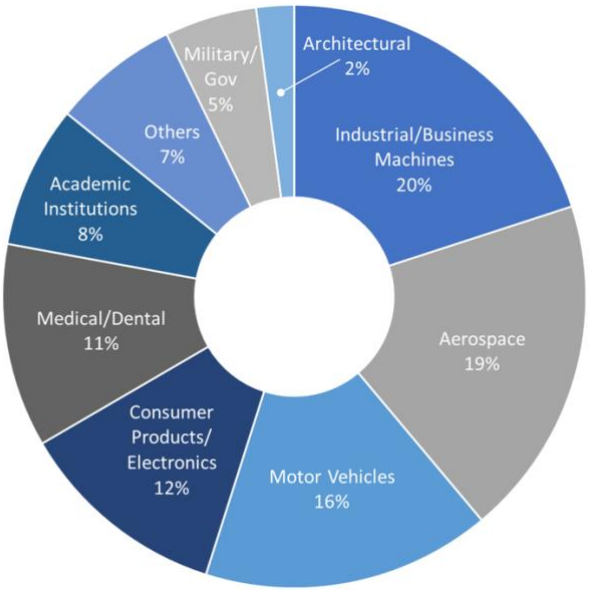

Figure 1.1: AM applications by sector (Wohlers et al., 2018)

This trend, as visible in Figure 1.2, is expected to grow more and more: from 2013 to 2019, the AM market size showed a percentage increase higher than 295%. Forecasts indicate that this market size will reach a global value of USD 23.75 billion by 2027 (Research and Markets, n.d.).

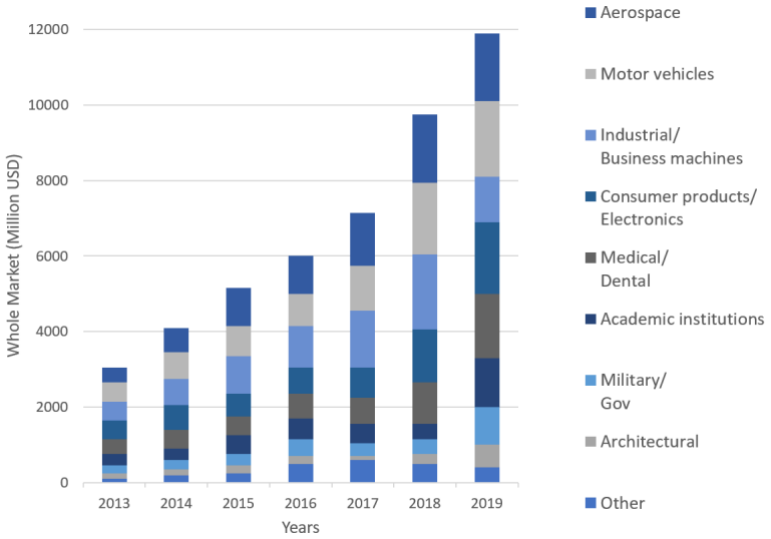

Figure 1.2: AM market size by sector (Tan et al., 2021)

In the literature, different classifications of the AM processes can be found: some insist on the difference between the base material (ceramic, metals, polymers), others on the state of the raw materials input (solid, liquid, powder) (Yakout et al., 2018), (Gibson et al., 2015).

By following the same division of ASTM International, AM technologies can be branched in 7 categories: Binder Jetting, Direct Energy Deposition (DED), Material Extrusion, Material Jetting, Powder Bed Fusion, Sheet Lamination and Vat Photopolymerization.

1.2. AM Techniques and L-PBF

In this section, the 7 technologies of the AM proposed by ASTM International are briefly presented (Figure 1.3). Although, the focus is on the Laser-Powder Bed Fusion (L-PBF), since it is the type of process used in the experimental analysis.

Binder Jetting: in this processing, a liquid polymer (binder) is injected over a powder bed, allowing the particles to agglomerate, resulting in a cross-section of the final part. The powder is then re-spread to create the successive layer. Even though it is a flexible process, as it permits to use many different materials, the produced products are characterized by a high level of porosity (Gao et al., 2015).

Direct Energy Deposition: DED consists in the printing of final part by simultaneously melt the material while it is being deposited. The heat source could be either a laser or electron beam, while the typical materials are metallic powder or wire (Milewski, 2017).

Material Extrusion: production layers are created through the extrusion of semisolid material which flows out from a nozzle (Wiberg, 2019). To properly eject the material, high temperatures are required but, at the same time, once expelled, the material has to rapidly solidify. The main drawback is on the final quality of the part: products printed with this technology show a high rate of porosity (Gao et al., 2015).

Material Jetting: it can be considered an evolution of the most common 2D ink-jet printing (Wiberg, 2019). In this case, the material (being it vax or photopolymer, in the form of droplets) is directly store on a baseplate. The viscosity of such materials is typically low and the droplets are subjected to a liquid-solid phase change thanks to photopolymerization (Gao et al., 2015). The wide adoption of this kind of production is mainly due to the low costs, however at the expenses of a low part accuracy (Gibson et al., 2015).

Sheet Lamination: the production takes place through ultra-thin metal sheets. Each layer corresponds to a new sheet of metal where the edge of the part cross-section is cut with the aid of a laser. Since its market introduction, the major advantages were clear: a precision for surface details and a lower cost for the production (Gao et al., 2015).

Vat Photopolymerization: this technology starts with a liquid (a polymer) which is contained inside a vat. At each step (thus each layer) a UV light hits the liquid which undergoes a phase change, solidifying and attaching to previously printed material (Gibson et al., 2015). Vat Photopolymerization is widely used because of its high production rate, but at the same time, it requires expensive materials and supplies.

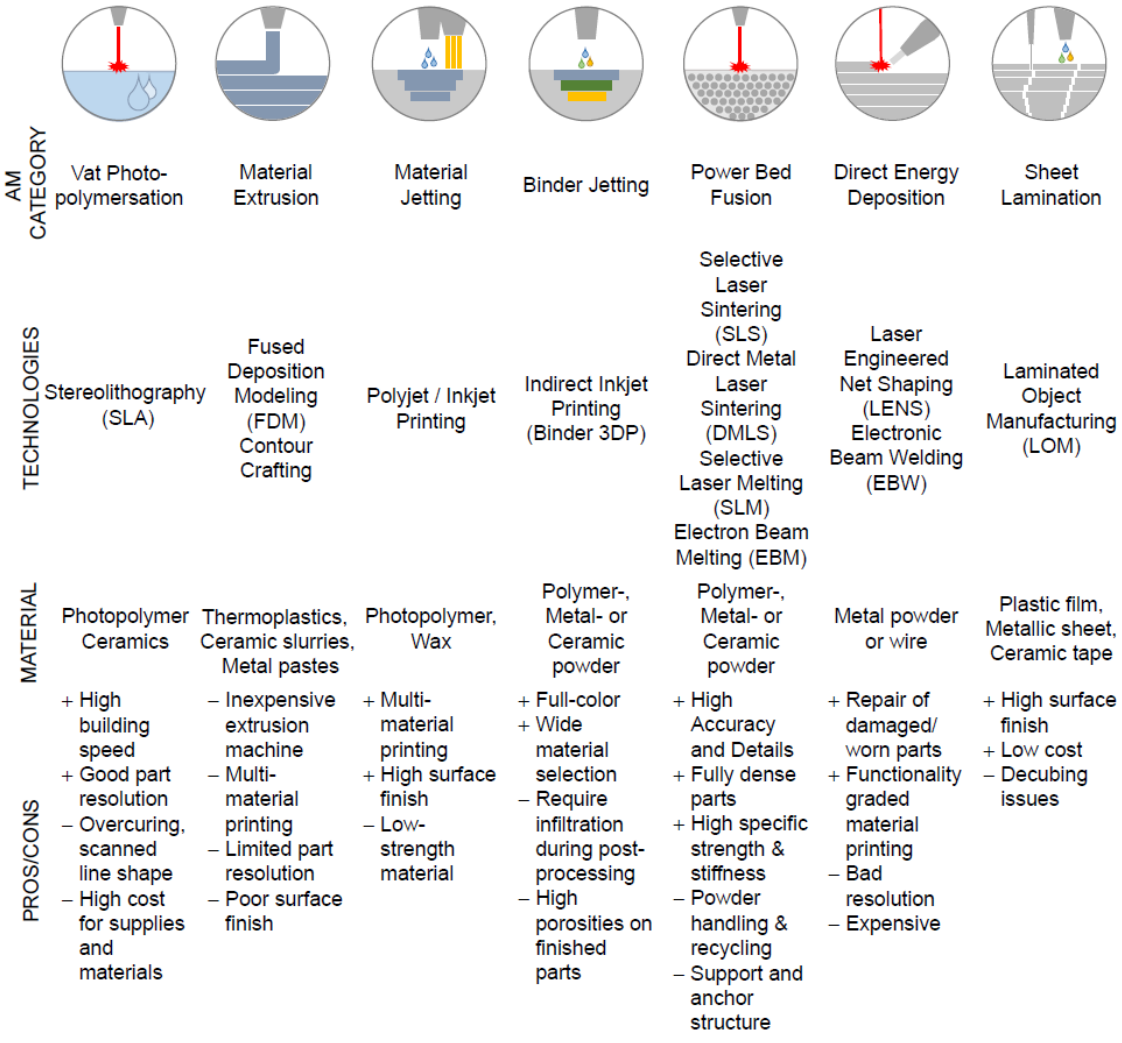

Figure 1.3: Main characteristics of AM techniques (Wiberg, 2019)

Powder Bed Fusion (PBF) needs a special attention because it is the type of technology used in the experimental part of this thesis. In general, PBF can be branched in two macro groups, depending on the energy source used: on the one hand the Electron Beam Melting (EBM) which uses an electron beam, while on the other hand Selective Laser Melting (SLM) or Selective Laser Sintering (SLS), using instead a laser beam.

All PBF processes occur in a build chamber, treated with inert gases (typically Argon or Nitrogen) to avoid material oxidation and to protect the melt. The first step of every PBF process is the spread of a thin layer of powder, in the order of 20 μm – 100 μm, (Herzog et al., 2016) over the build platform. This is possible thanks to a tank which contains the powder and a roller (or recoater blade) which distributes uniformly and smooths out the powder. Then, the thermal source, being it electron or laser beam, hits the powder particles inducing the material to melt or sinter. Once the layer is completed, the baseplate is pulled down of a height equal to the layer thickness and the process is repeated for successive layers. The general architecture of a PBF process is reported in Figure 1.4.

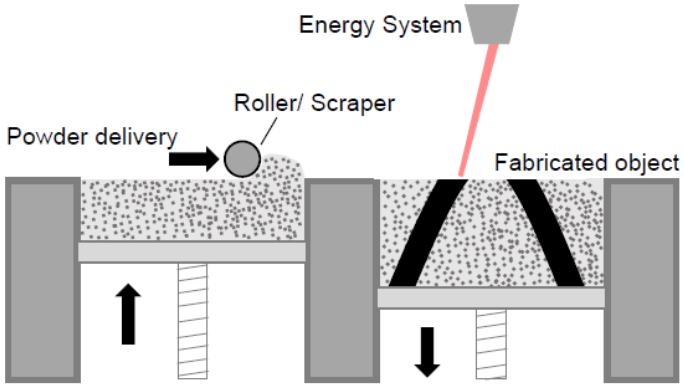

Figure 1.4: A general PBF process architecture (Wiberg, 2019)

It is useful to highlight that Laser source PBF (L-PBF) processes have different machines respect to electron ones, especially in terms of energy system architecture. Moreover, L-PBF is experiencing a remarkable adoption in the recent years, as it allows to produce very precise pieces with fine details (Wiberg, 2019).

L-PBF is also the typology of production used in the present Thesis. Given these premises, a little focus on its main characteristics is hereafter presented. It is possible to recognize four different categories of process parameters (Milewski, 2017), (Kurzynowski et al., 2012):

1. Laser-related parameters, comprehending the laser power, the spot size (or beam diameter) and the wavelength, influencing the absorption of the material.
2. Scan-related parameters: the scan speed, which is the velocity of the laser moving over the surface, the scan pattern and lastly the scan spacing, the gap between two adjacent scans.
3. Powder-related parameters, which refers to all those characteristics of the powder itself, such as the particle size, the layer thickness, the powder shape and distribution. All those quantities have a strong influence on the final density of the material.
4. Atmosphere-related parameters: since the process is extremely sensitive, the atmosphere is carefully controlled through the adoption of inert gases, a low level of oxygen and given temperatures.

1.3. Defect in AM

Among the different Metal Additive manufacturing technologies, the Powder Bed Fusion is one of the most studied in the literature, given its wide applicability in manufacturing products for different fields and sectors. Its increasingly constant use is to be sought in the possibility of producing complex pieces with extreme precision and efficiency.

Various defects can arise in Powder Bed Fusion processes which may reduce the quality of the produced parts. To overcome those issues, two main approaches can be adopted:

1. Applying post processing techniques to reduce the irregularities on the finished piece, e.g., blasting (Mohammadi & Asgari, 2018).
2. Adjusting the process parameters, e.g., laser power, scan speed, hatch distance (Guo et al., 2020).

Before correcting the defects, it is necessary to understand what types exist and how they differentiate. By following a categorization from internal to external, in the next paragraphs the main defects found in PBF, identified by Grasso & Colosimo, (2017), are described.

Porosity

Porosity (Figure 1.5) is one of the most common issues in PBF and it is a frequently addressed argument since it has considerable consequences in the mechanical

properties of the part (DebRoy et al., 2018), e.g., the fatigue performances. According to Eskandari Sabzi, (2019), porosity can be branched in four classes: (1) process induced, (2) gas entrapped, which gives a spherical shape to the pores, (3) evaporation-caused and (4) lack of fusion, due to the molten pool that does not penetrate the lower levels below the current layer. The process parameters can highly influence their formation and to have a comprehensive value that can represent laser power, scan speed, hatch spacing and layer thickness, the volume energy density is often calculated. Pores formed by lack of fusion can be reduced with a higher volume energy density, which is favorable since it permits to create a stronger bond between layers and track, as it is reported in the study by Guo et al., (2020).

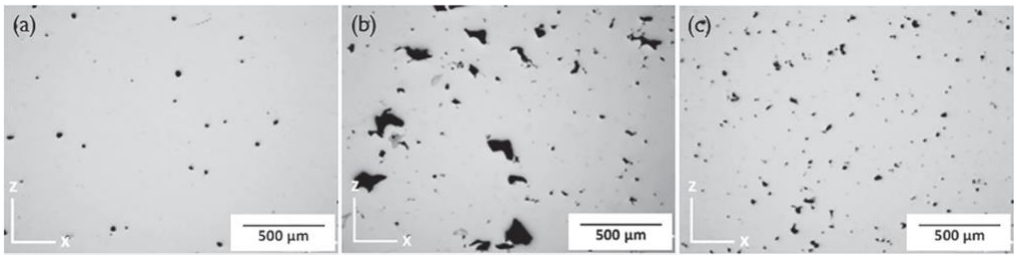

Figure 1.5: (a) Represents the gas entrapped pores, (b) shows the evaporation-caused pores and (c) represents the lack of fusion pores (Eskandari Sabzi, 2019)

Residual stresses, cracking and delamination

Residual stresses are "elastic stresses that remain within a part after the load is removed" (Gunenthiram et al., 2018). They originate for the reason depicted by Bartlett & Li, (2019): non-uniform thermal loads. When fast and consecutive heating and cooling phases are performed, the thermal gradient is significant (Calignano & Minetola, 2019) and it causes a non-uniform plastic deformation of the part, e.g., when the plastic limit is exceeded. To mitigate their presence, DebRoy et al., (2018) shows that a preheat of the substrate is very efficient, as it lowers the difference of temperature.

Furthermore, cracking (Figure 1.6a, b) can happen as consequences of thermal stresses. In the review by DebRoy et al., (2018) is described that, when a new layer is built during the additive manufacturing, its temperature is higher than the layer beneath it. They both thermically contract, but the shrinkage of the lower layer is less strong, and it impedes the metal just deposited. This creates tensile stress that, if it outpaces the strength of the superior layer, develops cracks.

Ultimately, as a particular type of cracking, delamination (Figure 1.6c) appears when two successive layers detach from each other (DebRoy et al., 2018).

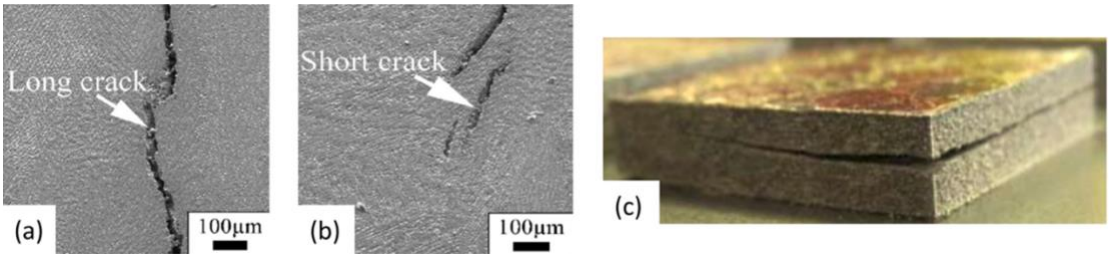

Figure 1.6: (a) Long crack, (b) short crack, (c) delamination (DebRoy et al., 2018)

Defects concerning the microstructure

According to Malekipour & El-Mounayri, (2018), the defects that impact on the microstructure are: heterogeneity, which depends by many factors, as the condition of the powder, the scan strategy used, or the alterations in temperature; and anisotropy. The latter regards the condition of showing on the surface specific characteristics that depend on the measurement direction (*Anisotropy*, n.d.). It is strictly related to the scan strategies and the orientations of the layers.

Another source of issues regards the surface oxidation, which could increase because of the ambient atmosphere during the process, or because of the metallic powder contaminations, which quality depends on the storage and handling conditions. Powder has to be examined before production, particles need to be of the accurate shape and no impurities or moisture have to be detected (Mandache, 2019).

Geometry defects and dimensional accuracy

In PBF, defects can develop geometrical inaccuracies in the printed piece, and one of the most common imperfections that reduces the accuracy is frequently called "edge effect" (Metelkova et al., 2019), or superelevated edges (Figure 1.7). It has many negative consequences, e.g., it obstacles the formation of the new layers and it may ruin the recoater blade as well, which originates striations on the powder bed surface. This printing defect can be removed in-situ through subtractive processes as laser ablation, refilling and remelting (Fleming et al., 2020). Other geometrical defects are shrinkage, warping and curling.

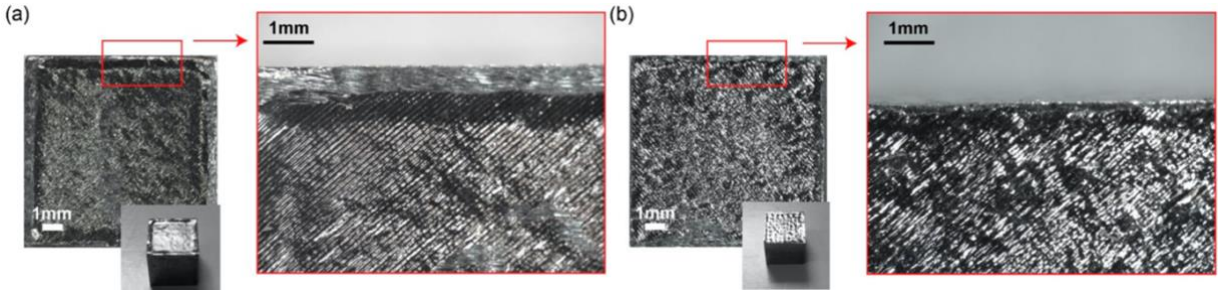

Figure 1.7: (a) Raised edges in the up-skin surface, (b) no defects in the up-skin surface (Calignano & Minetola, 2019)

Surface defects

A surface is composed by different frequencies that characterize form, waviness (macro geometrics) and roughness (micro geometrics). Respectively they regard low, medium, and high frequencies. It is important to differentiate and separate them within the roughness analysis, to not miscalculate its evaluation (Sahay & Ghosh, 2018).

Surface roughness can be originated mainly in two circumstances (DebRoy et al., 2018): (1) due to the "**stair step effect**", and (2) due to the incorrect melting of the metal powder which causes an irregular surface.

The stair-stepping effect (Figure 1.8) is as result of the layered nature of the additive manufacturing techniques, and it is even more accentuated both in up-facing and down-facing surfaces (Yasa et al., 2016). It increases with the layer thickness; on the other hand, the production time comes to be longer if the height is reduced. This phenomenon is more evident if the angle of inclination of the surface is steep (DebRoy et al., 2018).

Surface roughness is also provoked by a low scanning power and high scanning speed, which implies low energy input that is not enough to completely melting the metal (DebRoy et al., 2018).

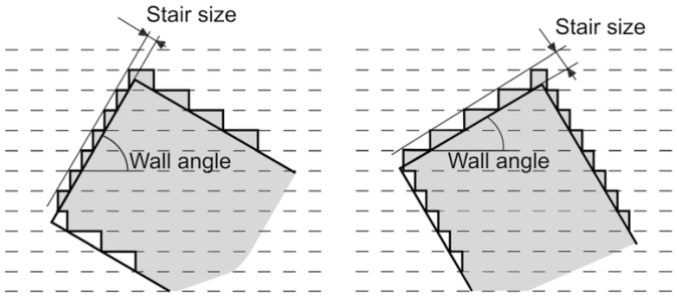

Figure 1.8: "Stair step effect" (Simoni et al., 2021)

These same causes also originate a further defect on the surface, which is balling. During the PBF printing, when the small region of metallic powder under processing melts, it creates a so-called melt pool, and while the laser beam moves along the surface path, a molten track is formed. The latter develops an elongated, cylindrical shape which is not always stable during the process. When the track collapse, the **balling phenomenon** (Figure 1.9) occurs, which consists in disconnected bulbs along the path (Skalon et al., 2020). The cause of this formation is explained by Gunenthiram et al., (2018) as lack of melting of the melt pool with the substrate that originates spheres on the surface due to the surface tension. Again Skalon et al., (2020) specifies that the balling regime develops in conditions of low volume energy density.

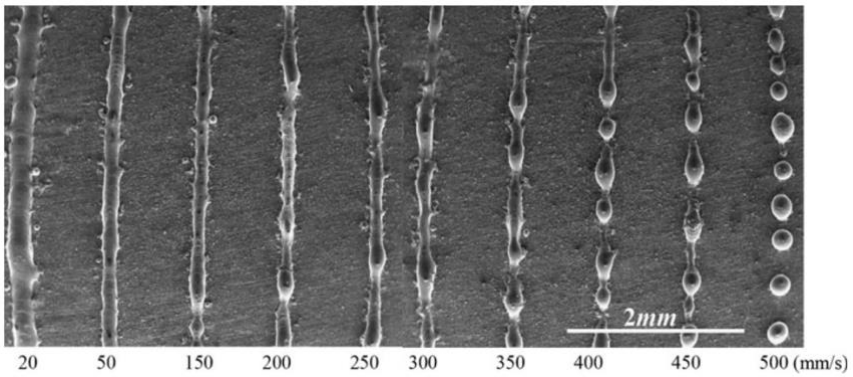

Figure 1.9: Balling phenomena (Ruidi Li et al., 2012)

A further cause is (3) **sagging** (Figure 1.10), which occurs when the inclination angle of the surface overcomes the critical angle of 40°- 45° and the powder drops downwards due to gravity (Çalışkan et al., 2021). This could be avoided with the use of supports, but they are not the best approach since removing them could be difficult and it could likewise induce roughness. The preferred alternative is to investigate the combination of printing parameters that could reduce this effect, as the ones with lower energy density.

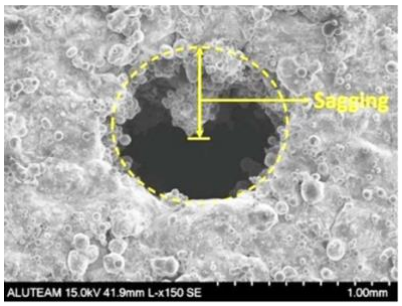

Figure 1.10: Sagging (Çalışkan et al., 2021)

Additionally, surface defects can be originated also by (4) **dross formations** (Figure 1.11), meaning "excess material that is present on overhangs caused by excessive melting as a result of overheating within the down-facing area" (Charles, Elkaseer, et al., 2021). This causes a dimensional inaccuracy respect to the desired design and further problems that can derive from that, as lower performances. The reason why dross arises is a too high linear energy density on the overhang structures with respect to the one used for the bulk (Charles, Bayat, et al., 2021).

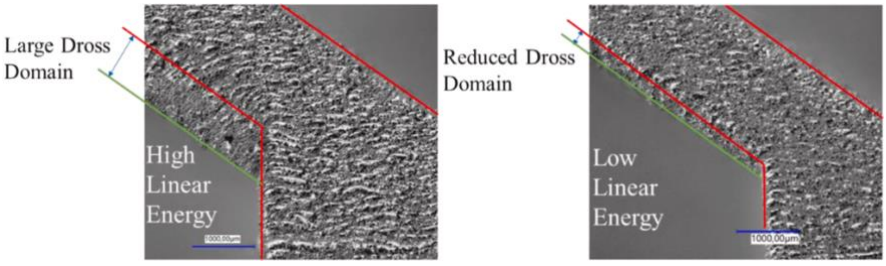

Figure 1.11: Dross formation (Charles, Bayat, et al., 2021)

1.4. Aim of the Work

The present work focuses on one of the most critical problems of the Powder Bed Fusion methodology, the final surface roughness of the printed parts.

The main areas of application of this technology are the aerospace (Seabra et al., 2016) and the biomedical one (Mohammadi & Asgari, 2018), sectors in which the final quality of the pieces is extremely fundamental, having very strict quality standards. Several defects affect the final quality of the printed products, but the one with the greatest influence is the final surface roughness (Rott et al., 2020). The roughness itself has a direct negative effect on the fatigue life of the mechanical parts. The work proposed by Mohammadi & Asgari, (2018) showed that a high surface roughness provokes an increase of the subsurface porosity, which, together with the roughness, is considered the main sites for fatigue crack initiation and propagation.

On the one hand, the final surface roughness could be drastically reduced with some post-process techniques, such as heat treatment (Simoni et al., 2021), milling (Rott et al., 2020) or polishing (Mumtaz & Hopkinson, 2009). The problem of these post-processing activities is their excessive cost and time. Especially in the aerospace sector, it is extremely difficult to obtain complex geometries with a relatively low roughness, as they typically include intricate internal structures. 3D printed parts used in space applications must verify strict precisions reaching an

almost zero roughness level. However, the post processing cleanliness not only cannot be always performed for complex parts since support removal and trapped powders removal can be very challenging (Blakey-Milner et al., 2021), but it also risks to reduce the fatigue life of the produced pieces (Rott et al., 2020), (Mohammadi & Asgari, 2018).

For this reason, with the aim of reducing these post-processing operations to a minimum, the latest concerns of Additive Manufacturing are about the in-time control of the surface roughness by monitoring it in real time. Furthermore, the final surface roughness is known to be widely dependent on the thermal stresses caused by the high temperatures recorded during the production, especially in the case of overhang regions (Feng et al., 2021).

This work has a similar purpose, wanting to understand some possible correlations between in-situ parameters and post-processing (or ex-situ) resulting roughness. In fact, if on the one hand this influence is commonly recognized, the literature still lacks a direct correlation between the two dimensions. The main object is to connect some parameters registered while the part is being scanned through a thermography analysis with the final surface roughness. The idea is that these real-time parameters could give an insight of how the final quality of the part will be. The chosen process signature is the Time Above Threshold (TAT), given that from the analysis of the roughness forming mechanisms, a correlation between thermal gradients and this defect seems evident. Then, it is fundamental to directly connect the ongoing production with the final quality of the buildings.

2 State of the Art

2.1. Ex-Situ

The current section will follow a division which considers the characteristics of the roughness presented in Section 1.3. As previously mentioned, this micro defect is highly dependent on the angle of inclination, which is the angle formed between the build direction and the vertical plane, indicated as α in Figure 2.1.

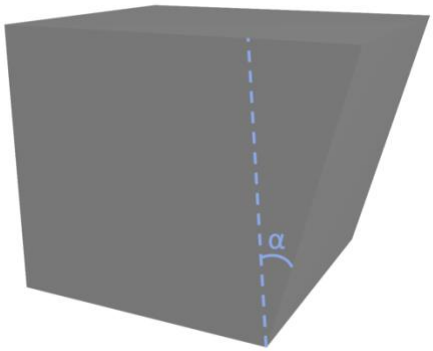

Figure 2.1: Example of angle inclination of a 3D printed specimen

Since part of the focus of this research work is on the analysis of the roughness, it is essential to comprehend how the current literature is tackling this subject. In addition, it is fundamental to understand the role of the printing parameters, such as scanning speed, hatch spacing, scan strategy and so on. Indeed, the influence of these parameters on the resulting roughness is widely demonstrated in the literature.

For this reason, two different subparagraphs will be developed. The first one, which mainly focuses on the role of the process parameters on those mechanical parts which are printed without any inclination. Both fixed and varying parameters will be considered.

The second one, instead, seeks to understand the influence of the inclination of the finished part on the surface roughness. Different orientations are present in the literature, some of which (those with a slope higher than 45°, according to Charles

et al., (2019), or higher than 60°[1], as stated by Fox et al., (2016)) require the presence of supports for a proper print. In this case as well, the impact of the scanning parameters will be analyzed.

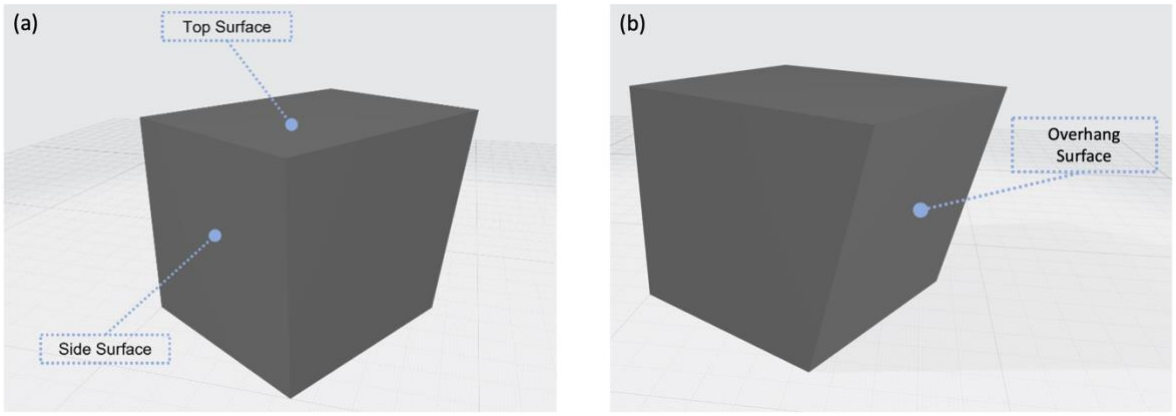

Figure 2.2: Example of (a) not inclined surfaces (top surfaces and side surfaces) and (b) inclined surfaces (overhang surfaces)

In Table 2.1, the analyzed studies are clustered in different common categories. The categorization was according to the angle of the surfaces under study and the parameters used in the process. For this latter division, in the specific, the following quantities are considered:

- Laser parameters: laser power [W], laser pulse energy [J], laser pulse duration [ms] and/or beam/laser spot diameter [μm].
- Scan parameters: scan speed [mm/s], hatch spacing [μm], surface energy density [J/mm^2] and/or volume energy density [J/mm^3].
- Angle parameters: scanning angle [°], angle between surface orientation and/or laser incidence [°].

[1] Angle formed between the vertical plane and the inclined surface. All the angles in this work are coherent with this interpretation.

	Top surface 90° (not inclined)	Side surface 0° (not inclined)	Downskin
Laser parameters	(Guo et al., 2020) (Mohammadi & Asgari, 2018) (Mumtaz & Hopkinson, 2009) (Simoni et al., 2021) (DePond et al., 2018) (Yan et al., 2021)	(Mumtaz & Hopkinson, 2009) (Simoni et al., 2021) (Yan et al., 2021) (Feng et al., 2021)	(Yang et al., 2021) (Simoni et al., 2021) (Koutiri et al., 2018) (Fox et al., 2016) (Feng et al., 2021) (Charles et al., 2019)
Scan parameters	(Guo et al., 2020) (Mohammadi & Asgari, 2018) (Fleming et al., 2020) (Mumtaz & Hopkinson, 2009) (Simoni et al., 2021) (DePond et al., 2018) (Yan et al., 2021)	(Mumtaz & Hopkinson, 2009) (Simoni et al., 2021) (Yan et al., 2021) (Feng et al., 2021)	(Yang et al., 2021) (Simoni et al., 2021) (Koutiri et al., 2018) (Fox et al., 2016) (Feng et al., 2021) (Charles et al., 2019)
Angle parameters	(DePond et al., 2018)		(Yang et al., 2021) (Rott et al., 2020)
Roughness formation mechanism	(Fleming et al., 2020)	(Feng et al., 2021)	(Feng et al., 2021)

Table 2.1: Studies about roughness - Literature review

Specimens without inclination

Guo et al., (2020) studied the top surface of cube shaped samples, printed with Inconel 738LC powder, by reconstructing it in three dimensions. They analyzed not only the surface roughness but also the porosity and crack density, by cutting the cubes in sections through Electrical Discharge Machining (EDM). Focusing on the surface roughness, calculated as average of nine different scanning areas, it was investigated as function of three process parameters: hatch spacing, scan speed and laser power, two kept fixed while only one changes. The minimum value they achieved was 10 μm. The principal conditions that they observe to decrease R_a are:

(1) Having a relatively large hatch distance (45 μm), thus the Marangoni flow (Figure 2.3), a mass transfer from the melt pool, fills the gaps between tracks creating a flat printed surface with no humps. The results showed that the surface roughness was worse with a smaller hatch distance than with high values of it.

(2) Increasing the laser power to improve bonding between layers and reduce balling.

(3) Decreasing the scan speed to not create gaps and to have a more stable process, since the energy input density is higher, and it improves the melting of the metal.

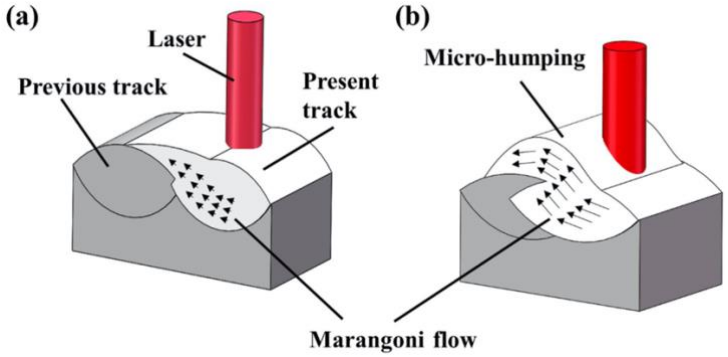

Figure 2.3: Marangoni effect with (a) large hatch distance and (b) small hatch distance (Guo et al., 2020)

A lower level of roughness, equal to only 1.1 μm, was achieved by Mohammadi & Asgari, (2018). The roughness values were averaged from the measurements done in 15 different points on the surface, but the value reported was not directly calculated after the production: it was subsequentially to a glass bead blasting, so the result is not comparable with the value in the study by Guo et al., (2020). As in the previous experiment, the specimens were cubes (Figure 2.4c), printed using AlSi10Mg powder, and only the top flat surface was under study. A relevant aspect of the paper is that the process parameters were adjusted differently according the up-skin, bulk and downskin layers. To enhance the surface finish, a lower laser power was used on the external regions. Several parameters were adopted: three were the same as in the research by Guo et al., (2020), recognized as the more relevant ones, and further ones were chosen differently depending on which area the layer was (up-skin, core or downskin, Figure 2.4a). To obtain the lowest R_a, the best strategy was to keep a higher surface energy density and concurrently to a lower beam offset[2] (0.1 mm) in the up-skin layer, in this way the structure is more regular and in order because the overlap is avoided. Again, as before, a low scan speed helped in preventing the formation of balling.

[2] The beam offset is the distance between the path of the laser beam and the nominal contour of the printed part

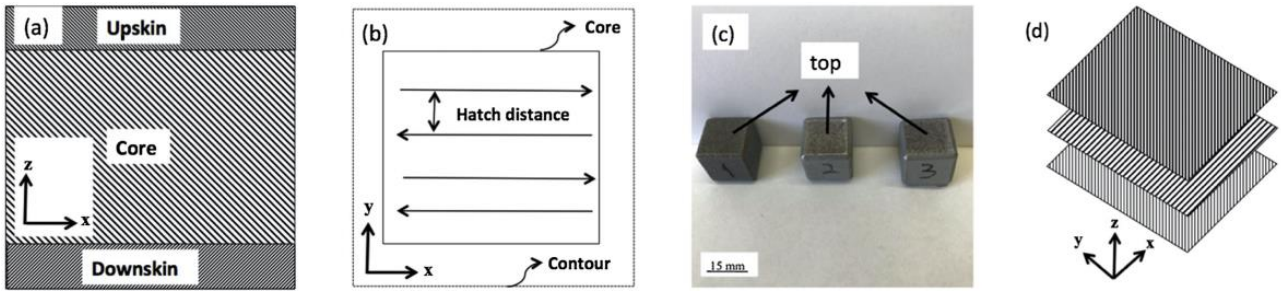

Figure 2.4: (a) Schema of up-skin, core and downskin layers, (b) schema of core and contour procedures and hatch distance, (c) three samples, (d) scan strategy adopted (Mohammadi & Asgari, 2018)

The study carried by Mumtaz & Hopkinson, (2009) elaborated a further step, not only the top surface roughness was analyzed as in the investigations by Guo et al., (2020) and Mohammadi & Asgari, (2018), but also the side one (Figure 2.5). To execute this, no specimens were printed, just four-layer thin-walled parts in Inconel 625. The arithmetic average roughness (R_a) was acquired both for top and side surfaces, and different process parameters were considered to see how they affected both the R_a at the same time. The main result they illustrate is that it is not possible to have the lowest value of roughness for both surfaces (4 μm for top R_a, and 10 μm for side R_a), because when one is enhanced, the other one is deteriorated. The upper face is improved by a low scan speed, high repetition rates, which induces a high overlap but entailing high balling formations in the edges. The side face needs opposite parameters, meaning a high scan speed with low repetition rates, since a low spot overlap reduces the side R_a. The parameter that improves the quality of both is high pulse energy because it increases the wettability of the melt pool and the bonding among layers. Finally, by compromising all the parameters, the optimal result attained in the work by Mumtaz & Hopkinson, (2009) is PBF printed part having top R_a equal to 9 μm and side R_a equal to 10 μm.

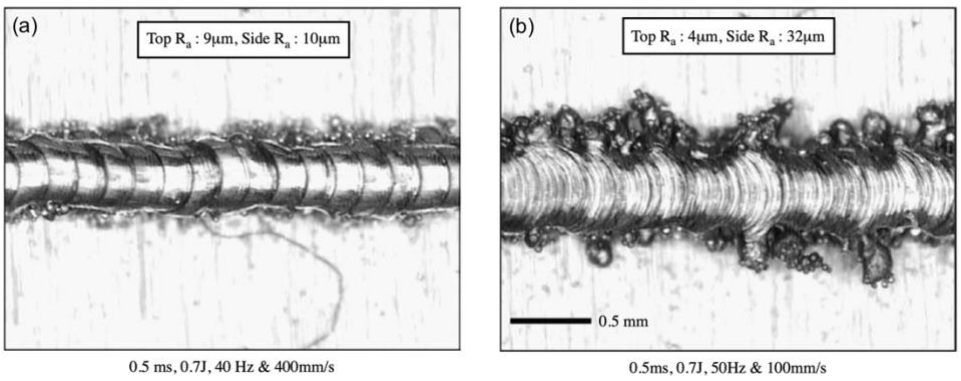

Figure 2.5: (a) Lowest side R_a, (b) lowest top R_a (Mumtaz & Hopkinson, 2009)

Specimens with inclinations

After having analyzed those specimens printed without inclinations, the focus switched to the understanding of tilted samples.

A great contribution in the study of the surface morphology in overhang regions came from Feng et al., (2021). The specimens under analysis (of the same shape), printed with a 17-4 PH stainless-steel powder, considered 6 different overhang angles (15°, 30°, 45°, 50°, 55° and 60°). Their experiment can be divided in two different steps: initially they performed a simulation of the printing process, followed by the print itself with the aim of finding correspondences between the attended and the actual results. Keeping the process parameters constant, they studied the effects of different impacting factors, the combination of which has high influence on the resulting roughness. The first studied effect is the one coming from the solidified border contour in the overhang region. In this area, in fact, one of the main contributors to the surface roughness come from the wavy overhang contour, more accentuated as the angle increases. Again, the powder adhesion (i.e., the remaining un-melted part on the overhang region, Figure 2.6) has a strong influence on the final surface roughness and, also in this case, the effect is more accentuated for higher inclinations. The third studied effect is the one coming from the warp deformation which, combined with the previous two, contributes to the overhang surface roughness. Even though the warp deformation is insignificant for inclinations lower than 45°, it should not be underrated for higher angles if printed without support structures. This warp deformation, indeed, is a direct consequence of thermal stresses, producing a departure in the vertical shape. Lastly, Feng et al., (2021) focused on the effects of the overhang angle itself on the surface roughness. This last effect was studied through simulation models by analyzing the difference between the expected overhang profile (a straight line) and the actual one. Coherently with the previous results, the deviation is much higher as the angle increases. The roughness, in fact, shows a quadratic trend in function of the inclination. Finally, as a solution for the roughness reduction, they suggest the decrease of the input laser power.

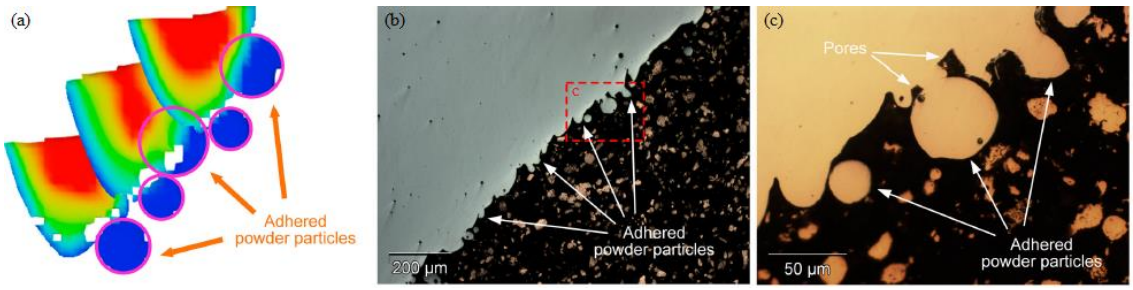

Figure 2.6: Effect of powder adhesion on the final roughness: (a) results by simulation; (b) optical micrograph; (c) focus of b (Feng et al., 2021)

An approach similar to Guo et al.,(2020) study was the one performed in 2019 by Charles et al., (2019). The controlled parameters were identical but applied to different specimens. They considered two samples (Figure 2.7), printed with a titanium alloy (LaserForm Ti gr23), of the same shape but with different inclinations (55° and 45°) with the aim of finding an optimal set of scanning parameters as to minimize the roughness of the overhang down-facing surfaces. Initially, they conducted different trials by varying two parameters at a time. The linear regression model found was then used to perform a Design of Experiment which indicated as minimum reachable roughness (S_a) 12.73 μm for the 45° down-facing surface and 20.01 μm for the 55°. The results showed that even for similar shaped specimens, a quite small difference in the inclination (10°) has significant influence both on the measured roughness and on the values of the parameters to be used.

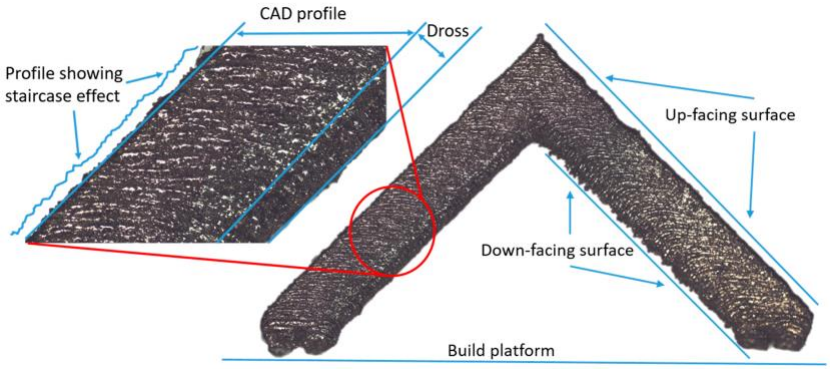

Figure 2.7: Dross formation influencing final roughness in down-facing surfaces (Charles et al., 2019)

The study of the impact of the surface orientation on the surface roughness was reproposed in 2021 by Yan et al., (2021). Differently from Charles et al., (2019), Yan et al., (2021) focused simply on the orientation of the part, while the process parameters were all kept constant. Their coin-shaped specimens (Figure 2.8) were printed according to 3 different angles: 90° (where the analyzed surface is basically the top one), 45° and 0° (lateral surface), while the powder used was Inconel 625. The chosen index for the quantification of the roughness was R_a, measured on a surface area of 1000 × 1000 μm. As expected, the smoothest surface was registered for the top surface, with a value of roughness equal to 5.706 μm, while the higher value was the one of the 45° specimen, where R_a reached 31.397 μm. The lateral surface seemed to have an intermediate behavior. The reason is to be found in other phenomena that affect the micro surface of the 45° sample, such as the balling and the stair-stepping effect, in accordance with the already discussed printing defects.

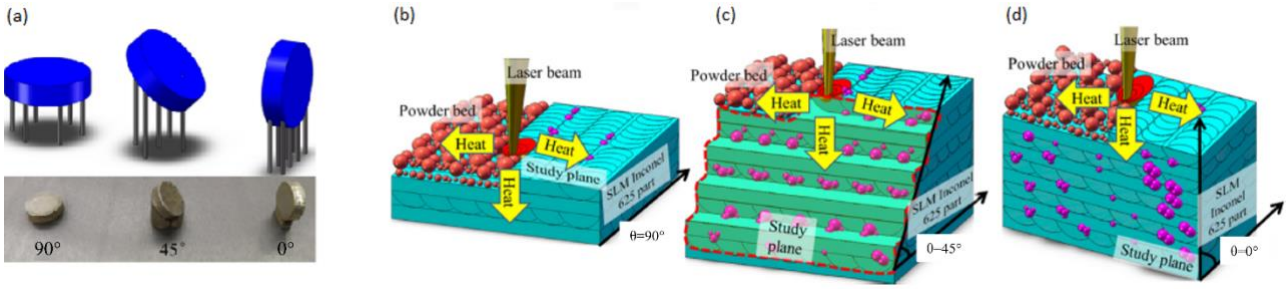

Figure 2.8: (a) Coin-shaped specimens and building angles; surface roughness formation: (b) 90°; (c) 45°; (d) 0° (Yan et al., 2021)

A similar concept was already presented in 2018 by Koutiri et al., (2018). The objective was equivalent, the minimization of the surface roughness of inclined specimens by varying the process parameters: laser power, scanning velocity and beam diameter. In this case, the specimens were blocks of 10 × 18 × 4 mm, again printed with Inconel 625, and tilted by 10° or 35°. Similarly to the previous studies, Koutiri et al., (2018) changed two parameters at time, recording the values of the obtained S_a. In general, they proved how a higher laser power generates a better value of S_a, indicating a smoothing effect coming from the layer re-melting. For the 35° the situation was more complex: a value of 140 W for the laser power could be considered the threshold after which the roughness started to increase again because, given the higher slope, more particles tend to stick on the melting zone. It is interesting, then, how the achieved S_a values of the down-facing surfaces were quite different for the two inclinations. In fact, for the 10° specimen the minimum roughness was 6.2 μm, while the 35° surface registered as minimum S_a the value 16.5 μm using the same parameters (Figure 2.9), except for the power which was decreased to the minimum value (100 W).

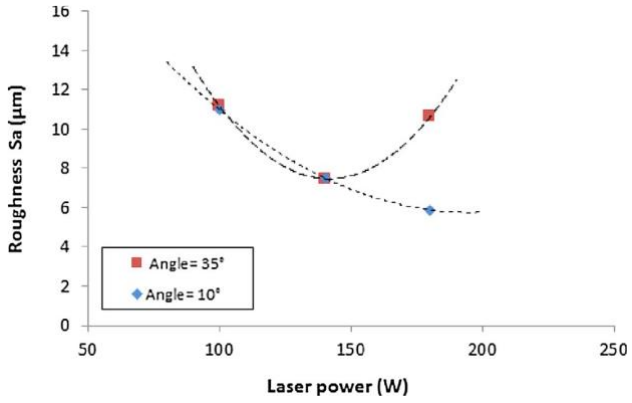

Figure 2.9: Influence of the laser power on the resulting surface roughness for the two inclinations (Koutiri et al., 2018)

The experiment performed by Fox et al., (2016) led however to a different result. Their specimens were parallelepipeds printed using a stainless-steel powder (EOS Stainless-Steel GP1) with 4 different overhang angles (from 15° to 60°), respect to the printing direction (Figure 2.10). Each part was produced using 4 different sets of process parameters. By measuring the R_a value of the down-facing surface, they were able to demonstrate that, although a relationship between the measured surface roughness and the build angle is evident, the same cannot be said for the roughness and the process parameters. This was also true for other roughness parameters, such as R_z or R_q. The lower value of roughness (≈16 μm), consistent with the above, was reached for the less inclined surface (15°[1]).

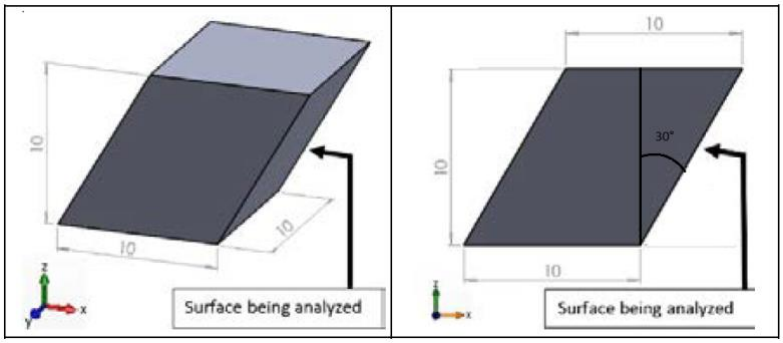

Figure 2.10: Example of the 30° inclined produced part and surface under analysis (Fox et al., 2016)

The study conducted by Simoni et al., (2021) considered as roughness parameters not only R_a but also R_z (the mean roughness depth). The specimens, printed with a CoCr alloy, were 6 blocks of 15 × 20 × 3 mm^3, each one inclined of 15° more respect to the previous, so that the first is flat and the last is tilted by 75°[1]. Even though the process parameters are not available, from the results is clear the dependency between the final surface roughness and the build angle. In fact, both the roughness parameters decrease as the angle decrease (the specimens are more vertical) and, predictably, the 0° sample shows the lowest values both for R_a (3.382 μm) and R_z (19.770 μm), (Figure 2.11). The main focus of the work, however, was to study the effects of the remelting strategy on the final roughness, which exceed the scope of the analysis of the present Thesis.

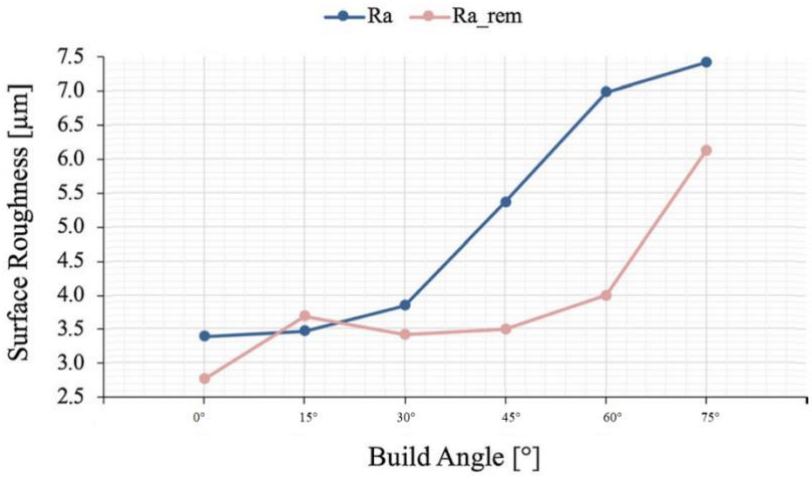

Figure 2.11: Effect of the build angle1 on the final roughness (Simoni et al., 2021)

In a recent study Yang et al., (2021), executed a DoE to analyze the influence that process parameters have on the overhang down-facing surfaces at high angles (30°, 45°, 60°), without using any support structure. The specimens had a tilted parallelepiped shape (Figure 2.12), printed using AlSi10Mg powder. Both contour and infill parameters were considered, and the principal ones were laser power, scanning speed and scanning angle, including them in a statistical ANOVA analysis. As expected, and in accordance with the previous works, the tiniest inclination (30°[1]) has the lower value of R_a, corresponding to 4.22 µm, one of the optimal values out of the papers analyzed in this section. The other angles had higher R_a, respectively the steepest one (60°[1]) reached 10.9 µm and the remaining one reached 7.9 µm. This was due to a large quantity of adhered balls. The conclusions they attain is that when the inclinations are more flattened, the only significant parameters are contour laser power and scanning speed, since it is a less delicate processing. When the inclination is higher, more parameters are critical (the contour energy density[3], the contour scanning speed, the scanning angle and finally the infill scanning speed). An interesting relationship which is deepened is the one between the scanning angle and R_a. It is seen that by keeping a scanning angle perpendicular to the edge of the overhang surface, the adhesion balls are reduced, improving considerably the roughness. This result is amplified for higher building angles.

[3] LED_c defined as: contour laser power / contour scanning speed.

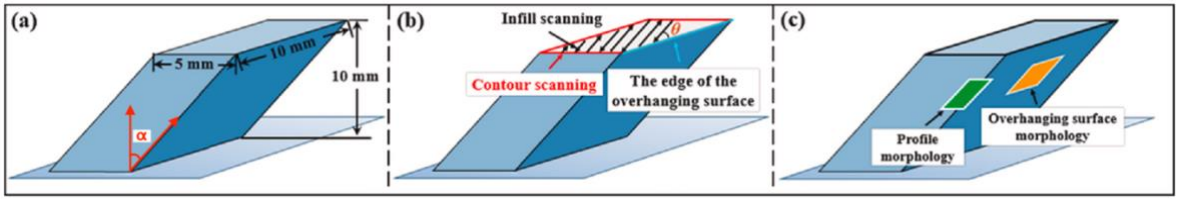

Figure 2.12: 3D representation of specimen: (a) geometric dimensions and build angles (**α**1 = 30°, 45°, 60°), (b) scan strategies and scanning angle **θ**, (c) morphology (Yang et al., 2021)

The investigation performed by Rott et al., (2020) intends to predict surface roughness by the relation among surface orientation and laser incidence. The angle among the two is a novel parameter (ζ) that they use (Figure 2.13b). The experiment regards truncated inverted pyramids (opening angle of 30°[1]), built using Amdry 1718 (Figure 2.13a). The shape of the specimens did not change, only their orientation did. The conventional angle that is considered for down-facing parts is the one between the surface and the horizontal plane (α). In this experiment both were considered in two different batches of specimens: the first one kept α (30°[1]) constant, the second one kept ζ (120°), in a way that the piece is always tilted towards the laser. By using a constant ζ during the processing, R_a can decrease significantly, and the lowest value reached is 5 μm. Contrary, α is not the principal parameter that influence the surface roughness, in opposition to what resulted from the previous papers. To claim it, the batch where α was kept constant was analyzed, and the values of R_a had a wide range, while when α was changing (and ζ was fixed), R_a had a narrow range of value.

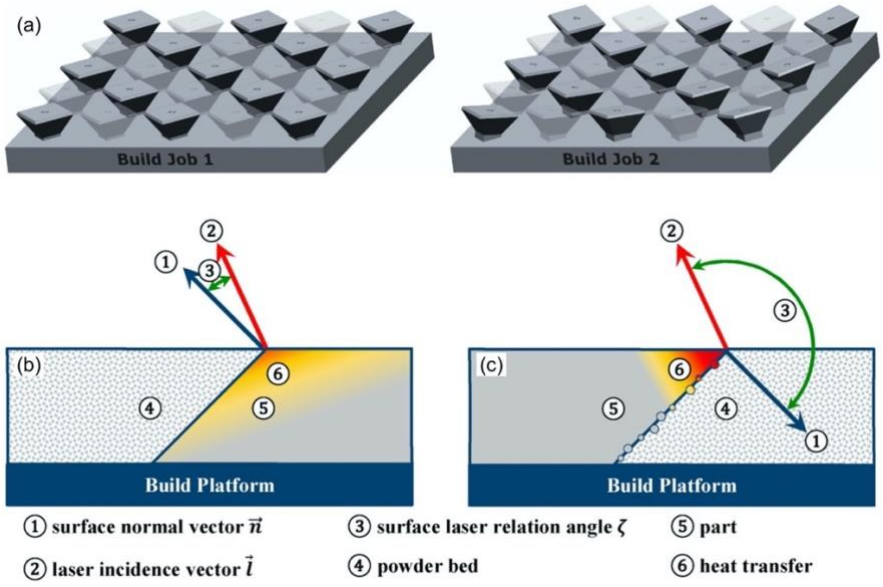

Figure 2.13: (a) Specimen of the two build jobs, heat transfer condition for (b) acute angle ζ and (c) obtuse angle ζ (Rott et al., 2020)

2.2. In-Situ

Different studies recognize the common origin of the roughness defect, linking it to the thermal stresses faced by the material during the on-going production. These thermal stresses are directly caused by the sudden changes in temperature, namely the melting and cooling phases, occurring while the part itself is being produced. It is useful to better understand these in-situ phenomena and how the melt pool is influenced by them.

In the study by Hooper, (2018), melt pool temperature peaks, gradients, cooling rates and sizes are analyzed and the objective is to demonstrate that those properties are diversified according the different positions in the produced part. The output under study regarded the surface temperature of the melt pools scanned by the laser, measured using a high-speed camera together with a two-wavelength imaging setup. The recorded locations are the bulk, the outer border, the overhang (Figure 2.14), and the material used to build the specimen is Ti6Al4V. Respectively, in the first one the melt pool is generally stable, except for some spatters and gradually there is less control while reaching the borders. The parameters regarding laser power, exposure time and point distance change according to the position. All of those are lowered in the outer border, generating a smaller melt pool to reduce the probability of defects. Lastly, in the overhang the cooling lasted more time since the powder underneath the printing area has less heat conductivity respect to the bulk. The melt pool achieves a long-tail shape, and its size is reduced since more spatters are present. Generally, in all the area of the specimen, the tail of the melt pool has a homogeneous temperature, in the range of the melting point of the material. Its length is reduced regarding the outer border, and it is at its maximum during the overhang scan. The peak in the temperature can be typically found in the head of the melt pool. Not even the position, but also events as the change of direction of the scan line, the end or the beginning of the scan line can affect the temperature and the melt pool.

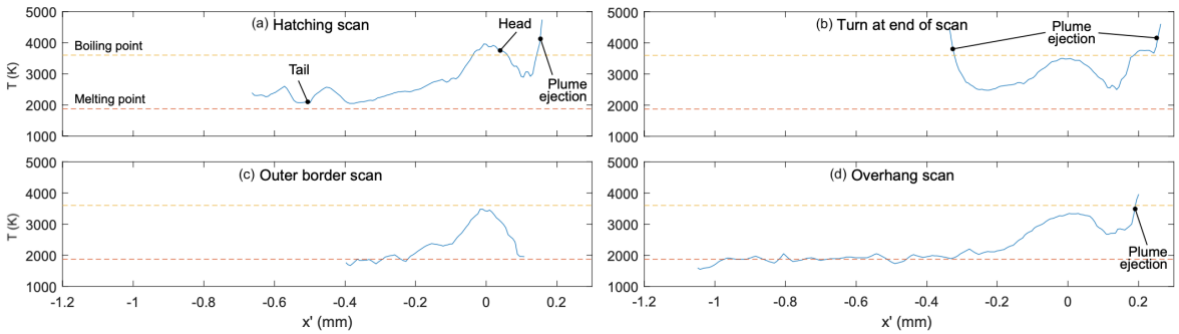

Figure 2.14: Melt pool scan (a) in the bulk, (b) at the change of direction, (c) on the outer border, (d) on the overhang (Hooper, 2018)

The methodology described by Mahmoudi et al., (2019) has as objective the detection of anomalies in the process by analyzing melt pool temperatures, since melt pools are an indication of process stability. The analysis focused on thermal images acquired with a two-wavelength imaging pyrometer, and anomalies are distinguished as pixels with too high or too low intensities. The method is structured in phases. First, data are acquired while the part is printed, extracting process signatures (Figure 2.15a) for each layer by merging the melt pool high speed thermal images generated in the current layer. The analysis does not regard the absolute temperatures, but the variations that affect the process. Due to this, the focus is not directly on the process signatures but on the difference measured between the reference signature coming from a fully dense specimen without flaws. The second step is the screening, in which the regions of interests (ROIs), the areas in which it is more probable that defects are formed, are determined. Then, with a Gaussian process method, the ROIs are analyzed to identify and flag the deviations (Figure 2.15b). It is not enough that a ROI has a high number of flagged pixels to be considered anomalous, the spatial interconnection of pixels has to be considered as well. Finally, a classification is performed by selecting a training dataset both with faulty and faultless layers to train the classifier and a test dataset composed by a faulty layer to evaluate the classifier. The authors were able to recognize process anomalies implementing an in-situ layer-wise control based on classification, establishing if a ROI is considered defective or not.

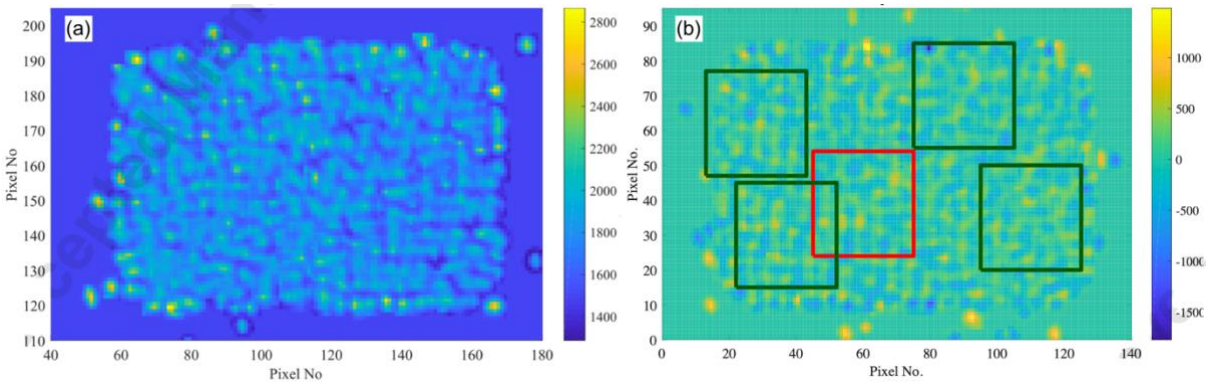

Figure 2.15: (a) Example of thermal process signature and (b) example of faulty layers with identified ROIs (Mahmoudi et al., 2019)

Criales et al., (2017) performed an experimental investigation once again on the melt pool, in particular the analysis had its focus on its size and shape, measuring both with a digital microscope and with thermal images. It is described as a "dynamic" melt pool, because it is in continuous evolution while the laser hits the powder. It was separated in two categories (Figure 2.16). Type I, the melt pool created when

the track that is being scanned by the laser is still affected by the heat emitted by the previous scanned track. This group was larger and not symmetric. The melt pool of Type II instead is the one which is not altered by the heat of the area around it. Oppositely to the first one, it was smaller and more regular. Different process parameters were then used to investigate how the melt pool would be affected. First its width and depth, then its shape were evaluated. The authors determined several outcomes. Regarding the melt pool dimensions, it decreases when the parameters respect those conditions: decreasing laser power, increasing scan speed and incrementing the hatch distance. It is important to specify that model is not linear. Those parameters, together with layer thickness, can be brought together by calculating the energy density. The latter influences in a proportional way the melt pool size. In relation to the shape instead, it becomes more symmetric when: the laser power and the scan speed are low, the hatch distance and the energy density are high. Again, the model is not linear. To conclude, the authors' initial hypothesis, which guessed that the hatch distance has the strongest influence, was be confirmed.

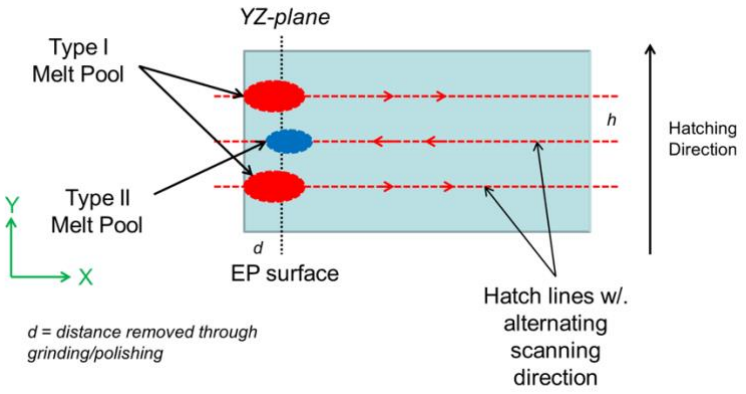

Figure 2.16: Melt pool Type I and Type II representation (Criales et al., 2017)

Lane et al., (2016) tried to understand some important characteristics of a L-PBF process from a thermographic point of view. Their study, conducted on Inconel 625 printed cubes, mainly focused on two attributes, through the adoption of a MWIR camera: the temperature rates of selected pixels along the melt track and the particle ejection (Figure 2.17). While the pixels at the center of the printed track show temperature levels which are always quite above the minimum measurable temperature due to the reheating of adjacent tracks, the same cannot be said for the edge pixels. Their temperatures, in fact, reach low values not easy to quantify, considering that the laser is scanning the opposite side of the track. As for the particle ejection, the main conclusion is related to their dimensions. The authors highlight how their size can reach the value of 200 μm, much higher respect to the

powder dimension. This work, however, has two main limitations: the first one is related to the acquisition frame rate used, too low to capture some significant characteristics. The second one, instead, is linked to noise and reflection created by the ejected particles which may adversely affect the signals originated with the thermography.

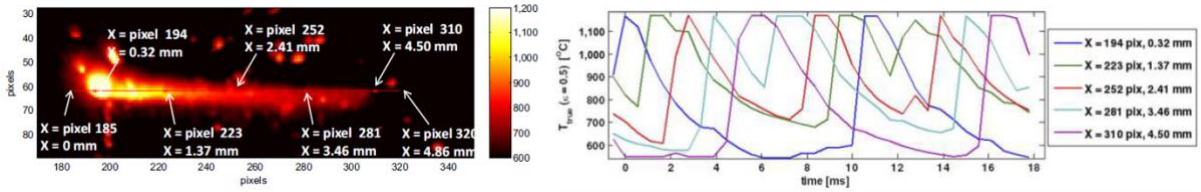

Figure 2.17: (a) Selected pixels along the laser track; (b) relative temperature rates. (Lane et al., 2016)

A different approach in the thermography analysis came from Altenburg et al., (2020). In their experiment, the printing process of a cubic sample (AISI 316) was registered with a mid-wave infrared camera. The first analyzed characteristic is the cooling down behavior of selected pixels along the scanned layer. The principal conclusion is that according to the chosen pixel (in the initial, middle or the last scanned part of the layer, Figure 2.18a), the temperature curves show a different behavior either in the heating up or in the cooling down part (Figure 2.18b). The novelty comes from the second used parameter, the Time Over Threshold (TOT), which is the time a selected part of the layer shows a temperature above a certain threshold (Figure 2.18c). Again, this parameter depends on the position of the considered area: the upper corners have a relatively low value, due to the absence of heating in the adjacent area. An increased value of the TOT, instead, when accompanied by a decreased cooling rate, could be an indication of a defect.

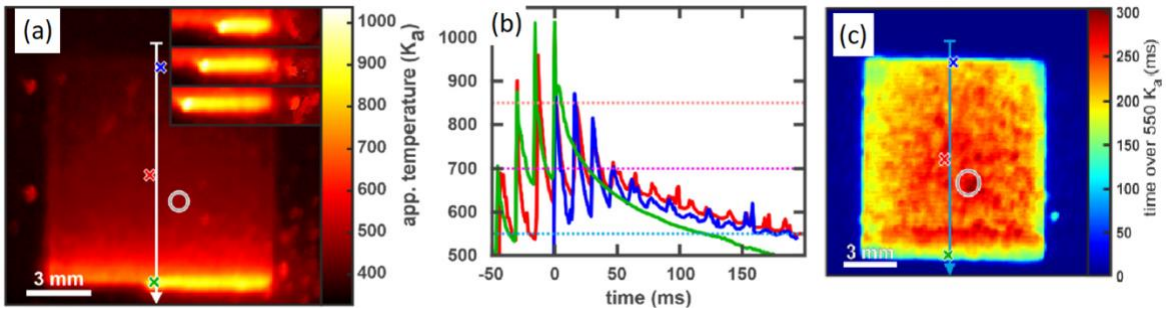

Figure 2.18: (a) Thermal video of scanned layer and position of 3 selected pixels; (b) cooling down curves of selected pixels; (c) TOT map of the same layer (Altenburg et al., 2020)

2.3. Correlation Ex-Situ and In-Situ

Once understood the main characteristics of the surface roughness and the behavior of the melt pool from a thermographic point of view, the focus switched on the investigation of their correlation. Nevertheless, only few authors have faced this correlation between in-situ attributes and the ex-situ surface quality. In addition, the vast majority concentrated just on the layer-by-layer printed surfaces rather than on the lateral ones, leaving unexplored the investigation of the correlation between the thermography analysis and the final quality of the external surfaces.

In a study performed by Yin et al., (2020), the correlation between in-situ processing and ex-situ morphology was investigated. More in the specific, the spatter dynamics during the printing process and the final melt track were analyzed on Inconel 718. The latter has a distinct trend: at the beginning a protrusion is noticeable, then the central part is flat and at the end a depression is formed (Figure 2.19a,b). Different relations were discussed:

(1) head protrusion against droplet ejection behavior.
(2) tail depression against backward-ejected spatter.
(3) vapor recoil pressure against forward-ejection spatter.

The most interesting results are following explained. In (1) it is illustrated that the Marangoni centrifugal convention and the recoil pressure cause a centrifugal flow of the melt pool and droplet ejection that originate the protrusion of the melt track (Figure 2.19c). Regarding the (2), the authors studied that the angle of the melted and powder spatters can be used to derive the geometry of the depression zone of the molten pool and the molten pool state (Figure 2.19d). The reason is that the backward ejected spatters, which are mainly caused by the vapor plume, have the same direction of the normal vector of the front wall and of the rear wall of the depression zone, and they are all depend on the laser power. Lastly, about the (3), the recoil pressure of the spatters can be adopted to determine the recoil pressure of the depression zone of the melt pool, since the latter is more complicated to calculate directly.

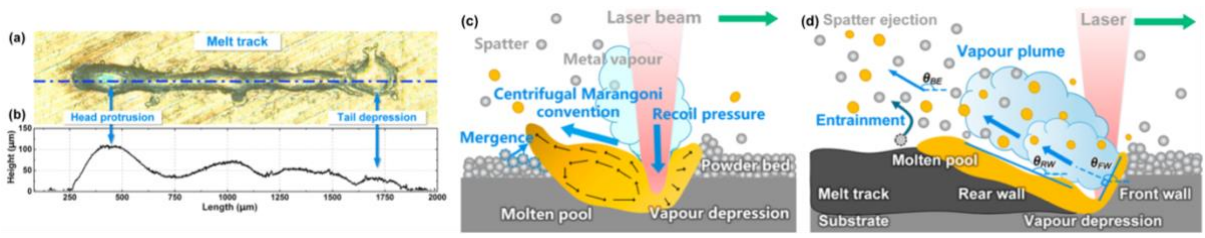

Figure 2.19: (a) Melt track morphology and (b) longitudinal profile, (c) protrusion mechanism, (d) depression zone formation (Yin et al., 2020)

Foster et al., (2018) focused instead on the correlation between the in-situ infrared thermography and the ex-situ surface roughness, and contrary from Yin et al., (2020), the spatter phenomena was not kept in consideration due to low temporal resolution of the IR camera. The authors first analyzed the IR intensity, without transforming it in temperature because of inadequacy of calibration parameters, with the quality of the build. The peaks of intensities were found in correspondence of the areas where the melt pool temperature was above the evaporation threshold. The correlation found was among the IR intensity and the decline of the print quality and the increment of hatch spacing. The latter has high influence on surface roughness since the track overlap can induce valleys and hills, if it is too far, or on the contrary a steady surface with an ideal hatch spacing. Finally, a model regarding Rosenthal equations was adopted to predict the melt pool characteristics, and correlate them with the measured ones, relating to the melt pool, the surface roughness and the porosity.

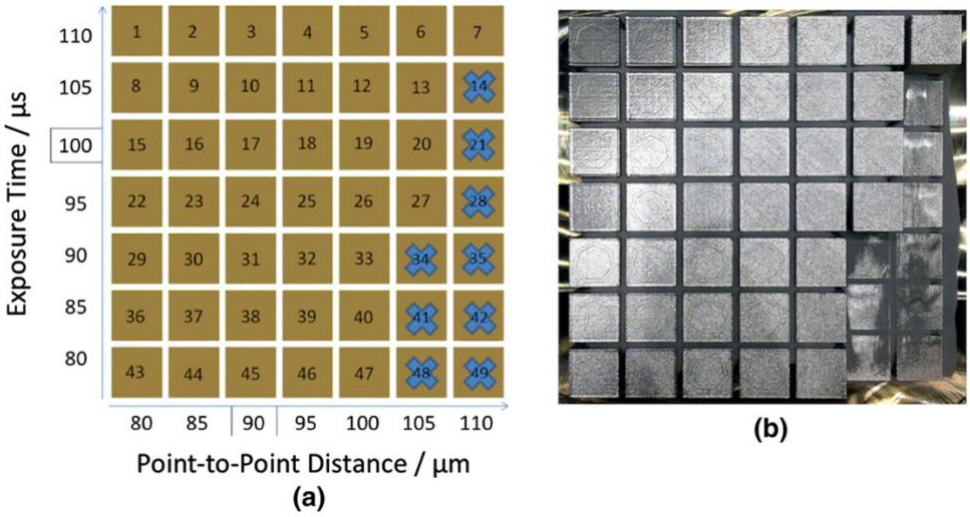

Figure 2.20: (a) Process parameters and (b) specimens: matrix of cubes (Foster et al., 2018)

In the article by Scime & Beuth, (2019) the correlation among ex-situ and in-situ was investigated with a different approach with respect to the previously described ones: the authors developed a Machine Learning method, first with a training set, then confirmed with a validation one. Two main parameters were considered: beam power and beam velocity. Various combination of them were examined. The scope was to classify different melt pools according to various ex-situ morphologies. As result, four categories were identified: desirable, balling, under-melting, and keyholing porosity (Figure 2.21). The in-situ melt pools images were acquired by a high-speed camera, then transformed in coaxial images, each labeled with the process parameters used. Part of this set was used in a machine learning technique

which was unsupervised since the classification of the in-situ morphologies were not known. Then with a cross validation, a supervised ML method was used to classify the melt pools not included in the training set. With the use of this tool, the authors were able to recognize if the in-situ morphology of a specific melt pool had similarities with one of the four ex-situ categories previously listed.

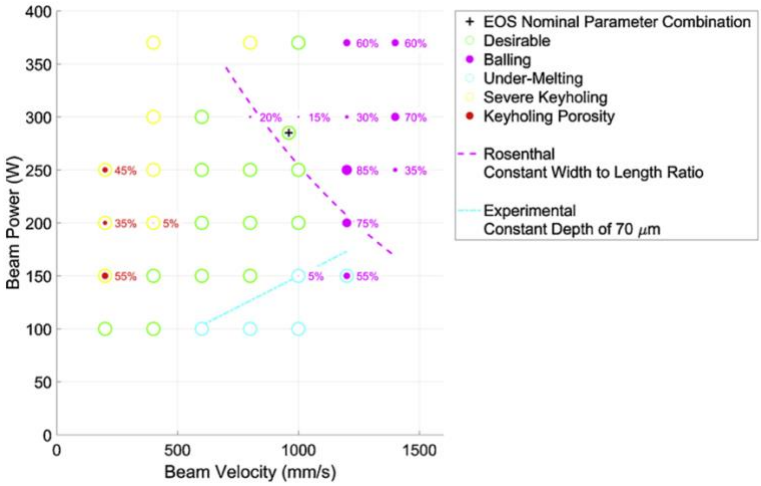

Figure 2.21: Schema representing ex-situ melt pool morphologies varying the process parameters (Scime & Beuth, 2019)

Differently from Scime & Beuth, (2019), Knaak et al., (2021) conducted a more sophisticated approach (Figure 2.22): before the machine learning technique, a neutral network procedure was implemented. The NN was trained using both S_a measurements, acquired by an interferometer, and high dynamic range (HDR) optical images of the specimens top surfaces of current layer, divided in class according to the corresponding range of S_a values, of the final top surfaces of printed cubes. The model was then verified utilizing previously unmeasured surfaces. The scope of this first part of the analysis was to predict the top surface roughness obtained according to different combination of process parameters. This result was then used as feedback for the machine-based reinforced learning technique, which objective was instead to find the optimal combination of parameters. Finally, with the develop method, the authors were able reduce both the final roughness and the defect rate on the printed surfaces. The main detected conclusion is that the strongest influence on surface defects is given by the volume energy density: the higher the VED, the higher the probability of defects. Furthermore, a negative correlation was found among part density and surface roughness: when a higher part density was detected, the corresponding S_a was lower.

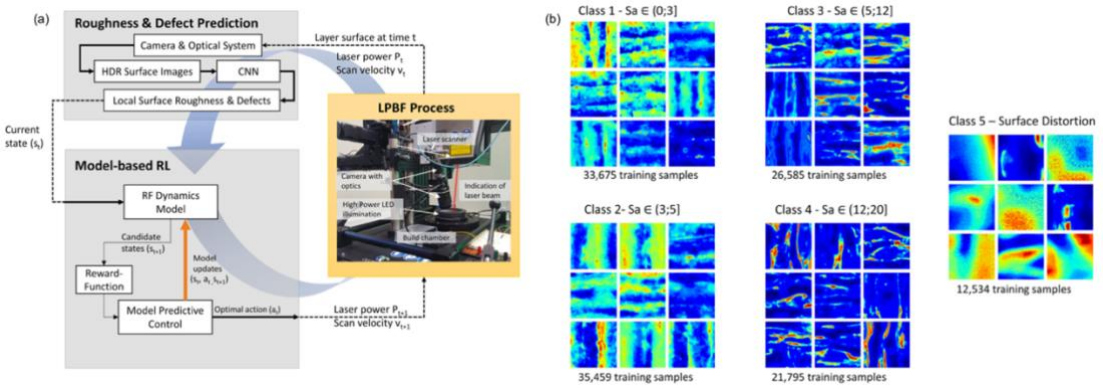

Figure 2.22: (a) Schema of the developed methodology, (b) example of HDR images with corresponding S_a classes (Knaak et al., 2021)

The study performed by Mohr et al., (2020) is an expanded version of an examination already discussed in Section 2.2 (Altenburg et al., 2020). This work is not only an inspection of in-situ characteristics, but it tries to compare the outcomes of parameters measured in real time with some induced defects analyzed through an ex-situ study. Concerning the ex-situ inspection, the main conclusion is a direct correlation between the presence of internal defects and the value of VED used: a high energy density leads to keyhole porosity, while a low one has a strong influence on the presence of lack-of-fusion voids. This inspection is then accompanied by an in-situ analysis, through the computation of two metrics: the TOT and Optical Tomography (OT) intensities. From the correlation analysis (Figure 2.23) two main outcomes can be ascertained: first, a direct comparison between a nesting of porosity and an increased value both for TOT and OT intensities. Secondly, in correspondence of an artificial induced cavity, the TOT has a sharp increase in the first melted layer after the defect. It is then clear how the in-situ inspection could give important indications about the final quality of the produced part.

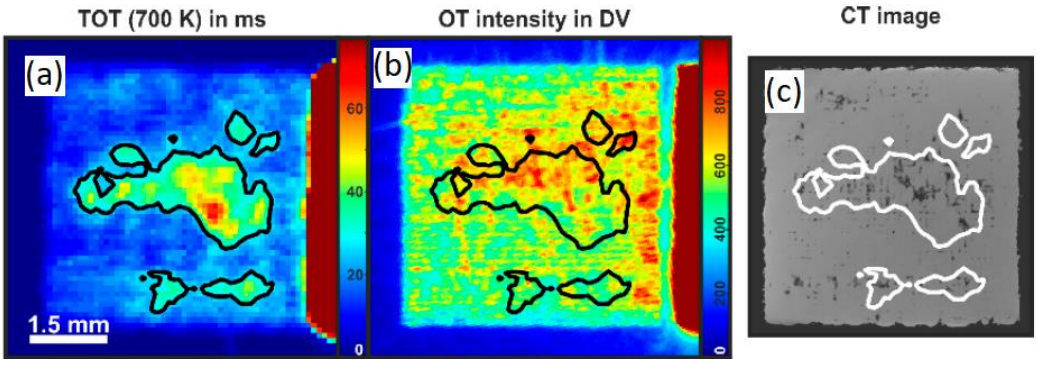

Figure 2.23: Nesting of porosity; correspondence between (a) the TOT; (b) the OT intensity and (c) the ex-situ tomography (Mohr, Altenburg, et al., 2020)

3 Experimental Details

3.1. Design of Experiment

The dataset analyzed in this work has been achieved from specimens produced through Laser Powder Bed Fusion methodology using AISI 316L and AlSi10Mg. The particle size distribution of the former material is as follow: D10 and D50 of the powder were 18-24 μm and 32.5-34.4 μm respectively. The second instead has a declared dimension of 20-63 μm. The printed parts were designed to analyze how surface quality and thermals are affected by different overhang angles. For this reason, four models were created for each of the two materials, and each with a different angle. All the specimens have the same shape: a parallelepiped architecture with one of the 6 faces inclined of the respective angle, as shown in Figure 3.1 and in Figure 3.2. The base (5 mm x 5 mm) and the height (5 mm) are constant. The four progressing inclinations are 15°, 30°, 45° and 50°, denominated as OH values in the work.

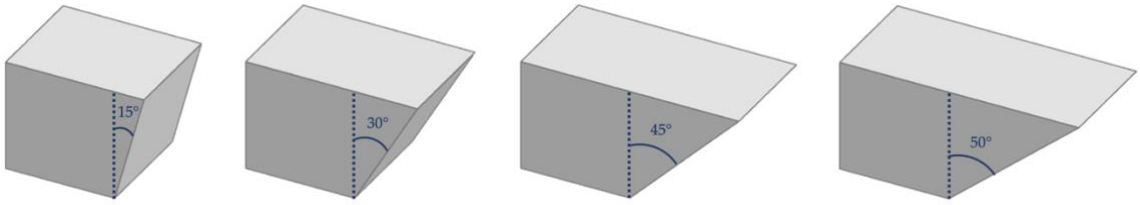

Figure 3.1: Specimens with respectively 15°, 30°, 45° and 50° angles

In addition to these two studies, a third one is carried out, concerning again 4 specimens. The angle is kept constant to 45°, threshold after which the surface quality begins to decrease significantly faster. The changes are instead in the scan strategy, to investigate how different print methods influence the samples, having the same geometry.

For a better clarification, the various trials studied are hereafter summarized:

• Four specimens produced in AISI 316L, with overhang angles of 15°, 30°, 45° and 50° and fixed scan strategy (Figure 3.3).

• First experimentation on AlSi10Mg, four specimens with overhang angles of 15°, 30°, 45° and 50° and fixed scan strategy.

• Second experimentation on AlSi10Mg, four specimens with fixed overhang angle of 45° and variable scan strategy.

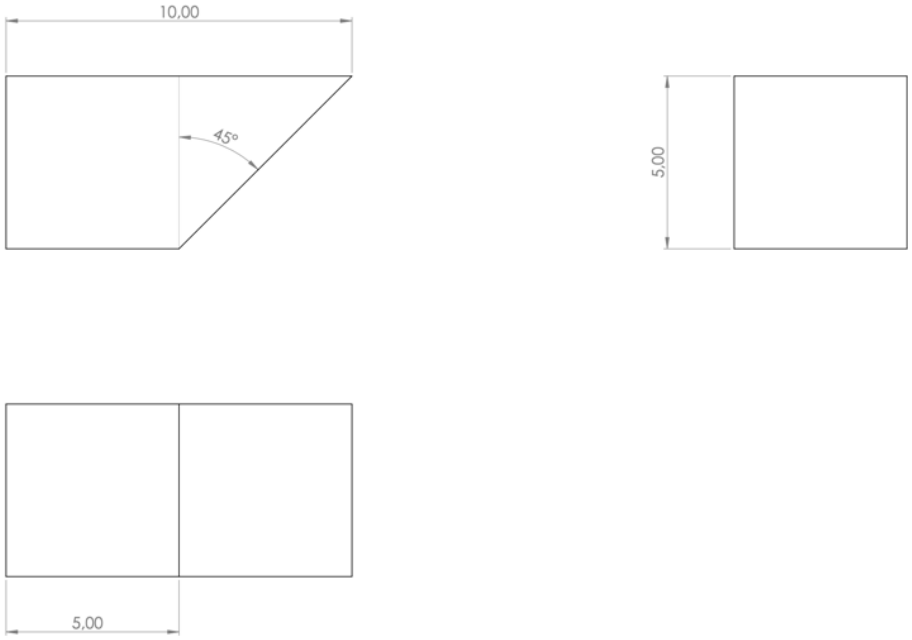

Figure 3.2: Technical drawing of the specimen with overhang angle of 45°

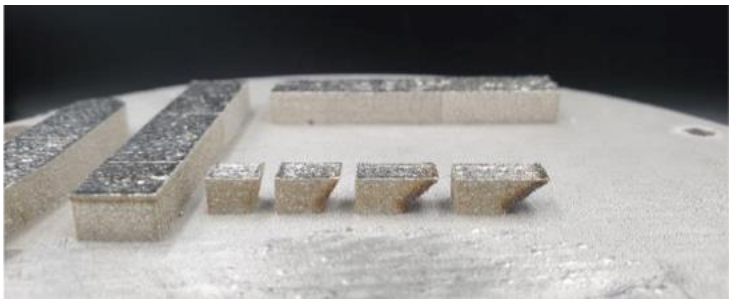

Figure 3.3: Printed parts after production (AISI 316L Job)

3.2. Machinery and Tools

3.2.1. F3DNT L-PBF Prototype

Figure 3.4: 3DNT L-PBF Prototype

The equipment used in this study was a 3DNT L-PBF Prototype (Figure 3.4) located at the Politecnico di Milano, specifically in the Add.Me Lab of Mechanical Engineering. The volume of the chamber has a cylindrical shape, and it measures 160 mm of height and 150 mm of dimeter. Inside there are various in-situ sensors and it is provided of fiber laser (**λ** = 1064 nm), with spot dimeter of 70 μm at layer height, 200 W of nominal power.

The AISI 316L parts are composed by 166 layers, each of them with a thickness of 30 μm, instead regarding the AlSi10Mg, the layer height was reduced to 25 μm, with consequentially 200 scans. The process parameters are summarized in Table 3.1 and they have been kept constant for all the specimens. The main parameter used in L-PBF, as it is demonstrated in literature, is the Surface Energy Density, which is calculated as follows:

$$E = \frac{P}{h \cdot v}\left[\frac{J}{mm^2}\right]$$

Equation 3.1: Surface Energy Density

Where P is the laser power [W], h is hatch spacing [mm] and v is the scan speed [mm/s]. In the experiment, those parameters did not change, and the Surface Energy Density maintained the value of 4.44 J/mm² (AISI 316L) and 2.22 J/mm² (AlSi10Mg).

	AISI 316L Job	1st AlSi10Mg Job
Scan Power [W]	200	200
Laser emission	Continuous wave	Continuous wave
Scan Speed [mm/s]	900	1000
Hatch Spacing [μm]	50	90
Number of layers	166	200
Thickness of layers [μm]	30	25
Energy Density [J/mm^2]	4.44	2.22

Table 3.1: Process parameters of the specimens in AISI 316L, and in AlSi10Mg (1st experimentation)

As already mentioned, the second AlSi10Mg experimentation had a variable scan strategy, and respectively, the 4 specimens were produced as follows. Regarding the first one, named as CW +0%P, a continuous wave (CW) emission is adopted, and the scanning parameters were maintained equal to the first experimentation in AlSi10Mg. For the remaining three samples instead a pulsed wave (PW) emission was tested, changing for each sample the used laser power with the aim of inducing several thermal conditions. In particular, by following the denomination in Figure 3.5, for the sample denoted as PW +0%P the same laser power of the continuous mode was used, 200 W. The sample PW +20%P is characterized instead by an increase of the 20% in the emitted power, a value equal to 240 W. In parallel, a reduction of 20% of the laser power was applied to the PW -20%P specimen (160 W). A recap of the different scan parameters used for the 4 specimens is summarized in Table 3.2.

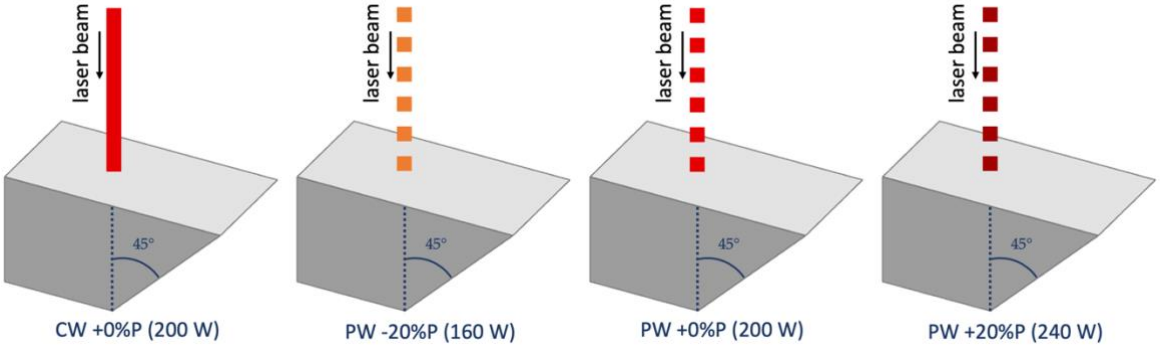

Figure 3.5: Specimen details of AlSi10Mg 2nd experimentation, showing the continuous vs pulsed laser wave, and the different intensities of power.

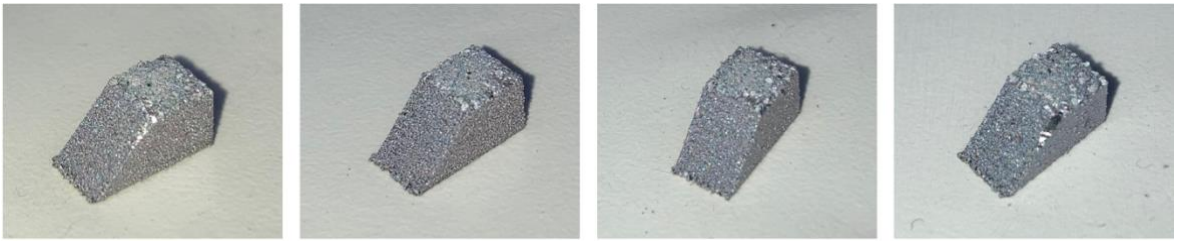

Figure 3.6: Specimen in AlSi10Mg (2nd experimentation), from left to right: CW +0%P, PW -20%P, PW +0%P and PW +20%P.

	CW +0%P	**PW -20%P**	**PW +0%P**	**PW +20%P**
Scan power [W]	200	160	200	240
Laser emission	Continuous wave	Pulsed wave	Pulsed wave	Pulsed wave
Scan speed[mm/s]	1000	500	500	500
Hatch Spacing [μm]	0.09	0.13	0.13	0.13
Triggering Frequency [Hz]	-	6.25	6.25	6.25
Point distance [μm]	-	80	80	80

Exposure time [μs]	-	140	140	140
Number of layers	200	200	200	200
Thickness of layer [μm]	25	25	25	25
Energy Density[J/mm²]	2.22	2.15	2.69	3.23

Table 3.2: Process parameters of the specimens in AlSi10Mg (2nd experimentation)

It is worth to highlight that the computation of the Energy Density parameter for the pulsed wave emission requires a different formula.

$$E = \frac{P \cdot Te}{h \cdot Pd}\left[\frac{J}{mm^2}\right]$$

Equation 3.2: Surface Energy Density for pulsed laser wave emission

Where P is the laser power [W], Te is exposure time [s], h is the hatch spacing [mm] and Pd is point distance [mm].

The printing technique has a periodicity equal to four layers for all the jobs, since the angle of the laser rotates of 90° after manufacturing each layer (Figure 3.7), defining a meander path. The inert gas flux, which in the specific was Argon, had a inclined orientation of 10° respect to the centerline.

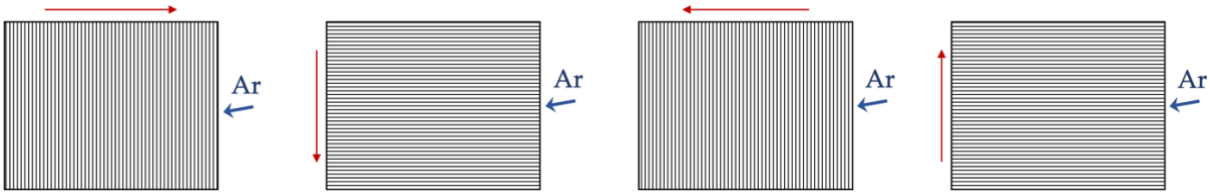

Figure 3.7: Printing technique illustration, the red arrow represents the direction and the orientation of the laser during scanning. The blue arrow is the direction of the Argon gas. Respectively the layers in the picture are Layer 62, Layer 63, Layer 64, Layer 65.

3.2.2. In-Situ Monitoring Equipment

Figure 3.8: FLIR x6901sc IR Camera

To monitor the in-situ production and acquire data layer-by-layer, the FLIR x6901sc MWIR IR Camera (Figure 3.8) was adopted and installed in the L-PBF machine. The complete build job did not regard only the four specimens under analysis and, to diminish the acquired data to only the necessary dataset, the frame was cropped from 640x512 pixels to 72x224 pixels and the framerate was set at 667 fps (AISI 316L) or 500 fps (AlSi10Mg). The blackbody-equivalent temperature that the camera can monitor ranges from 30°C to 1500°C. The camera is positioned 520 mm away from the power bed and its lens measure 50 mm. The machine is equipped with a silica glass, for AISI 316L, and sapphire glass, for AlSi10Mg, which permit to the camera to see in the internal environments, since they allow to accurately detect IR waves. The camera is 30° off axis with respect to the build platform normal.

Videos can have three different formats, which are Counts, Radiance and Temperature. The latter one is used in this analysis.

3.2.3. Ex-Situ Characterization Equipment

Figure 3.9: InfiniteFocus by Alicona

Besides the in-situ data acquisition, also the final surfaces of the specimens had to be investigated. The machine used for this purpose was InfiniteFocus by Alicona (Figure 3.9), an optical 3D measuring system, which uses Focus Variation Microscopy to reconstruct the 3D structure of the part in the form of a point cloud. Different objective magnifications (5x, 10x and 20x) have been tested. Among the alternatives, the 5x magnification allowed the best trade-off between resolution and computational burden, therefore it was the adopted one.

4 Data Analysis

The following chapter illustrates the core phases of the experimental investigation.

The data analysis was performed in a sequence of ordered steps. It begins by acquiring the necessary data: both the surface roughness, acquired after the specimens were produced, and the thermal data, recorded while the print was executed, are useful in this investigation. Then, a cleaning operation is mandatory: the irrelevant or redundant information, along with the outliers, needs to be handled before the exploration. Once only the relevant material was selected, the extraction of parameters was carried out. Those phases were performed for both materials: AISI 316L and AlSi10Mg. To avoid repetitions, in the following sections these steps are described only for the steel specimens, knowing that the same procedure was repeated for the aluminum samples. At last, the results are discussed separately for the two materials, illustrating the differences among AISI 316L and the first experimentation in AlSi10Mg. The second job produced with the aluminum alloy is instead delineated in a final section, to validate and deepen the previous analysis.

4.1. Data Acquisition

4.1.1. Surface Roughness Data

Once the production of the specimens was completed, the investigation concerned the final quality of different surfaces. The first step regarded the ex-situ data acquisition, performed with Alicona InfiniteFocus optical microscope (Chapter 3.2.3). The chosen surfaces to measure are represented in Figure 4.1, and the same superficies were scanned for each specimen. The Overhang Surface was acquired to study the influence of the different angle inclination on the surface roughness, and to demonstrate the hypothesis that for steeper angles a higher roughness is expected. Vice versa, the Vertical Surface, opposite to the overhang, is considered as 0° angle. This latter acquisition can be considered an extension of the original dataset with the aim of considering a surface with a more homogeneous and moderated roughness.

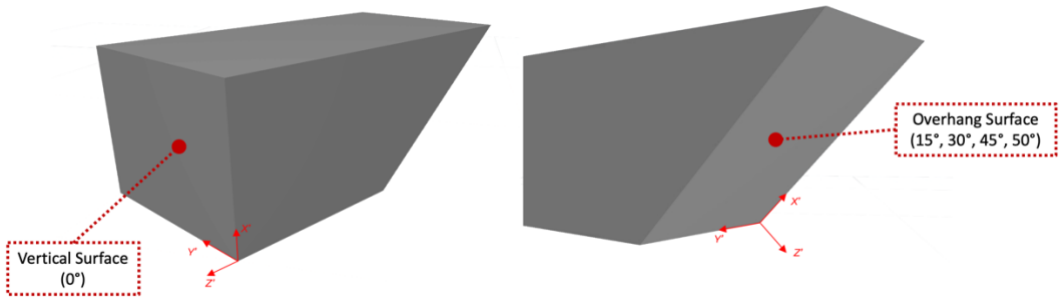

Figure 4.1: Surfaces scanned with Alicona InfinteFocus

The initial parameters that had to be set to start the measurement are detailed in Table 4.1. Furthermore, the machine requires, as input from the user, the definition of a bounding box, that is the area of the specimen inside which InfiniteFocus performs the measurements.

Magnification	Exposure	Contrast	Polarizer	Vertical resolution	Lateral resolution
5x	213 µs	0.27	Deactivated	0.41 µm	7.36 µm
10x	371 µs	0.57	Deactivated	0.10 µm	3.50 µm

Table 4.1: Measurement settings in Alicona InfinteFocus

The scanned areas of the part are acquired by the optical microscope as point clouds, and the three coordinates x, y, and z are associated to each point. To achieve both quantity and variety of data, without requiring excessive time, it was decided to use different resolution modes according to the different area. For the overhang surfaces the resolution power was higher (corresponding to the 10x magnification), and the cleaned clouds of points that reconstruct the surface are on average around 6 million x 3 coordinates. The downskin is the focus of this work and it was necessary to have a better precision. Instead, the Vertical Surface (0°) was acquired with lower resolution power (corresponding to the 5x magnification), and on average, once cleaned, the dataset is formed by 1 million points x 3 coordinates.

4.1.2. Temperature Data

To acquire data while the specimens were under production, the FLIR x6901sc MWIR IR Camera was used (Chapter 3.2.2). The acquisition modes available for this camera are Single Preset and Super Framing. For the analysis of this Thesis, the Super Framing mode was exploited to record the in-situ data, since it has a wider temperature range, by improving the brightness of the thermal image, without

losing thermal contrast, by acquiring more sub-frames in sequence and by combining them in the Super Frame one (*Infrared Imaging*, 2012). Two presets are available, and they are adopted consecutively: the first one has a range from 308 K to 423 K, and the second one from 423 K to 623 K, regarding AISI 316L. Instead for AlSi10Mg the temperatures were lowered to 35 K to 150 K, for the first preset, and 150 K to 350 K for the second. In contrast with the Single Preset mode, no filter is necessary. Furthermore, due to the transfer of data through an ethernet cable, the acquisition frame rate is scaled by a factor of 3, so from the theoretical rate of 2000 Hz, the real value was diminished to 667 Hz for the steel, and to 500 Hz for the aluminum.

Not all the layers have been recorded since the storage was limited. Specifically, four layers, respectively Layer 62, Layer 63, Layer 64 and Layer 65, were acquired at 1860 μm from the base, having all different scan strategies (as previously mentioned, after producing each layer, a 90° rotation of the laser was performed), as depicted in Figure 4.2.

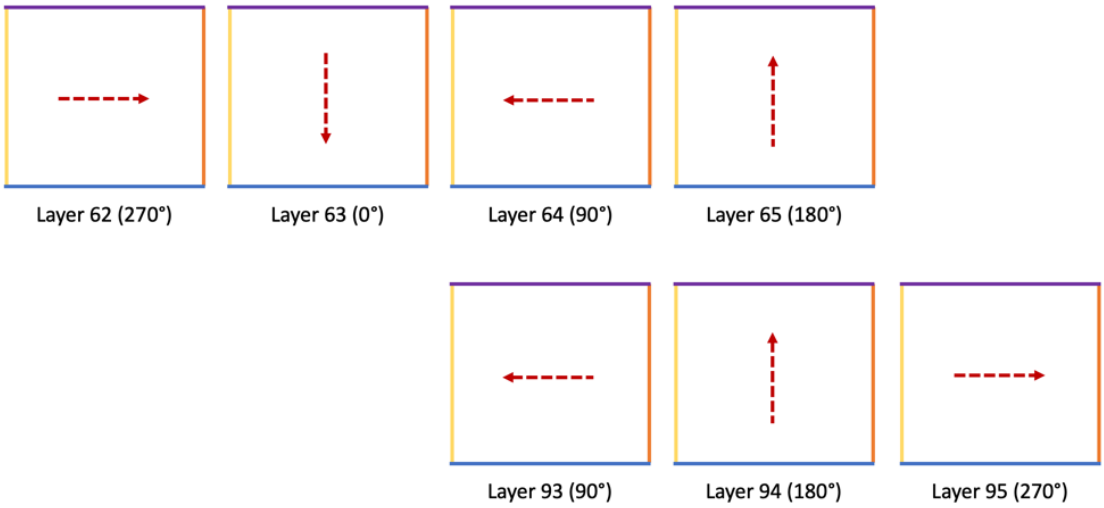

Figure 4.2: Different scanning directions for each layer – in purple and in blue: edges corresponding to the trapezoidal surfaces, in yellow: the edge corresponding to the overhang, in orange: the edge corresponding to the bulk

In addition to them, other three layers (Layer 93, Layer 94 and Layer 95) were acquired at 2790 μm from the base, with only three out of the four scan strategies due to an incomplete acquisition.

Instead, during the production of the specimens in AlSi10Mg (both experimentations), three groups of layers were recorded: Layers from 160 to 163, Layers from 200 to 203 and lastly Layers from 240 to 243, respectively starting from 2000 μm, 3000 μm and 4000 μm from the base.

The video extracted by the IR camera can be considered as a sequence of single frames, and the single frame is in turn a matrix of pixels. Then, mathematically, the videos can be considered as matrixes of three dimensions: m x n x j, where j is the number of the frame, and m x n is the matrix which represent the single image, in which each element is a pixel. The number of frames changes according to the length of the video, instead the dimension of the single frame is fixed to 72 x 224 pixels, while every pixel has a dimension of 240 μm x 240 μm. The final analysis of the videos is performed both on MATLAB and Minitab, but a previous step has to be performed since the format of the files exported by the camera is .ats and the software used to handle it is ResearchIR.

4.2. Data Cleaning

4.2.1. Surface Roughness Data

The second step of data analysis is the cleaning, necessary before going through the data processing. To visualize the point clouds resulting from the measurements, they were represented in a three-dimensional space both on MATLAB and CloudCompare.

Some issues were easily identified, as it can be noted in Figure 4.3a. The first problem to address was the inclination of the samples: in fact, all the specimens were inclined respect to the three principal planes (X-Y, X-Z and Y-Z), as an effect of how the acquisitions of the final parts were conducted. These inclinations had to be eliminated by making the cloud flat: in such way the roughness was entirely on the Z axis, allowing a more sensible and reasonable analysis. The starting point was to find the tilt angles of the point clouds respect to the three principal planes. It was necessary, then, to find a plane that best fitted our 3D point cloud, through the Ordinary Least Square (OLS) methodology.

Secondly, depending on the dimension of the bounding box, the acquisitions included some points on the edges that were out of the area of the analysis. To fully rely on the end results, these points had to be eliminated: the right dataset should include only those points belonging to the interested surface of the specimen. Several trials were performed first on MATLAB, but the required computational time was extremely high (in the order of 20 hours per trial), requiring a different approach. Therefore, it was decided to use an Open Source software: CloudCompare. It was possible to select directly from the image itself the interested portion of points and, as a consequence, to get rid of the other points.

Since now the figures were flattened and cleaned (Figure 4.3b), to complete those preliminary phases, a new reference system was found (X' Y' Z'), (Figure 4.4). This was necessary because all the specimens had different origins according to how the acquisition was performed. For each surface the reference system was determined to have a dextrorse tern, and the dataset centered in the mean height.

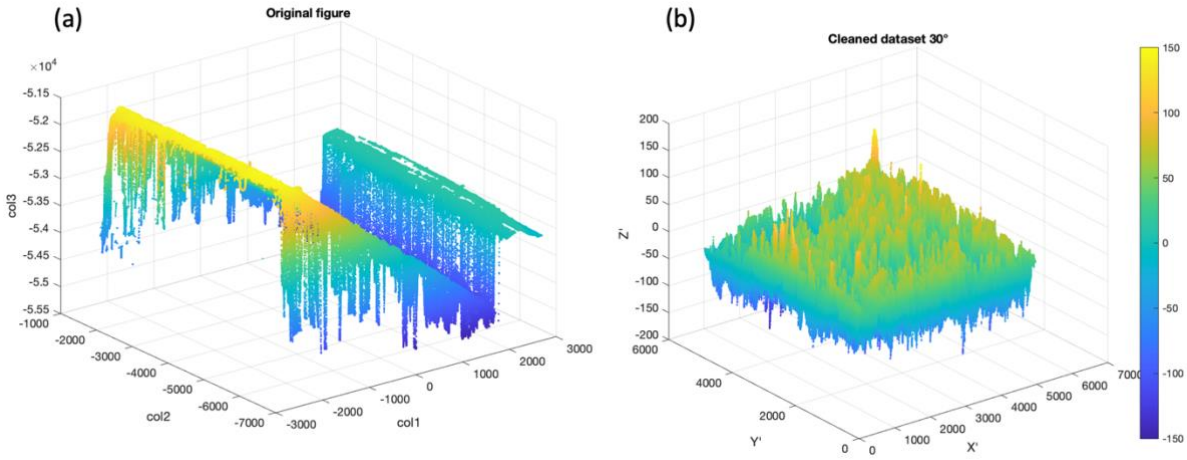

Figure 4.3: (a) Example of overhang dataset scanned with optical microscope, (b) after cleaning process

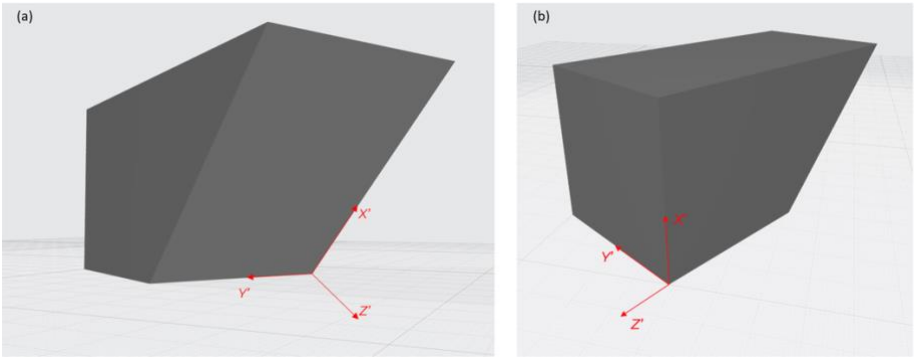

Figure 4.4: New reference systems (a) Overhang Surface, (b) Vertical Surface

The last matter regarding the cleaning phase is about the AISI 316L specimen with overhang angle equal to 45°. Close to the base, it is possible to notice a defect that is considerably higher respect to the remaining part of the surface (Figure 4.5). Once the parameters to explain the surface roughness behavior are calculated, those points were considered as outliers, and therefore excluded from the analysis.

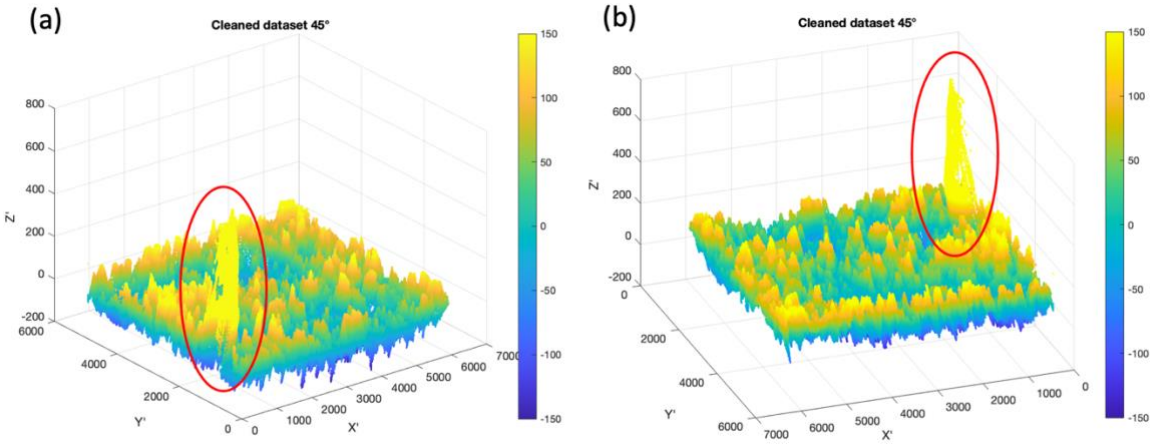

Figure 4.5: Defects present in the specimen with overhang angle of 45° (a) front view, (b) back view

4.2.2. Thermal Data

During the printing process, thermal data were recorded with the Thermal Camera FLIR x6901sc. The total number of printed layers for the AISI 316L specimens is equal to 166, but the correct information store by the camera only regard 7 layers. Instead, the total number of layers for AlSi10Mg is 200, and the recorded ones are 12. By recording consecutive layers, the data about all the scan strategies were acquired.

The videos of each layer are saved from the thermal camera in .ats format, and to process them the ResearchIR FLIR software has to be adopted to export it in different formats. The chosen one is .mat since it can be used on MATLAB, the software exploited for the analysis.

Some necessary corrections have to be implemented, and they regard the calibration of the acquisition parameters.

The first problem that has to be addressed is the emissivity of the surface. Thermal cameras provide an indirect measure of the temperature, based on the radiance, the quantity of energy emitted from the hot source. Every body emits energy in a different way, some bodies emit more energy and some other less. Emissivity (ε) can be defined as "a measure of how efficiently an object radiates heat" (Teledyne, 2021), and it is the ratio between the energy that is emitted and the total energy. Theoretically, emissivity ranges between 0 and 1, which corresponds respectively to a body that reflects all its energy, and to one that absorbs and radiates all its energy, like the sun. Metals like aluminum have a low value, close to 0, because of their polished surface. Because of that, the temperature that the camera detects is

reflected and emanated from the objects around the measured one. This is more critical for lower emissivity, and those values have to be regulated in the camera settings. For this study, the emissivity parameters were set to 0.2 for the bulk and 0.5 for the powder. To establish the moment when the phase transition occurs, and consequentially when ε changes, a temperature threshold is defined. Those values were chosen based on the experiment performed by Mohr et al., (2020), where the authors estimated the most desirable range of values to apply. In particular, for the bulk surfaces the values are from 0.2 to 0.35, and for the powder surface they are higher, from 0.37 to 0.5.

The second calibration required by the thermal camera regards the transmittance of the optical chain. Air does not influence transmittance, but between the IR camera and the specimens, a silica glass (for AISI 316L) and sapphire glass (for AlSi10Mg) divide the two environments where the IR camera is positioned from the PBF machine chamber. It can deaden the signal derived from the measured object.

To estimate the transmittance value to consider in the analysis, the ASTM E1897-97 standard is utilized (Danjoux, 2008).

ASTM E1897-97 (2010) Standard Test Methods for Measuring and Compensating for Transmittance of an Attenuating Medium Using Infrared Imaging Radiometers
1) Set the emissivity to 1.00 and the distance at 0 m. 2) Measure and set the reflected apparent temperature. 3) With the emissivity still set to 1.00, measure the apparent temperature of a hot radiation source. 4) Place the test specimen in between the radiation source and the camera and freeze the image. 5) Change the “emissivity” until the temperature equals the apparent temperature of the hot radiation source. 6) This value is the transmittance. 7) Multiply your target true emissivity by the window transmittance you have obtained, and consider a “global equivalent emissivity”.

Advantages and limitations	• You need a calibrated camera. • The window temperature shall be the same as the original reflected apparent temperature (prevalent before the window is applied). • The technique does not take into account two possible environmental conditions (atmospheric temperature and reflected apparent temperature) on each side of the window.
Note: This standard is also a normative reference for ISO18434-1	

Table 4.2: ASTM E1897-97 standard (Danjoux, 2008)

The hot radiation source exploited for the test method is a tungsten filament of an incandescent light lamp. The final computed value is 0.11 regarding the steel, and 0.86 regarding the aluminum.

Finally, to have the global equivalent emissivity value, the emissivity of the measured object is multiplied by its transmittance. The transmittance in the camera is set to zero since it is already considered in the latter parameter.

Emissivity and transmittance values	**AISI 316L**	**AlSi10Mg**
ε bulk	0.2	0.2
ε powder	0.5	0.5
transmittance	0.11	0.86
global equivalent emissivity	$\varepsilon \cdot transmittance$	$\varepsilon \cdot transmittance$
distance of IR camera from powder bed	520 mm	520 mm
reflected temperature	303.15°K	303.15°K

Table 4.3: Real measurements for in-situ monitoring

Once the videos are recorded and the dataset is exported in the correct format necessary for the analysis (.mat), further cleaning must be performed. As already explain in Chapter 4.1.2, each video can be considered as a sequence of frames. In

each frame, the contour of the layers for each specimen has to be identified and cleaned from the neighboring spatters, otherwise the area considered in the analysis would be wider than the actual one. The result is to have a separated sequence of cleaned frames, saved in distinct matrixes, for each layer and specimen, to analyze them individually (Figure 4.6).

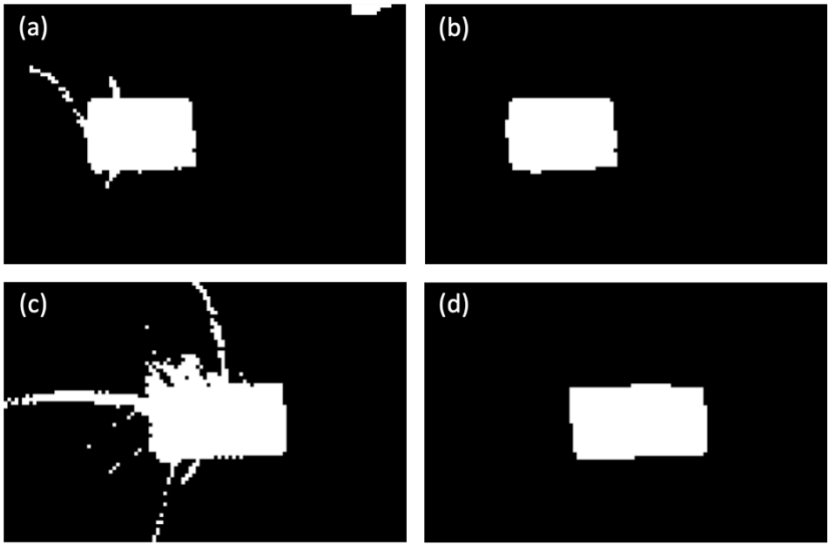

Figure 4.6: Examples of pre-cleaning and post-cleaning contours in Layer 93, (a) pre-cleaning and (b) post-cleaning of specimen with angle 30°, and (c) pre-cleaning and (d) post-cleaning of specimen with angle 50°

4.3. Data Extraction

4.3.1. Surface Roughness Data

Once the cleaning phase was completed, the next step regards the computation of the parameters regarding the roughness of each dataset.

Since the dataset comprehends only four specimens, it was decided to calculate more than one roughness parameter for each sample. For this reason, each surface was divided in multiple squares and for each square the S_a roughness indicator was calculated.

Two different division strategy were adopted. Taking as reference the new coordinate system presented before (Figure 4.4), the first one consisted in considering 20 squares both for the X' and the Y' edge, for a total of 400 squares (Figure 4.7a), while in the second strategy this number was reduced to 25 squares (Figure 4.7b). The reason for the former one is to be found in the direct comparison

with the pixel dimension. With such division the length of a side of the square is 241 μm while the pixel is 240 μm, enabling then a 1-by-1 matching. Indeed, the aim is to directly connect the ex-situ results (roughness parameter) with the in-situ values (the pixel temperature, in this work).

However, being S_a an areal parameter, it requires a minimum number of points to be properly calculated. The problem is that adopting the 20x20 division, some squares were characterized by a low density of points, resulting in non-reliable outcomes, while others had no points at all. For this reason, the second division strategy, namely 5x5, seemed the more appropriate for this analysis. Therefore, from now on, only the 5x5 division is used.

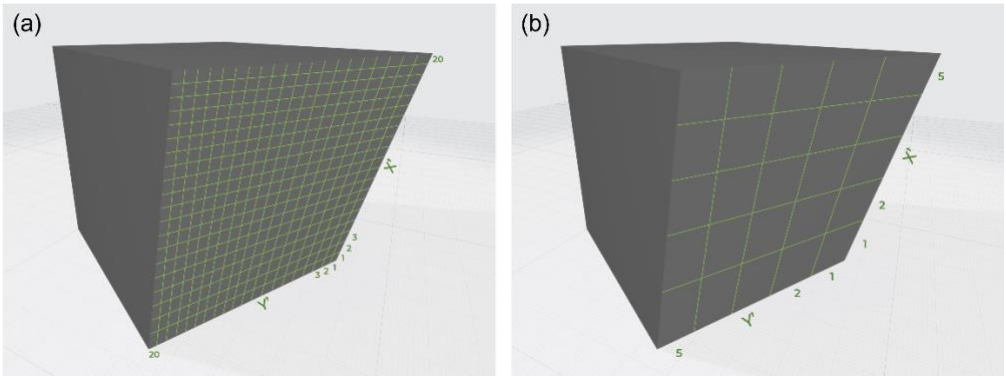

Figure 4.7: Division strategies for the surfaces (a) 20x20 (400 squares) and (b) 5x5 (25 squares)

In Figure 4.8, an example of the applied division strategy for the 45° specimen under analysis is reported.

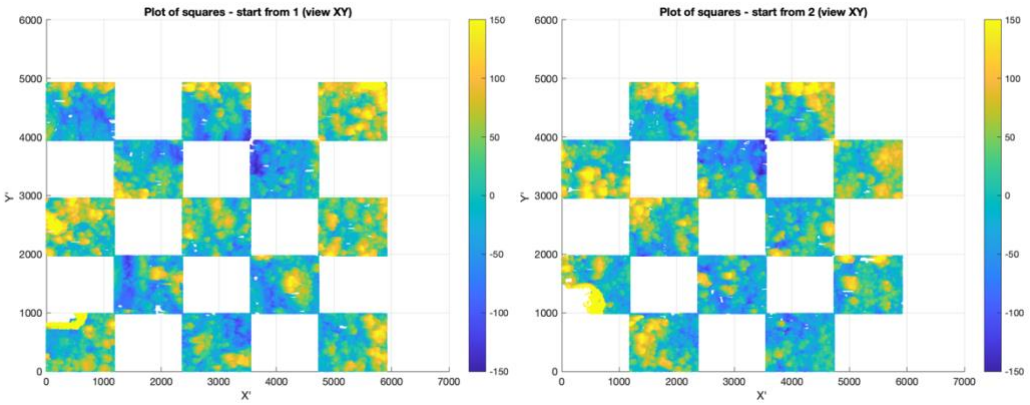

Figure 4.8: 5x5 division strategy for the 45° overhang surface (top view)

As previously noted, the chosen roughness index is S_a, the arithmetical mean height. Its definition is provided in the standard ISO 25178 Surface Texture: "the arithmetic mean of the absolute value of the height from the mean plane of the surface" or,

equally, "the mean of the absolute value of the height of points within the defined area" (Keyence, n.d.).

Mathematically, S_a can be expressed by two equivalent formulas (Lancashire, 2017):

$$S_a = \frac{1}{A}\iint_A |z(x,y)|\,dx\,dy$$ being A the total area and z(x, y) the height function

Equation 4.1: S_a formula

or, in the discrete form:

$$S_a = \frac{1}{MN}\sum_{j=1}^{N}\sum_{i=1}^{M}|z(x_i,y_j)|$$ where (M, N) is the number of points in (x, y).

Equation 4.2: S_a formula in discrete form

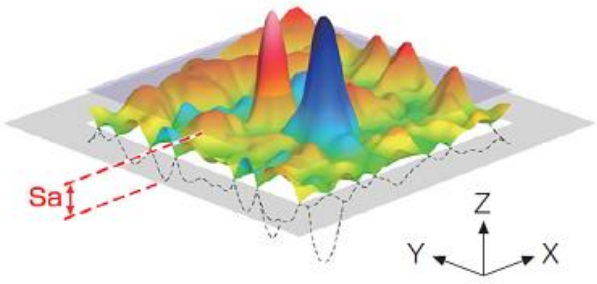

Figure 4.9: Visual interpretation of S_a (Olympus, n.d.)

Although in the present work S_a has been used as parameter for the characterization of the surface roughness, also other indexes were computed, such as S_p and S_v, respectively the height of the highest and lowest point of the surface, or S_q the square root version of S_a.

It is worth to highlight that to properly compute the roughness parameters, the height function must be centered in the mean value (Leach, 2013).

Since the dataset is in the form of point clouds, the second equation is the most appropriate for the evaluation of the surface roughness.

For each square, besides S_a, it is decided to keep track of the relative position of the square itself, by also saving the value of the relative centroid (X' and Y'). The reason for this is to be found in the willingness to evaluate if the relative position of the square influences the corresponding roughness value. From a theoretical point of view, some differences in the S_a value could be present along the X' side, coherently with the printing direction.

4.3.2. Thermal Data

The in-situ dataset to analyze consists in IR videos recorded by the thermal camera during the printing process, composed by multiple successive frames illustrating the temperature of the single layers of the specimens. For each of the four samples, only a total of seven layers was recorded regarding AISI 316L, and twelve instead for AlSi10Mg. Each frame consists in multiple pixels that together give the complete picture of the layer, and each pixel contains the temperature information of a precise point of the surface.

The thermography analysis consisted in the study of the variations and differences in temperature according to different level of analysis. First, the investigation regarded the temperature evolution of single pixels on the surface of the layers in precise locations, which is illustrated in Chapter 4.4.2. Then, instead of considering the whole thermal history, different temperature thresholds were defined to study the extend of time in which each specimen maintained a certain degree of heat.

Focusing on this latter parameter, the Time Above Threshold, it can be described as the portion of time a specific region of the layer stays above a certain temperature limit. The objective was to have an overview of the heat transmitted to the samples during the scanning of the layers, to investigate if some areas maintained a higher temperature respect to others. The selected thresholds were respectively 500 K, 650 K and 800 K for AISI 316L, as represented in the example in Figure 4.10, and 200 K and 400 K for AlSi10Mg.

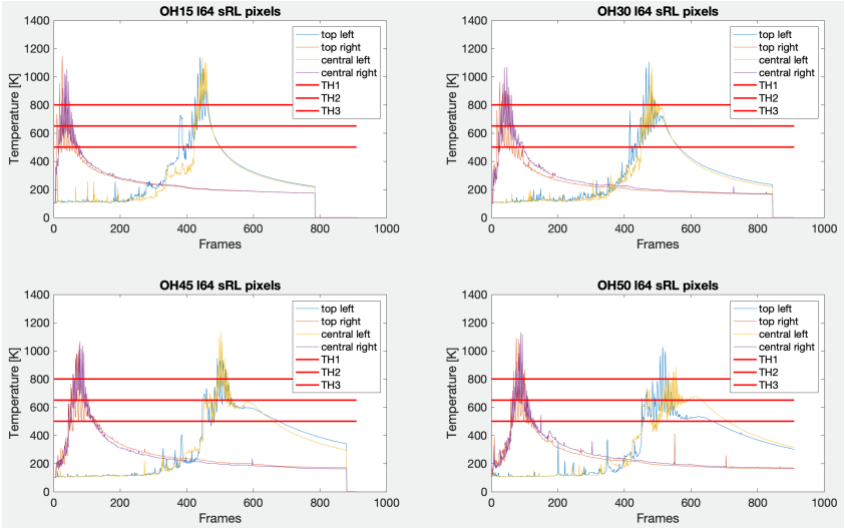

Figure 4.10: Thresholds of 500 K, 650 K and 800 K – Visual example on Layer 64

Previously to the analysis, a data pre-processing is executed. Two aspects had to be considered in the computation of the TAT: the generation of spatters that could randomly rise the temperature recorded by the IR camera, and the periodical

fluctuation of the temperature of the pixels when the laser scanned the nearby regions. Therefore, it is necessary to be careful in the calculation of the number of frames that are considered above the thresholds. The methods, at code level, to overcome those issues are the followings. First, not all the frames were included in the parameter, but only the successive ones, to avoid considering in the TAT also the time where the temperature was above the threshold due to the presence of spatters. Secondly, since the temperature curves of each pixel have fluctuant behaviors due to the movement of the laser, and therefore the temperature does not linearly lower, a moving mean calculation was performed, to include also the contiguous up and downs.

4.4. Discussion of Results

4.4.1. Surface Roughness Data

AISI 316L

The first step is to study the influence of the position of the squares over the resulting S_a value. This is done through a regression analysis in Minitab by evaluating the p-value of both regressors, respectively X' and Y' and considering as response the corresponding S_a. Contrary to expectations, none of the regressors influences the S_a value. The analysis, repeated separately for each OH, shows similar results. An example of the results is reported in Table 4.4 specifically for the less inclined (15°) specimen (Table 4.4a) and for the most tilted (50°) one (Table 4.4b). Even though only these two examples are reported in this work, the general outcome is a p-value higher than 0.05 for all the regressors in all the inclinations, indicating basically a negligible effect of the position of the square on the final surface roughness.

Coefficients (a)

Term	Coef	SE Coef	T-Value	P-Value	VIF
Constant	18,37	1,36	13,52	0,000	
X'	-0,220	0,304	-0,72	0,477	1,00
Y'	0,455	0,304	1,50	0,148	1,00

Coefficients (b)

Term	Coef	SE Coef	T-Value	P-Value	VIF
Constant	39,22	5,01	7,82	0,000	
X'	-0,47	1,12	-0,42	0,678	1,00
Y'	1,88	1,12	1,68	0,107	1,00

Table 4.4: Results of the regressor analysis of S_a vs X' and Y' for: (a) 15° specimen and (b) 50° specimen

With the aim of also having a graphical interpretation of X' and Y', an individual value plot is provided in Figure 4.11 and Figure 4.12. On the x axis, the indication

of the X′ or Y′ is reported. The color of each point represents instead the actual reference square, meaning that the red color is associated to every first square both on the X′ and Y′, the yellow to the second square and so on. Lastly, on the y axis the value of roughness is indicated. The red asterisk shows the mean S_a value for the specific X′ or Y′ line. Visually, no clear trend can be identified both in Figure 4.11 (15° specimen) and in Figure 4.12 (50°), in accordance with the statistical analysis, but only more variability and a general increase for the S_a values of the surface with inclination equal to 50°.

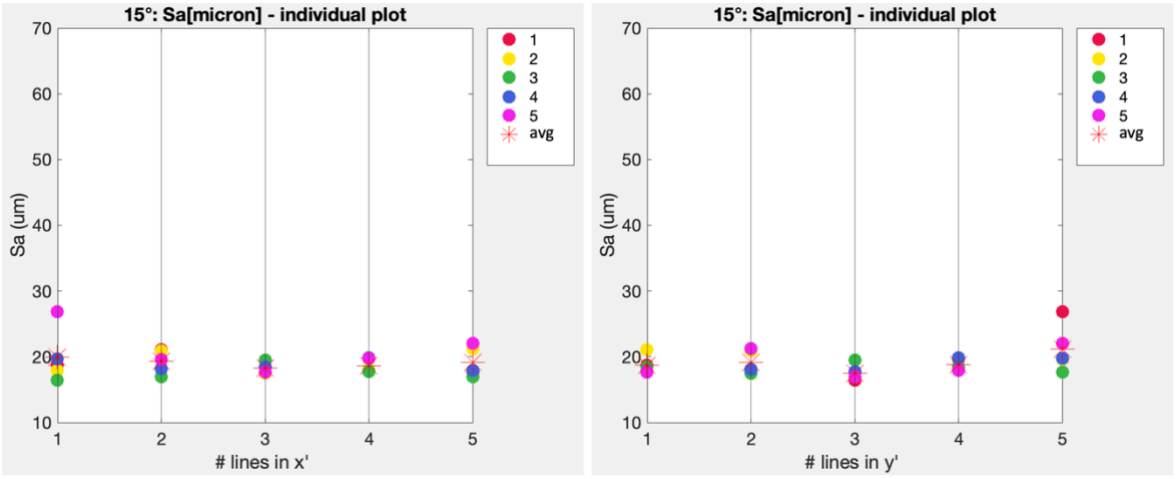

Figure 4.11: Individual Value Plot of S_a values (15°)

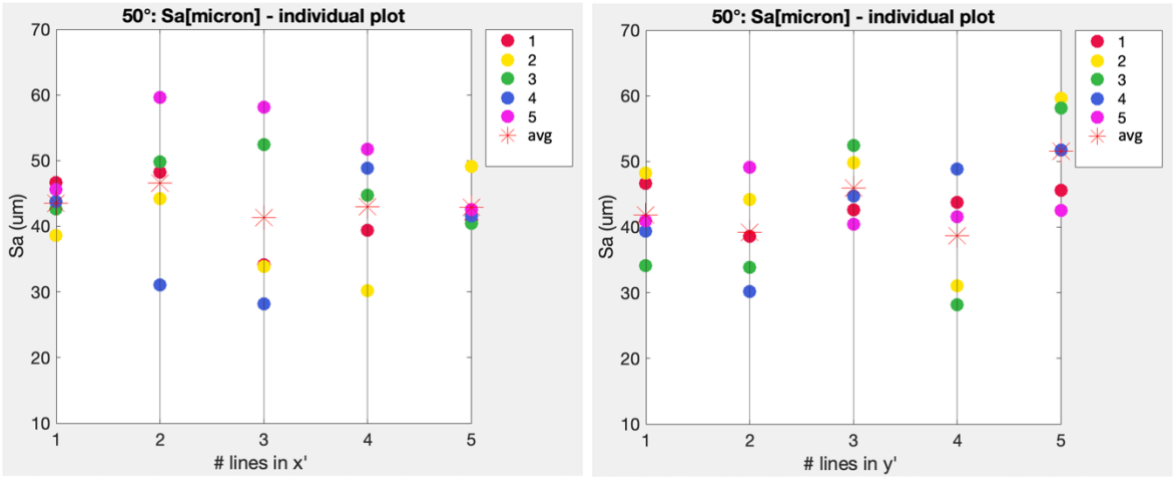

Figure 4.12: Individual Value Plot of S_a values (50°)

At the light of the obtained results, it is possible to consider each square a replica of the same surface. Basically, each surface can be reputed with homogeneous roughness, considering individually the surface with inclination and the Vertical one (0°).

The following step is the connection of the value of S_a found with the corresponding overhang value. All the Vertical Surfaces, as previously said, are considered an extension of the real dataset, having an inclination equal to 0°. The final dataset is therefore composed as follows: 100 observations (25 values for each of the 4 specimens) for the Vertical Surface (0°) and 25 observations for each of the other (15°, 30°, 45° and 50°). This connection is performed through the fitting of a regression model which could directly correlate the values of S_a with the OH regressor. Such regressor takes into account the value of inclination of the different specimens.

It is needed to point out again that the 45° specimen shows a clear printing defect close to the base, influencing the value of S_a of two squares. To properly find a good and reliable model, these points are not included in this analysis. The aim of this work is to consider a general and average behavior, without examining those outliers coming from punctual and stochastic defects.

Prior to the finding of the direct model, a data visualization is needed. This is done by using a scatterplot where on the X axis there is the value of inclination, namely OH (overhang) and on the Y axis the corresponding values of surface roughness indicated as S_a and measured in µm (Figure 4.13).

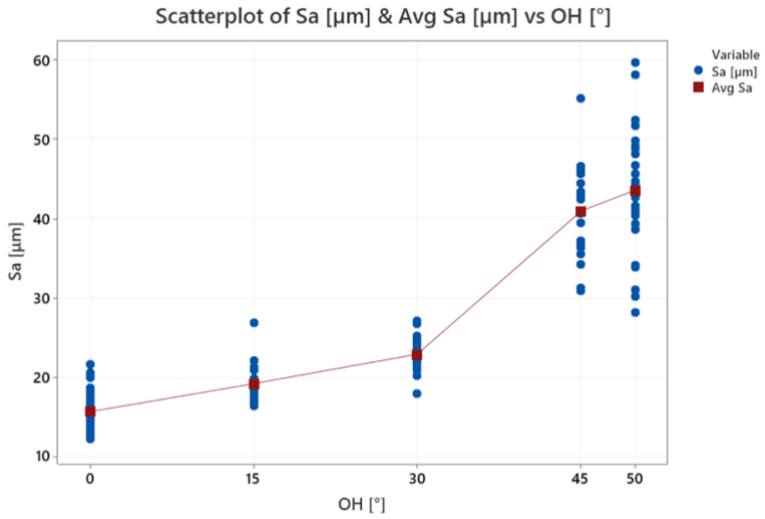

Figure 4.13: Data exploration: scatterplot of OH vs S_a

The first thing that immediately catches the attention is a clear rise in the mean as the inclination increases. In addition, a considerable increment in the values is visible by moving from the 30° to the 45°. This is coherent with the literature that indicates the 45° as a particular inclination (Charles et al., 2019), above which support structures are needed. Furthermore, the variability of the data is higher for the steepest inclinations (45° and 50°).

The model that best fits the data is the one indicated in Equation 4.3. A Box-Cox transformation was necessary to obtain normal regressors. It suggested a value of λ equal to -1.

$$-\frac{1}{S_a[\mu m]} = -0.064892 + 0.000821\ OH[°]$$

Equation 4.3: Regression Model of S_a vs OH

The $R^2_{adj,}$ indicating the goodness-of-fit, is equal to 88.10%.

The Analysis of Variance output confirms the great impact of the OH regressor on the S_a value, with a p-value equal to 0.000.

Analysis of Variance for Transformed Response

Source	DF	Adj SS	Adj MS	F-Value	P-Value
Regression	1	0,052863	0,052863	1459,35	0,000
OH [°]	1	0,052863	0,052863	1459,35	0,000
Error	196	0,007100	0,000036		
Lack-of-Fit	3	0,000616	0,000205	6,12	0,001
Pure Error	193	0,006483	0,000034		
Total	197	0,059963			

Table 4.5: ANOVA of the model in Equation 4.3

To really trust the model, a final evaluation should be performed: the normality check of the residuals. If residuals are not normal, the model is not a good model and the results cannot be considered representative. The Anderson-Darling test indicate the normal behavior of the residuals (p-value = 0.134) and the model can be considered reliable.

In the following graph (Figure 4.14) the model is plotted with the 95% Confidence Interval and the 95% Prediction Interval, respectively the dotted lines in green and purple, while the red line represents the regression fit. Even though some points fall outside the PI limits, globally the model is able to explain the linear dependency of the S_a from OH indication.

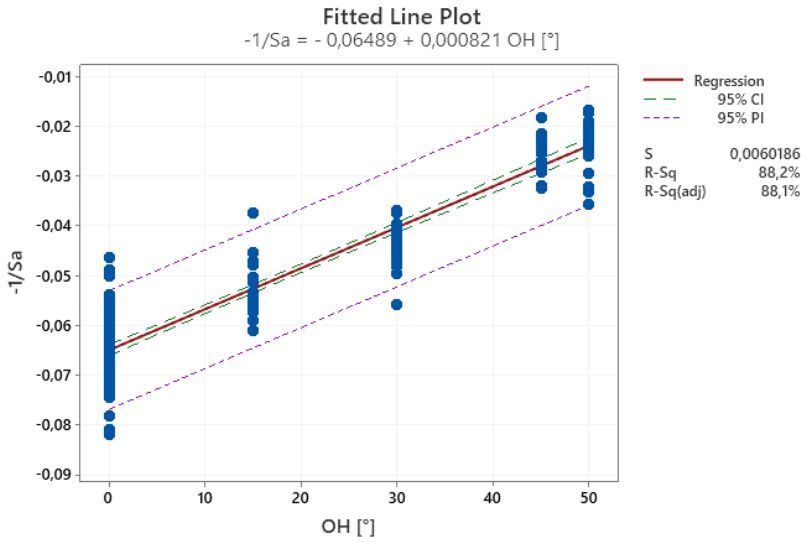

Figure 4.14: Fitted Line Plot of S_a vs OH. Red continuous line: regression line; Green dotted line: 95% Confidence Interval; Purple dotted line: 95% Prediction Interval

AlSi10Mg

The same analysis that was executed for AISI 316L is repeated in this section for the second material under investigation: AlSi10Mg. The analysis of the position of the centroid confirms again how the different squares can be considered replica of each other for all the different inclinations, since nor X', the printing direction, nor Y' have an influence on the squares. This result is proved by the not significant p-values, higher than 5%, in Table 4.6.

(a)

Coefficients

Term	Coef	SE Coef	T-Value	P-Value	VIF
Constant	30,50	2,14	14,26	0,000	
X'	-0,039	0,478	-0,08	0,935	1,00
Y'	0,316	0,478	0,66	0,516	1,00

(b)

Coefficients

Term	Coef	SE Coef	T-Value	P-Value	VIF
Constant	49,25	2,97	16,56	0,000	
X'	-0,339	0,665	-0,51	0,615	1,00
Y'	-0,330	0,665	-0,50	0,625	1,00

Table 4.6: Results of the regressor analysis of S_a vs X' and Y' for: (a) 15° specimen and (b) 50° specimen

To visualize the S_a values of the aluminum and to investigate how they variate according to the different inclinations, a scatterplot is depicted in Figure 4.15. By comparing this graph with the AISI 316L, some differences are noticeable: the variability of the roughness values corresponding to the Vertical Surface (0°) is wider for the AlSi10Mg, and the average value for the 30° sample is greater. The trend seems to assume from the beginning a quadratic form, while the steel had a linear growth for the first three surfaces, and then it grew abruptly in the last two.

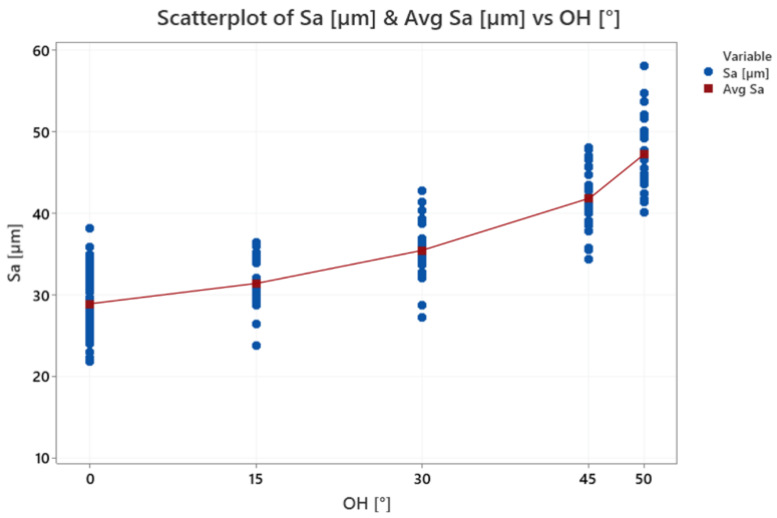

Figure 4.15: Data exploration: scatterplot of OH vs S_a

Hence, the model (R^2_{adj}=77.20%) that best explains the data is quadratic and it is reported in Equation 4.4.

$$S_a\ [\mu m] = 28.819 + 0.0279\ OH\ [°] + 0.00642\ OH\ [°] \cdot OH\ [°]$$

Equation 4.4: Regression Model of S_a vs OH

The ANOVA is reported in Table 4.7. To respect the hierarchy principle, the first-degree term is kept although its low significance. The normality of the residuals of the model is checked and the resulting p-value is 0.074, therefore the obtained regression is acceptable.

Analysis of Variance

Source	DF	Adj SS	Adj MS	F-Value	P-Value
Regression	2	8741,9	4370,95	336,30	0,000
OH [°]	1	3,5	3,53	0,27	0,603
OH [°]*OH [°]	1	423,2	423,22	32,56	0,000
Error	196	2547,5	13,00		
Lack-of-Fit	2	74,4	37,22	2,92	0,056
Pure Error	194	2473,0	12,75		
Total	198	11289,4			

Table 4.7: ANOVA of the model in Equation 4.4

The 95% Confidence Interval and the 95% Prediction Interval in Figure 4.16 explain adequately the variations.

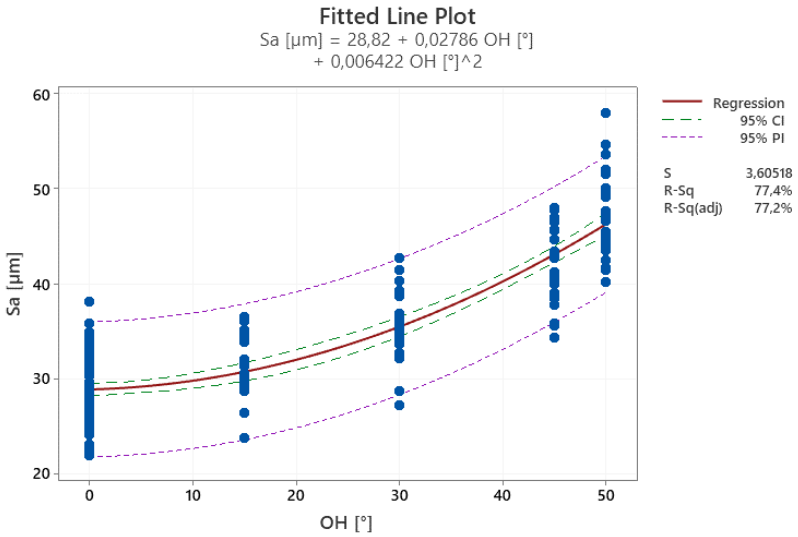

Figure 4.16: Fitted Line Plot of S_a vs OH. Red continuous line: regression line; Green dotted line: 95% Confidence Interval; Purple dotted line: 95% Prediction Interval

Materials Comparison

At the light of the obtained statistical results, a comparison between the behaviors of the two materials is essential. The first noticeable observation regards the surface quality, which is higher for AISI 316L: the lowest reached value is 12.3 µm, against the value equal to 21.8 µm for AlSi10Mg. From the statistical evaluation of the S_a index, a distinct performance is found: the stainless-steel alloy presents a linear growth as the value of inclination increases. This is true until the value of 30°. After this threshold, from the inclination equal to 45°, the behavior seems exponential, coherently with the study by Feng et al., (2021) in which the same attitude was deducted but only from a graphical point of view. The aluminum alloy instead shows from the beginning an exponential trend, indicating a stronger influence of the inclination value on the resulting roughness. The differences then are even more marked if considering the range of observations, namely the variability of the S_a index. The extension of variability for the second material is globally more expanded, even for the Vertical Surface (0°). These latter behaviors confirm how the stainless-steel is more performant in the mechanical applications, justifying its wide usage in the aerospace sector.

4.4.2. Thermal Data

AISI 316L

In the following analysis, even though all the layers and all the scan strategies have been investigated, only the most interesting ones are described, namely the strategy that goes from the bulk to the overhang (Figure 4.17a) and the opposite one (Figure 4.17b).

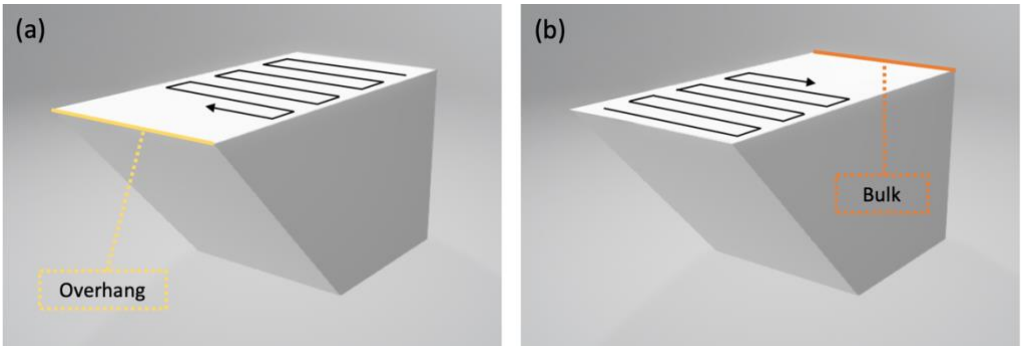

Figure 4.17: (a) Strategy Bulk-Overhang, (b) Strategy Overhang-Bulk

Study of the temperature of single pixels

The data exploration regarding the pixels consisted in the study of the temperature curves, more specifically the evolution of the temperatures at chosen pixels. The initial study concerned four selected pixels representing each contour side of the printed layers, in the interest of investigating the differences among them. Successively, only the pixels positioned on the long edge that connects the bulk to the overhang were considered. They were chosen to examine the transition from the two different regions of the samples.

Differences between the four sides of the specimens

Four pixels were selected for each specimen, in the same positions, named ad “Top”, “Bottom”, “Left” and “Right” as illustrated in Figure 4.18.

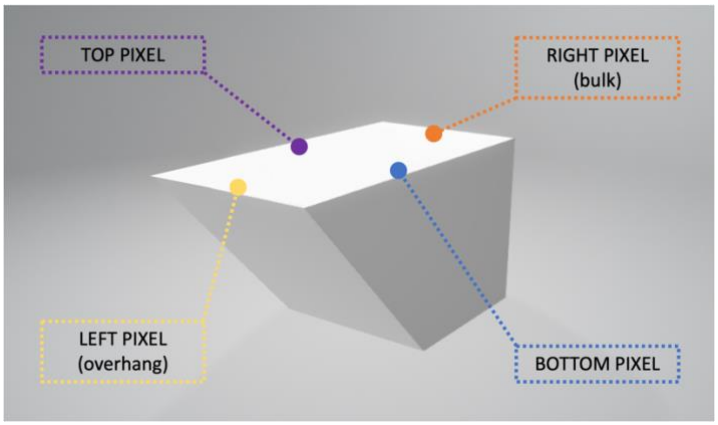

Figure 4.18: Positions of chosen pixels – Top in purple, Bottom in blue, Right in orange, Left in yellow

The aim was to find possible differences in the cooling behavior considering two main factors: the inclination of the sample and the scan strategy. The latter one is critical because according to the orientation of the scanning, the last part of the layer being hit by the laser will have a slower cooling. The most interesting one is the Right-Left strategy because in that case the left side of the specimen is the last scanned part. This part indeed corresponds to the Overhang Surface in the final part, the most critical one. For the purpose of understanding the influence of the scan strategy on the reached temperatures, the thermography analysis was performed for both the groups of successive layers, respectively Layer 62, Layer 63, Layer 64 and Layer 65 for the first group and Layer 93, Layer 94 and Layer 95 for the second, as already described in Chapter 4.1.2.

The adopted approach was a comparison of the pixels in the same position for the different overhang angles (Figure 4.19), repeated for all the layers mentioned above.

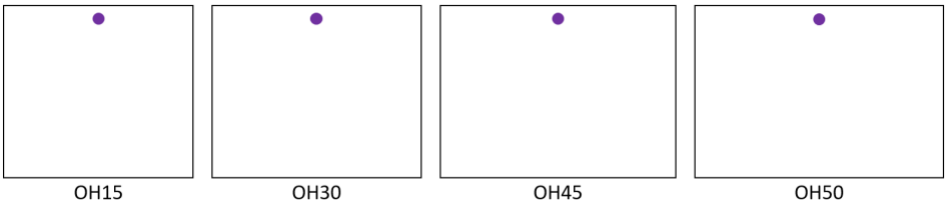

Figure 4.19: Comparison of the pixel in the same position for all the overhang

To execute a reliable comparison, the temperature curves of the different pixels were aligned with respect to the peaks, namely the maximum reached temperatures for the different selected points.

Layer 64 – Strategy: Bulk-Overhang

As said above, for Layer 64 the scanning starts from the bulk part (Right) of the specimen and it ends at the overhang side (Left). In Figure 4.20 it can be noticed how the Left pixels have the most irregular curves compared to the other pixels, for all the specimens. Moreover, for these pixels the central part of the curve, corresponding to the moment in which the laser is hitting the powder, presents an upward trend for all the inclinations. The cooling down part is then coherent with the value of the inclination: the 15° specimen has the most rapid cooling while the 50° the longest and slowest one. It is interesting to notice that the range of fluctuation of the temperature, in the cooling down, is wider for the Left pixels compared to the other positions, being highly influenced by the inclination angle of the downskin surface.

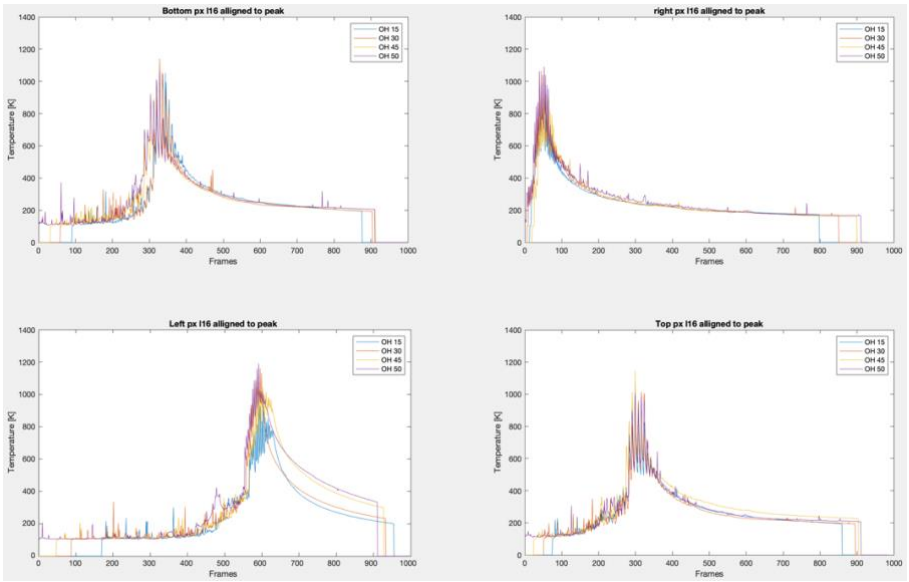

Figure 4.20: Layer 64, strategy Bulk-Overhang, same pixel for each overhang angle

Layer 95 – Strategy: Overhang-Bulk

For the second group of layers it was decided to examine Layer 95, printed according to the opposite strategy respect to Layer 64: in this case the laser starts from the Left part of the specimens, corresponding to the Overhang Surface and it ends with the scanning of the Right edge, the bulk area. Figure 4.21 reports the curves of the temperatures organized according to the position of the selected pixel. The different colors represent the sample under analysis. Also in this case, the influence of the inclination is clear, especially for the pixels overlooking the overhang sides (the Left ones). The specimen with 50° of inclination has the highest curve, symptom of a slower cooling, while the 15° sample shows the most rapid

behavior. It is useful to focus on the opposed behavior of the Left and Right pixels. From the thermal histories it is evident how the Right pixels always have a faster cooling behavior, while the Left ones are characterized by a long and less stable cooling part. This confirms the unusual behavior of the left region of the layer: even though Layer 64 and Layer 95 have an opposite scan strategy, in both cases the Left pixel have the slowest cooling. This depends on the fact that since the left part coincides with the Overhang Surface, in this area the specimen is not able to release all its heat, resulting in a longer cooling down curve.

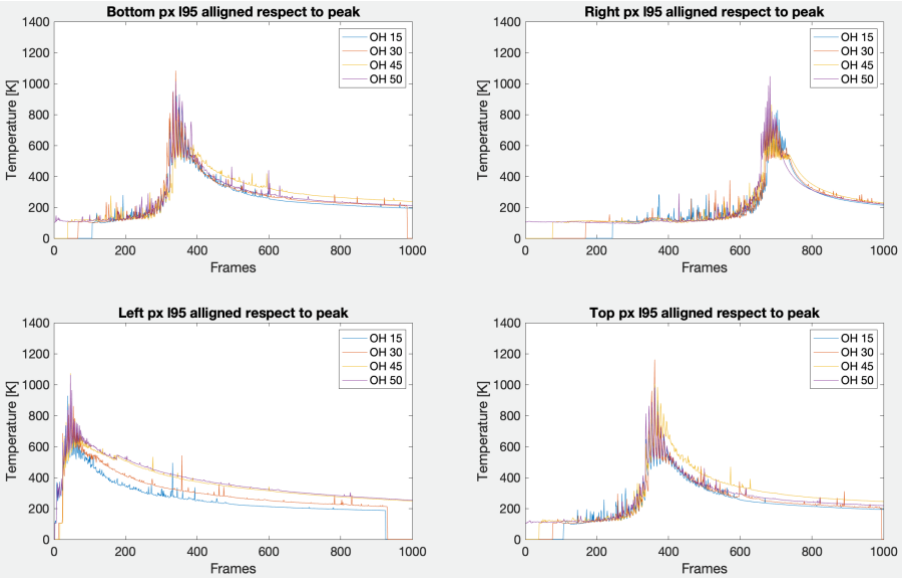

Figure 4.21: Layer 95, strategy Overhang-Bulk, same pixel for each overhang angle

At the light of the found results, it can be confirmed that both the overhang inclination and the scan strategy have a direct impact on the cooling behavior. The novelty is the influence of the relative position of the pixels, especially the Left one belonging to the overhang zone. With the aim of analyzing deeply this influence, the next step was to study the transition from the bulk to the overhang region.

Differences among bulk and overhang

The analysis of the progression from the Vertical Surface (0°) to the downskin area consisted in the selection of seven pixels belonging to the same line in the upper part of the four successive printed layer, as it is illustrated in Figure 4.22a. The same pixels were selected on the opposite line as well (represented in blue in Figure 4.22), and since the behavior is comparable, only the first ones are described. The objective

of the analysis is to investigate how the progression from the bulk to the overhang evolves and the main changes among them.

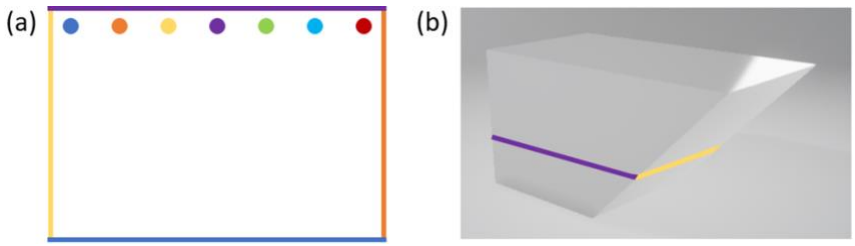

Figure 4.22: (a) Seven TOP pixels chosen (respectively named as: Top-Left, Top Half-left 1, Top Half-left 2, Top, Top Half-Right 2, Top Half-Right 1, Top-Right), (b) 3D view

Layer 64 – Strategy: Bulk-Overhang

The most interesting curves are those of Layer 64, particularly the inclinations at 30°, 45° and 50° in Figure 4.23. Here in fact, the pixels closest to the overhang area (Left and Half-Left 1) present an interesting pattern in the second part of the curve. The blue and orange curve are characterized by a hump during the cooling, likely attributable to the fact that during the cooling itself, part of the heat is dispersed through the already solidified material and not just though the powder. From the analysis of the Left pixel, it is clear how this behavior depends on the inclination, even though the highest curve is the one of the 45° specimen and not, as one would expect, of the 50°. Moreover, looking at the in-situ videos, both the 45° and 50° are characterized by ejected material which melts to the left part of the specimen before the laser hits this area, another justification of this strange cooling behavior.

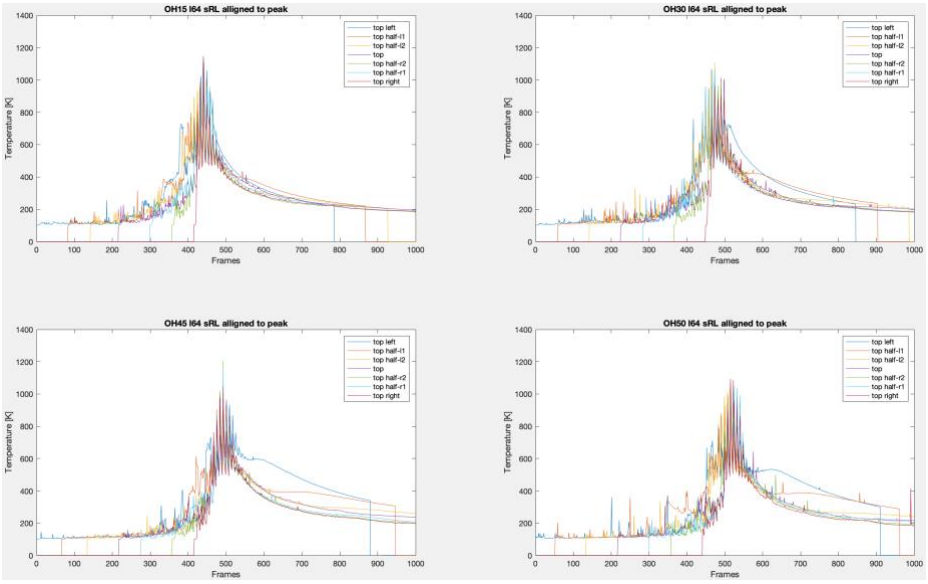

Figure 4.23: Seven top pixels - Layer 64, strategy Bulk-Overhang

Layer 95 – Strategy: Overhang-Bulk

For Layer 95, the differences are not so noteworthy, especially in the heating up part (Figure 4.24). The curves of all the pixels are almost overlapping, except for the sudden increase of the Left pixel, accordingly to the scan strategy. Concerning the cooling down, instead, the differences between the Left and Right pixel are clear: the former shows a slower and longer decay while the latter has an opposite attitude. In general, this behavior is in accordance with the position, with the Left being the highest curve till lowering to the Right one.

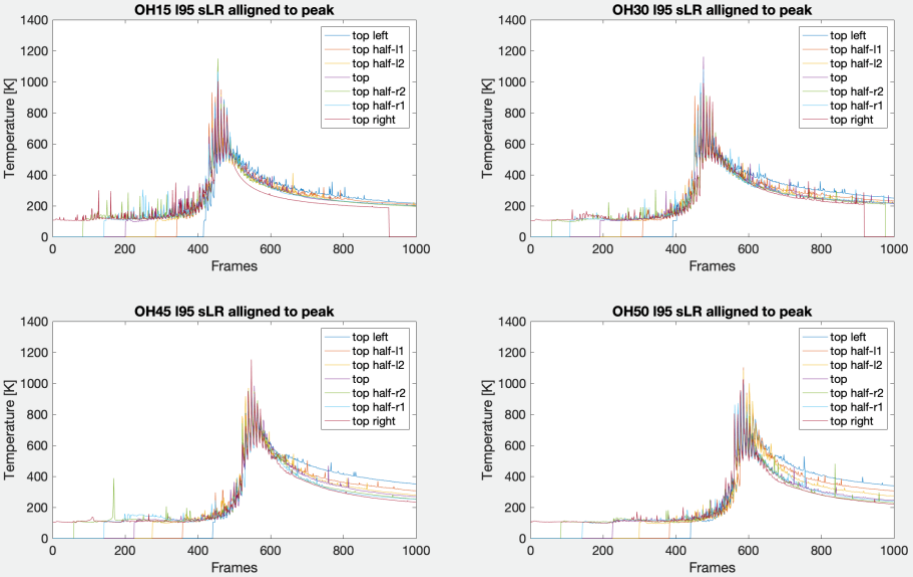

Figure 4.24: Seven top pixels - Layer 95, strategy Overhang-Bulk

Study of the time above threshold temperatures

Since the study of the temperature of single pixels is an extremely punctual analysis that can be subject to variations that depend on the choice of the pixel to analyze, other approaches were performed too. In particular, the most interesting parameter to analyze is the Time Above Threshold temperatures (TAT), defined in Section 4.3.2.

The most meaningful threshold is the one corresponding to 500 K; instead 650 K and 800K gave less information since they appeared excessively dark. Therefore, only this threshold is considered in the analysis.

By following the same structure of the previous section, only two scan strategies, and as consequence only two layers, are described and exploited as exemplifications. The chosen strategies are from bulk to overhang in Layer 64, and

the opposite one in Layer 95. These are the most relevant strategies because in both cases the laser spends more time scanning the overhang part, the one under analysis, either at the end (Strategy Bulk-Overhang) or at the beginning (Strategy Overhang-Bulk) of the production of the layer. The other two strategies instead result in more blurred values. It is worth to notice that, in all the strategies, the left part of the specimen is characterized by higher values of TAT, a symptom of the importance of this part of the layer.

Layer 64 – Strategy: Bulk-Overhang

By representing the TAT of 500 K of Layer 64 for each specimen (Figure 4.25), it can be easily noticed how the area that assimilates the highest temperature is the overhang side, on the left edge of the specimens. However, not all the samples present the same conditions: the heat is influenced greatly by the different values of inclination. The overhang of 50° is the brightest one, instead, the overhang of 15° is slightly warmer than the bulk region. The segment characterized by the longest time above 500 K is sharply divided by the rest of the body, indicating that the part which has underneath the solid metal has an improved thermal conductivity respect to the part of the layer laying directly onto the powder. It is important to specify that this difference is even more accentuated by the scan strategy, since in this circumstance the laser spends more consecutive time on the overhang compared to the other strategies.

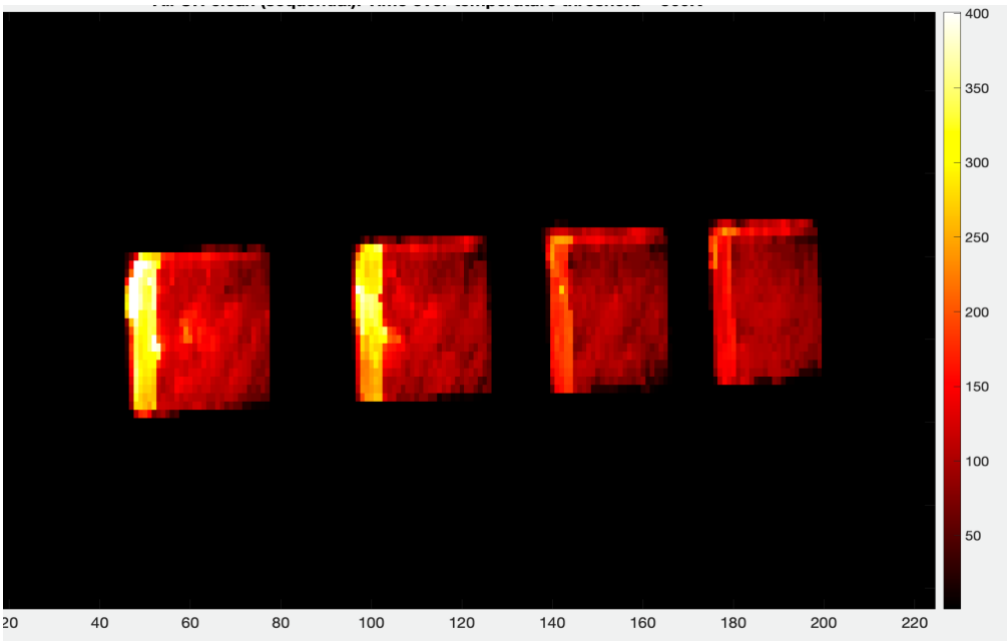

Figure 4.25: Time Above Threshold (500 K) of Layer 64, strategy Bulk-Overhang. In order from left to right: overhang angle 50°, 45°, 30° and lastly 15°.

Layer 95 – Strategy: Overhang-Bulk

This layer is produced adopting the opposite scan strategy with respect to the previously described layer. This means that again the laser heats the overhang for a prolonged span of time, but contrarily to before, this happens at the beginning of the production, when the surface is cold, and therefore the total final heat on the left edge is reduced. In Figure 4.26 the light area is narrower and more blinded with the bulk's temperature. The main differences regard anew the four overhang values of the specimens, having as the most homogeneous one, the 15° sample.

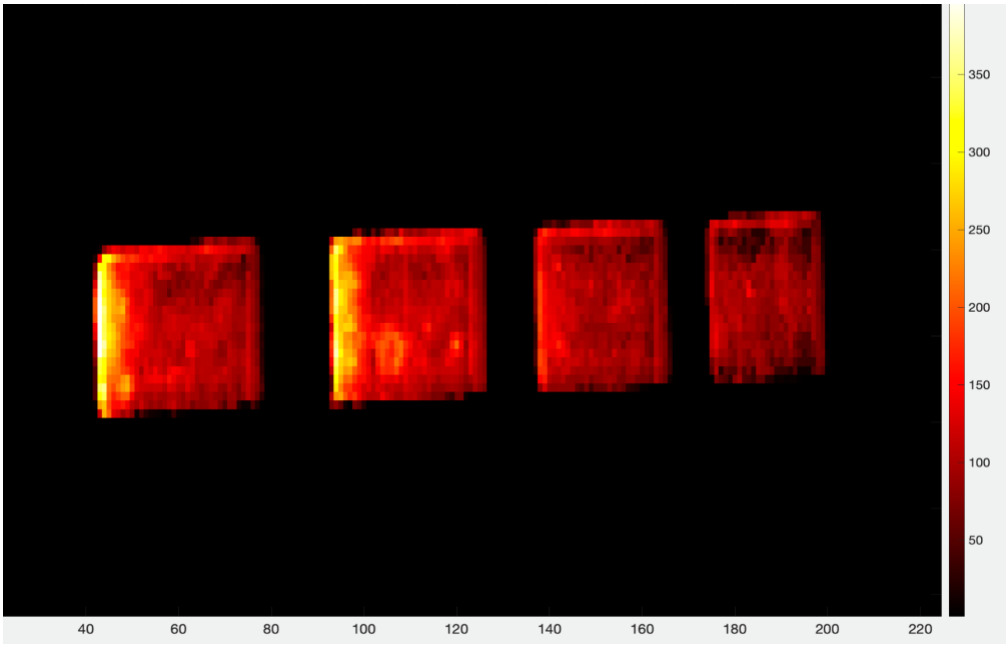

Figure 4.26: Time Above Threshold (500 K) of Layer 95, strategy Overhang-Bulk. In order from left to right: overhang angle 50°, 45°, 30° and lastly 15°.

Statistical Analysis of the Time Above Threshold

To better analyze and to have more reliable results of this new indicator, a statistical comparison was performed in Minitab. The objective was to find some possible differences of the TAT by keeping track of the position of the pixels, the specimen inclinations, and the relative scan strategies of the layers.

The resulting interaction plot is represented in Figure 4.27. The output variable of the General Linear Model is the TAT [msec] of the specific pixel, while the input variables are three: the relative position of the pixel (Left or Right), the inclination of the sample and the scan strategy of the layer. The latter one is codified as follows: B-T for the strategy starting from the lower side of the sample and ending in the top one; L-R when the laser first hits the overhang edge and progressively moves

towards the bulk area; R-L and T-B are the strategies opposite respectively to the L-R and B-T ones.

The graphical visualization of the plot allows to clarify 3 important aspects:

a. The significant importance of the position of the Left pixel, confirmed by the increasing value in TAT of the points in this area respect to the Right ones.
b. The central role of the inclination: by focusing on the Left pixels, those on the down-facing surface, it is clear how the TAT shows an increasing trend as the value of the sample is higher.
c. The key function of the printing strategy. The one starting from the bulk zone and ending on the overhang area, is characterized by the higher values of Time Above Threshold, coherently with the results of the analysis of Layer 64.

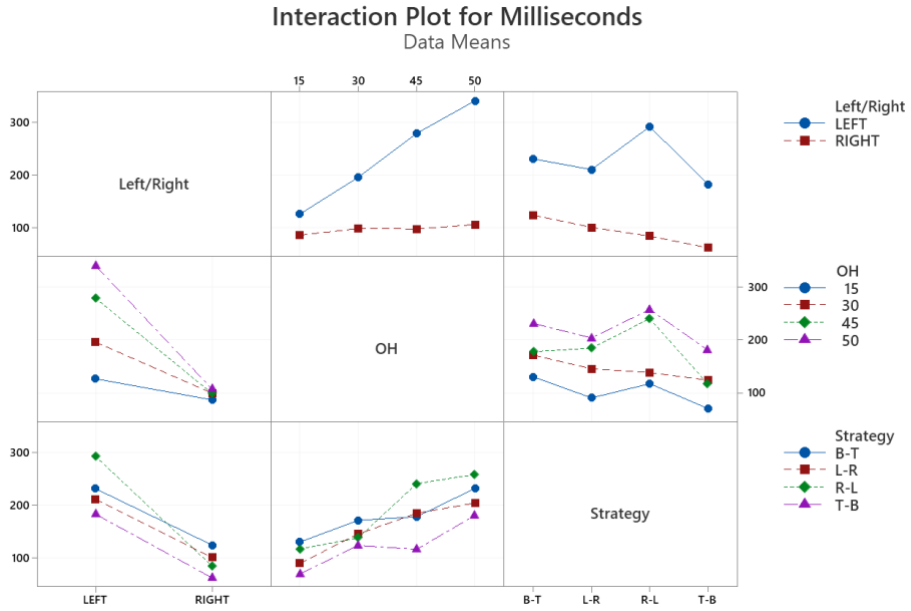

Figure 4.27: Interaction Plot Output. TAT [msec] vs Left/Right, OH Indication & Scan Strategy

The previous results are also statistically supported by the Analysis of Variance (Table 4.8). The three input factors (Left/Right, OH and Strategy) present negligible p-values, indicating their strong influence on the TAT.

Analysis of Variance

Source	DF	Adj SS	Adj MS	F-Value	P-Value
OH	3	217928	72643	22,33	0,000
Strategy	3	53653	17884	5,50	0,002
Left/Right	1	536635	536635	164,99	0,000
Error	104	338270	3253		
Lack-of-Fit	24	260503	10854	11,17	0,000
Pure Error	80	77767	972		
Total	111	1146487			

Table 4.8: ANOVA of the General Linear Model

AlSi10Mg

Differences between the four sides of the specimens

The same thermal analysis in function of the position of the pixels was reproposed for the second material. Again, it is decided to keep track of the two most important strategies: the strategy from bulk to overhang and the opposite one, from overhang to bulk.

Layer 160 – Strategy: Bulk-Overhang

The most significant curves belong to the Left pixels: while the other curves present a more stable oscillating behavior, the Left ones are characterized by a sharp increase in the temperature values in the central part. Moreover, the range of fluctuation is longer for the 45° specimen, which reflects in a longer cooling down for this sample. Focusing on this part of the curve a difference with the AISI 316L can be found. Contrary to expectations, the cooling behaviors do not respect the values of inclination: the sample with inclination equal to 30° has the most rapid cooling, while the other three can be almost overlapped.

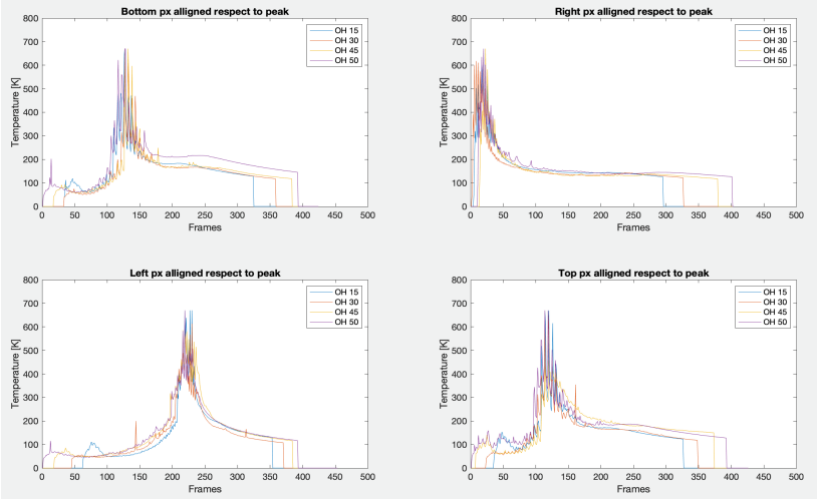

Figure 4.28: Layer 160, strategy Bulk-Overhang, same pixel for each overhang angle

Layer 202 – Strategy: Overhang-Bulk

This layer is printed with the opposite strategy, meaning that the laser scans for a longer portion of time the overhang area at the beginning of the print, as visible in Figure 4.29 by the strong increase in temperature of the Left pixels. Again, a comparison between the Left and the Right pixels is worth. The cooling down part of the Left pixel is coherent with the value of inclination: the 50° specimen has the slowest and longest behavior, while the 15° sample has the most rapid one. The Right ones instead have more irregular curves if compared to the same scan strategy for the AISI 316L (Figure 4.21) specimens. The central part of the curves (when the laser is hitting the specific pixel) is wider and with more frequent peaks and troughs.

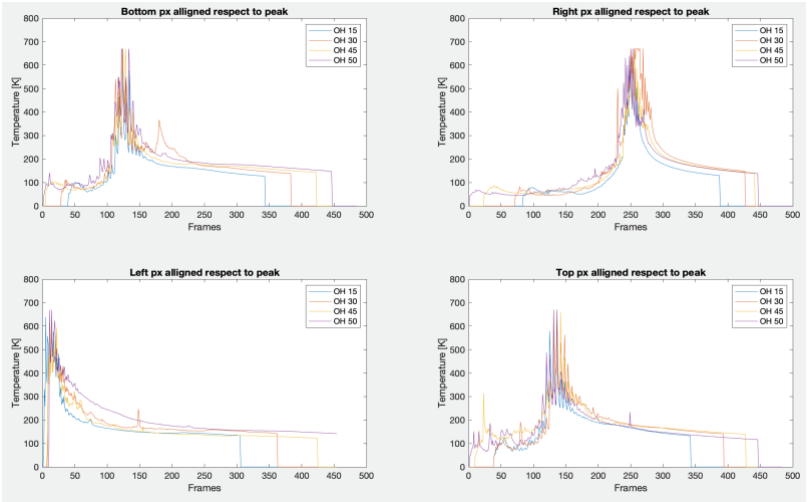

Figure 4.29: Layer 202, strategy Overhang-Bulk, same pixel for each overhang angle

The main differences respect to the temperature curves of the specimens printed with AISI 316L is a general decrease in the reached temperatures and less regular cool-down curves.

Study of the time above threshold temperatures

The Time Above Threshold (TAT) parameter is analyzed also for the specimens printed in AlSi10Mg. For this new material the considered threshold was reduced from 500K to 200K because the general registered temperatures were lower. As previously described, only the most two meaningful scan strategies are analyzed.

Layer 240 – Strategy: Bulk-Overhang

Coherently with the scan strategy used and with the analysis of the previous specimens, Figure 4.30 shows how the left part of the samples are characterized by higher values of TAT. The heat is once again influenced by the value of overhang: the inclination of 50° has the brightest pixels and the segment with the longest portion of time higher 200 K is again clearly identifiable respect to the rest of the specimen. The width of this segment is once more coherent with the value of inclination.

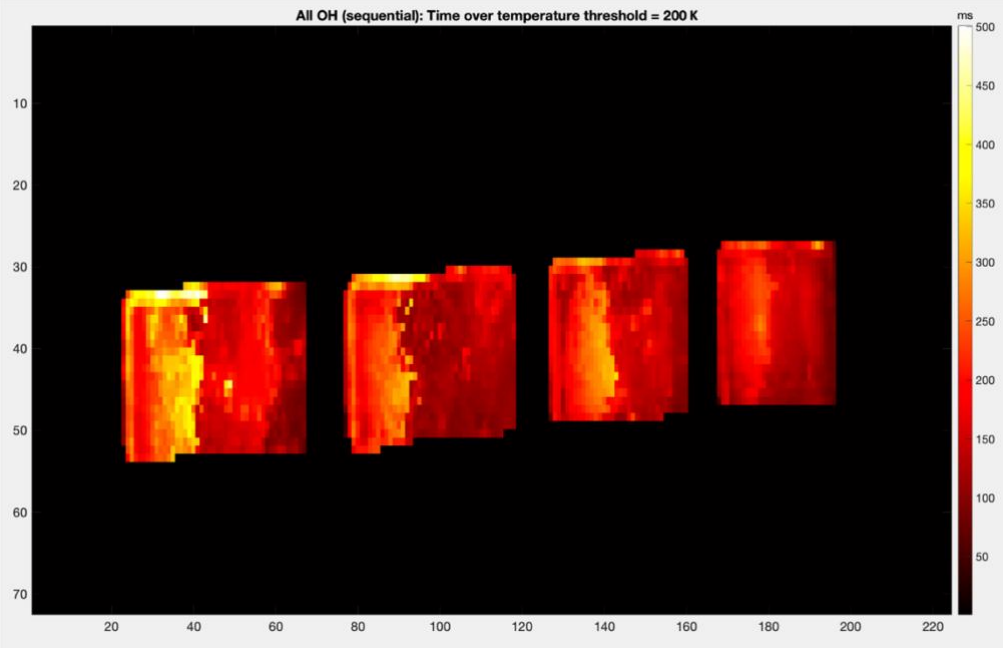

Figure 4.30: Time Above Threshold (200 K) of Layer 240, strategy Overhang-Bulk. In order from left to right: overhang angle 50°, 45°, 30° and lastly 15°.

Layer 202 – Strategy: Overhang-Bulk

The change of the scan strategy has a direct effect on the temperature reached by the different positions and therefore on the values of TAT as well. This behavior is visible in Figure 4.31 where it can be seen how the brightest area of the images is not well defined as in the previous case. The left part shows again high values of TAT but along with it, other areas are affected by this characteristic, indicating a higher variability

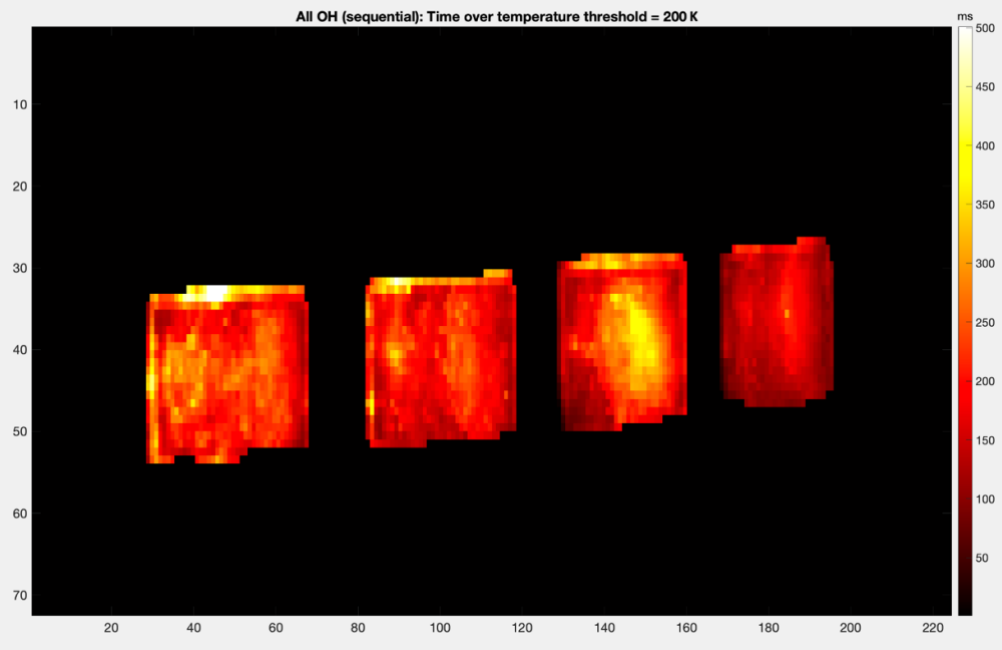

Figure 4.31: Time Above Threshold (200 K) of Layer 202, strategy Overhang-Bulk. In order from left to right: overhang angle 50°, 45°, 30° and lastly 15°.

Materials Comparison

A general comparison between the two materials is needed. Some fundamental differences are observed. Starting from the physical properties, the melting temperature of the steel is higher, reaching 1670 K, and lower for the aluminum, equal to 850 K. This implies different scanning parameters, especially a different total energy density (the former has 4.44 J/mm^2, and the latter 2.22 J/mm^2).

Regarding instead the results obtained in the present work, some considerations can be presented. The thermal thresholds chosen for the two materials are set to 500 K for the stainless-steel and to 200 K for the second one, which implicate different TAT ranges. The AISI 316L has a most regular and steady behavior, both in terms of temperature curves and TAT reached values. The AlSi10Mg instead is

characterized by irregular cooling down curves and thermal images which reflect in TAT values less stable. This is coherent with the ex-situ analysis, where a general increase in the S_a values is evident for the AlSi10Mg specimens, also for the Vertical Surface (0°).

4.4.3. Correlation Ex-Situ and In-Situ

AISI 316L

After having analyzed individually the ex-situ characteristics and the in-situ thermal videos, the analysis that follows deepens the main research objective of this Thesis, the existing correlation between the two. Again, what it is proposed to verify is how the real-time parameters give an indication regard the final surface quality in terms of roughness. The first problem to address is how to consider the two datasets (the ex-situ and the in-situ one) to perform a reliable comparison.

The main issue is that the thermal videos have a top view of the scanned layer, while the ex-situ parameter refers to an external surface. For this reason, in the videos, only the two edges of the scanned layers corresponding to the final vertical and overhang surfaces were considered, respectively the right edge and the left one. A superpixel operation was needed to obtain a number of pixels comparable to the cardinality of the S_a index. This operation consisted in calculating the average value of the TAT indicator of a 2 by 3 group of pixels, as indicated in Figure 4.32 and it was re-proposed for all the available layers. Then, a final mean of the corresponding superpixels for the different layers was considered. In such way, a total number of 5 superpixels was obtained, enabling a direct comparison with the 5 squares of S_a along each X' line. Another problem had to be solved. Since a punctual comparison was not possible, given that the dataset of the thermal videos regards only a limited number of layers, a different approach is used: once it is established that the printing direction has no influence on the roughness values, a S_a average of the 5 squares along each of the Y' lines was computed.

The resulting dataset is then a total number of 5 S_a values for each inclination (20 for the 0°) and 5 values of TAT respectively for the right part of the sample (corresponding to the vertical surface) and 5 for the left one (matching with the overhang surface) for each sample. An exemplification of the previous logic is shown in Figure 4.32 where on the left part (Figure 4.32a) the reasoning behind the computation of S_a is presented, while on the right (Figure 4.32b) the superpixel operation is reported.

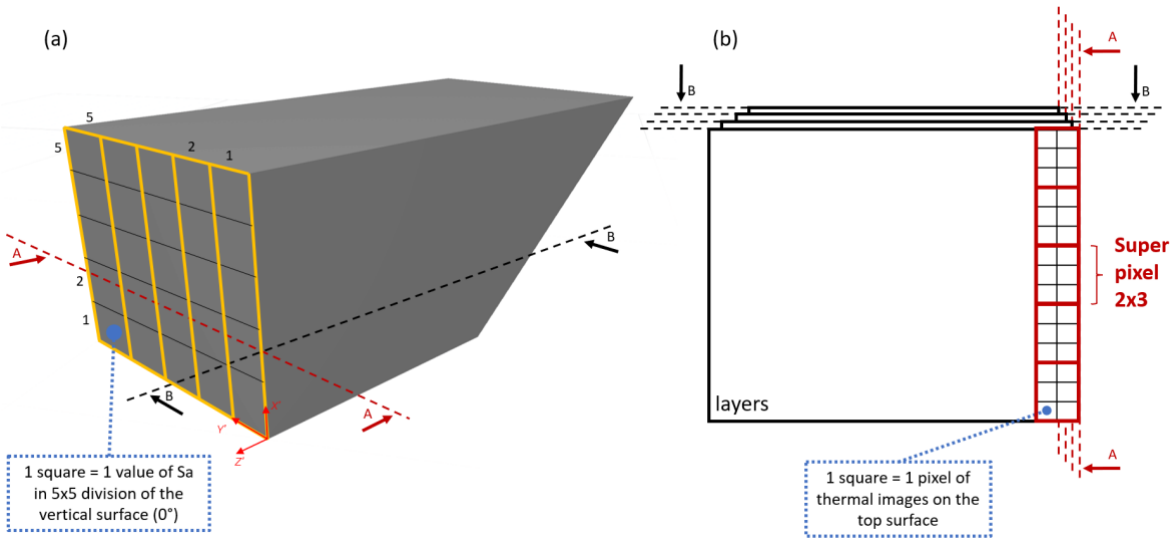

Figure 4.32: Dataset extraction for (a) S_a parameter and (b) TAT indicator

The first step is a visualization and graphical interpretation of the extracted data. Initially, a matrix plot is proposed to investigate potential correlation between the S_a values, the TAT indication and the information of the inclination of the sample. This latter regressor is included since a connection between S_a and OH value is known and widely investigated in Section 4.4.1. As visible in Figure 4.33a, a linear dependency seems evident between all the regressors. The focus instead, as already anticipated, is on the interrelationship among S_a and TAT, the upper-right quadrant.

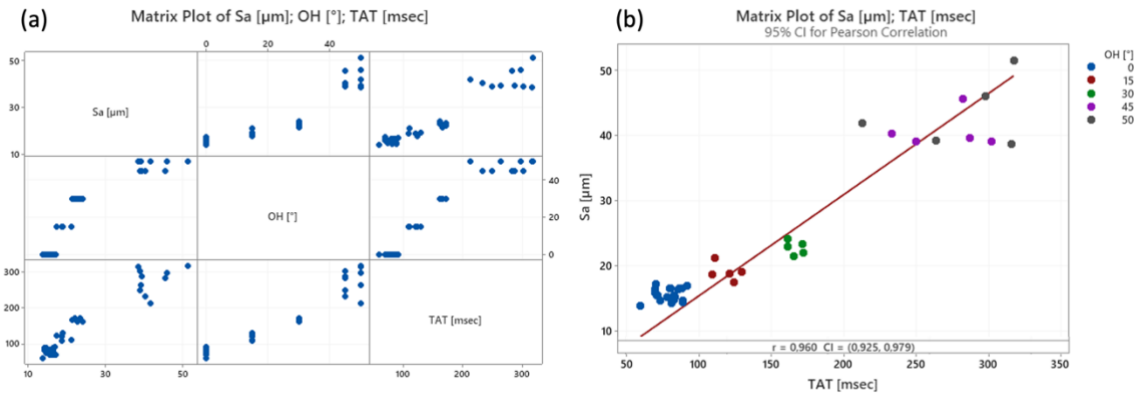

Figure 4.33: (a) Matrix Plot of S_a, OH and TAT indicators; (b) Correlation Analysis of S_a vs TAT

From the graph a clustering behavior is evident. The first thing that comes to mind is that these clusters are coherent with the value of inclination. To further analyze this behavior, the indication of the overhang is used as grouping variable in the matrix plot in Figure 4.33b. The different colors represent the different inclined surfaces. Besides the evident clustering behavior, in accordance with the

expectation, another interesting result is the jump from the 30° to the more inclined surfaces (45° and 50°).

The general outcome is a strong linear dependency between the two. The statistical correlation analysis is computed through the Pearson method. This type of correlation evaluates the so-called Pearson coefficient, or r, given by the Equation 4.5 (Berman, 2018):

$$r = \frac{\sum_{i=1}^{n}(x_i - \bar{x})\,(y_i - \bar{y})}{\sqrt{\sum_{i=1}^{n}(x_i - \bar{x})^2}\,\sqrt{\sum_{i=1}^{n}(y_i - \bar{y})^2}}$$

Equation 4.5: Pearson coefficient formula

where x and y represent the values for the two quantities and n is the total number of observations.

This coefficient can assume values from -1 to +1. Values close to the extremes are symptoms of a strong correspondence between the variables, respectively a negative or a positive one, while the 0 indicates no association at all (Kirch, 2008), (Profillidis & Botzoris, 2019).

The Pearson coefficient estimated in Minitab for the two variables under analysis (S_a and TAT), shows a value equal to 0.960 (Figure 4.33b), a very strong positive correlation between them. This means that high values of Time Above Threshold correspond to high values of roughness and vice versa. In other words, the more the temperature of the specimens stays above a certain value (500 K in this case) in terms of time, the worse the final surface quality will be.

The next step, which is also the main objective of the correlation analysis, is to understand if this real-time parameter, the TAT, can be directly connected to and predict in a certain way the value of the final surface roughness S_a through a regression model.

The regression equation that best fits the observations is the following one:

$$S_a[\mu m] = 5.09 + 0.12480\,TAT\,[msec]$$

Equation 4.6: Regression Model of S_a vs TAT

The R^2_{adj} for the previous model is equal to 91.89%, thus the input variable (TAT) is highly capable to explain the variability of S_a.

The importance of the regressor is verified by the ANOVA output, which shows a null p-value for the in-situ parameter.

Analysis of Variance

Source	DF	Adj SS	Adj MS	F-Value	P-Value
Regression	1	4580,9	4580,86	443,11	0,000
TAT [msec]	1	4580,9	4580,86	443,11	0,000
Error	38	392,8	10,34		
Total	39	4973,7			

Table 4.9: ANOVA of the model in Equation 4.6

The main assumption that has to be verified is the normality of the error terms. The Anderson-Darling Test performed on the residuals, indicates a p-value = 0.483 meaning that the null hypothesis cannot be rejected and the error terms can be considered normal. The model, in essence, can be considered statistically significant.

For the correlation analysis, as well as for the ex-situ part, a fitted line plot is represented in Figure 4.34 to better visualize the observations versus the identified regression model.

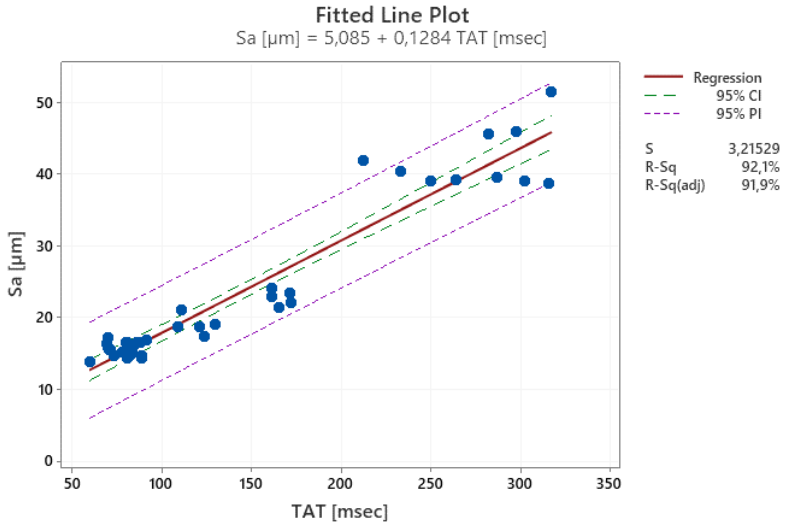

Figure 4.34: Fitted Line Plot of S_a vs TAT. Red continuous line: regression line; Green dotted line: 95% Confidence Interval; Purple dotted line: 95% Prediction Interval

It is clear how the model is very capable of justifying the linear behavior of S_a depending on the value of TAT. Almost all the observations then, fall inside the Prediction Interval, computed with the 95% of confidence level and represented with the purple dotted line in the graph.

Successively, a second model was tested, including both the information of the inclination and the TAT reached value. The idea behind is that this model can be considered an improved version of the one proposed in Section 4.4.1. If the previous

model was based simply on the design specifications of the piece, given that the only needed information was the value of the inclination of the analyzed surface, this new one combines both the design specification and the information of the selected thermal parameter (TAT). The decision to include the thermal indication arises from the formation mechanism of the roughness itself: this surface defect, as discussed in Chapters 1.3 and 2.1, has a direct connection with the overheating and heat accumulation.

The new model is expressed as:

$$S_a\ [\mu m] = \ 24.77\ + 0.457\ OH\ [°] - \ 0.1594\ TAT\ [msec] + \ 0.000499\ TAT^2 [msec^2]$$

Equation 4.7: Regression Equation of the complete model: S_a vs OH & TAT

and it shows a R^2_{adj} = 93.70%.

The ANOVA (Table 4.10) confirms the importance of all the parameters, having all a low p-value. The first order term (TAT) is included in the equation with the aim of respecting the hierarchical model, although it has a high p-value.

Analysis of Variance

Source	DF	Adj SS	Adj MS	F-Value	P-Value
Regression	3	4684,43	1561,48	194,32	0,000
TAT [msec]	1	31,34	31,34	3,90	0,056
OH [°]	1	92,63	92,63	11,53	0,002
TAT [msec]*TAT [msec]	1	92,14	92,14	11,47	0,002
Error	36	289,28	8,04		
Total	39	4973,71			

Table 4.10: ANOVA of the model in Equation 4.7

By analyzing both the R^2_{adj} and the adjusted MS (the error term of the model) it is clear how this expanded version is capable of better explaining the variations of the S_a respect to the previous. Again, since the Anderson-Darling test on the residuals gives a p-value of 0.242, the model can be considered statistically significant.

From a graphical point of view, the 3D scatterplot in Figure 4.35 helps to better understand the impact and influence of both the regressors (OH indication and TAT) on the registered S_a.

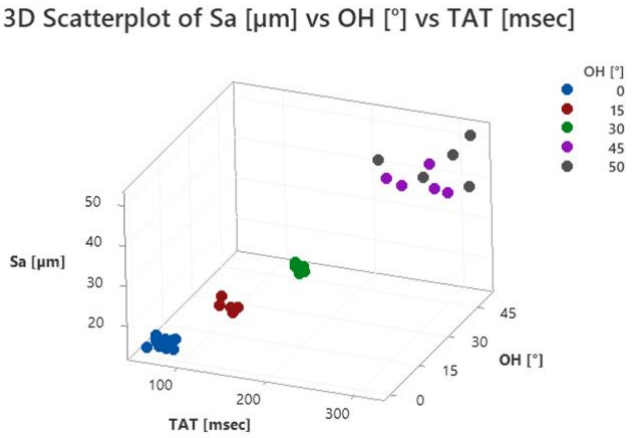

Figure 4.35: 3D Scatterplot of S_a [µm] vs OH [°] vs TAT [msec]

AlSi10Mg

Again, the first needed step is a visual examination of the complete dataset. The same matrix plot, already analyzed for the AISI 316L is reproposed for this material (Figure 4.36a). Focusing on the relation between S_a and TAT, it is clear a different behavior respect to the previous case. This time the correlation between the two variables is clearly quadratic. Figure 4.36b then denotes another difference: the clustering behavior is not so clear, especially for the less inclined specimens. The data belonging to the 0° and 15° can be almost completely overlapped.

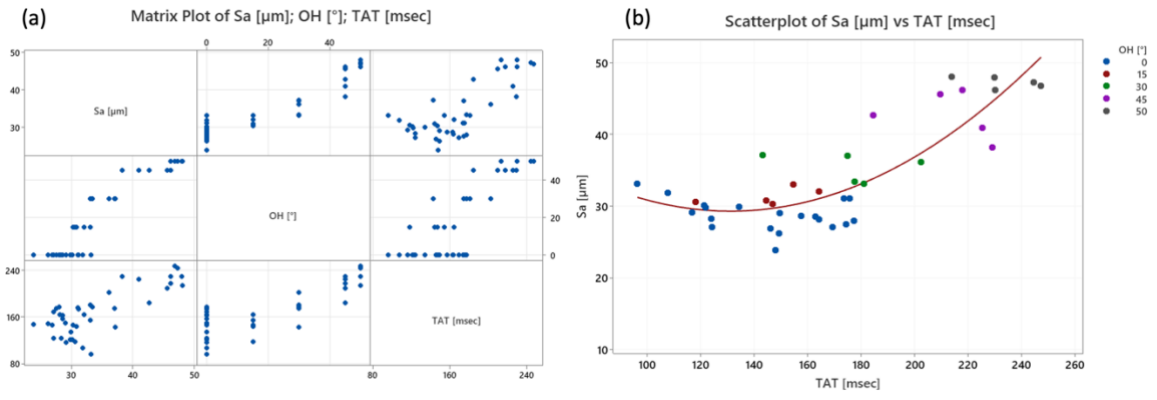

Figure 4.36: (a) Matrix Plot of S_a, OH and TAT indicators; (b) Scatterplot of S_a vs TAT

This quadratic behavior is confirmed by the best fit model expressed in Equation 4.8. ANOVA output (Figure 4.37) indicates that all the terms should be included in the model since they all have a null p-value.

$$S_a\ [\mu m] = 56.6 - 0.417\ TAT\ [msec] + 0.00159\ TAT^{\,2}[msec^2]$$

Equation 4.8: Regression Model of S_a vs TAT

The model capability of explaining the variability of the output variable (S_a) represented by the R^2_{adj} is equal to 71.77% and given that the normality of the residuals is verified by the Anderson-Darling test (p-value=0.172), the results are statistically acceptable.

Source	DF	Adj SS	Adj MS	F-Value	P-Value
Regression	2	1469,1	734,53	50,57	0,000
TAT [msec]	1	153,0	153,04	10,54	0,002
TAT [msec]*TAT [msec]	1	275,6	275,65	18,98	0,000
Error	37	537,4	14,52		
Total	39	2006,5			

Figure 4.37: ANOVA of the model in Equation 4.8

The graphical examination of the model plotted with the 95% of Confidence and Prediction Interval clarifies the strong quadratic correlation between S_a and TAT.

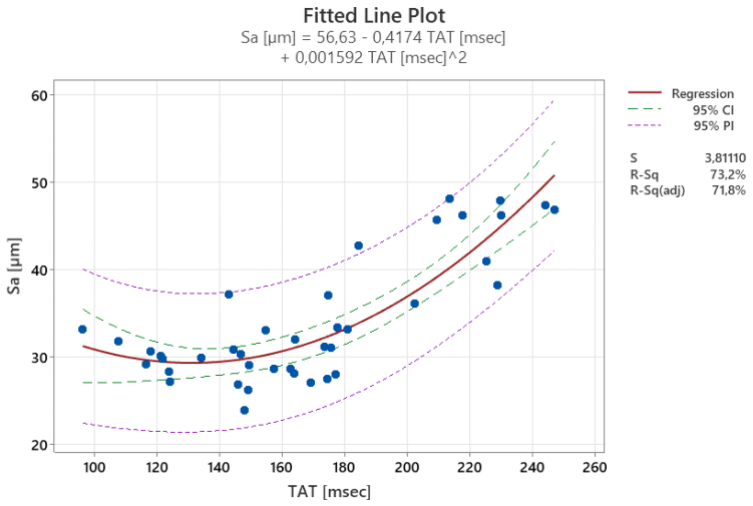

Figure 4.38: Fitted Line Plot of S_a vs TAT & TAT². Red continuous line: regression line; Green dotted line: 95% Confidence Interval; Purple dotted line: 95% Prediction Interval

The model connecting both the information, the overhang value and the in-situ parameter, is re-proposed for the second material as well. Equation 4.9 expresses the relation between the input variables and the parameter under investigation.

$$S_a\ [\mu m] = 48.65 + 0.2802\ OH\ [°] - 0.2600\ TAT\ [msec] + 0.000808\ TAT^2\ [msec^2]$$

Equation 4.9: Regression Equation of the complete model: S_a vs OH & TAT

The great significance of all the regressors is proven by the ANOVA output in Table 4.11. P-values are all almost null, suggesting how the three variables should be all included in the regression equation.

The evaluation of the R^2_{adj} (89.87%) clarifies the goodness of this new model. A comparison between the complete equation (Equation 4.9) and the model including only the design information (Equation 4.4) is needed. A general increase of the goodness-of-fit indicator higher than the 25% suggests a higher capability to estimate the final roughness of the printed parts of the complete model.

The Anderson-Darling test of the residuals confirms the statistical significance of the results: the p-value is equal to 0.834, therefore the normality hypothesis cannot be rejected.

The general outcome is a coherent increase of the S_a parameter with the rise in the OH value and the TAT indicator. The Figure 4.39 allows to visualize and graphically understand this behavior.

Analysis of Variance

Source	DF	Adj SS	Adj MS	F-Value	P-Value
Regression	3	1818,82	606,275	116,32	0,000
TAT [msec]	1	55,88	55,884	10,72	0,002
OH [°]	1	349,76	349,763	67,10	0,000
TAT [msec]*TAT [msec]	1	59,63	59,627	11,44	0,002
Error	36	187,64	5,212		
Total	39	2006,47			

Table 4.11: ANOVA of the model in Equation 4.9

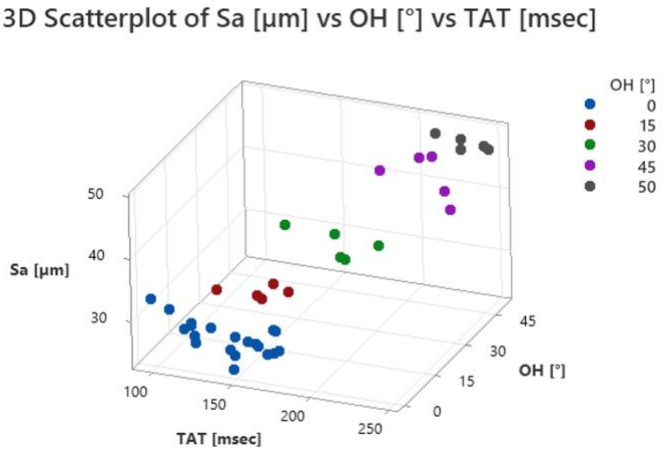

Figure 4.39: 3D Scatterplot of S_a [µm] vs OH [°] vs TAT [msec]

Materials Comparison

The regression models concerning the thermal analysis support the differences already presented in the Section 4.4.1. The proposed models in the thermal analysis aim at connecting the ex-situ resulting roughness (S_a) with the in-situ information (the value of TAT). The model for the steel alloy suggests again a linear dependency between the roughness indication and the regressor. Instead, the aluminum has once more an exponential behavior, suggesting how even comparable levels of TAT lead to much greater values of S_a.

The complete model, connecting both the design parameter and the in-situ information, allows to reduce the disparities between the two materials. Besides some obvious differences in the coefficients of the models, the general behavior is globally comparable: the TAT influences quadratically the roughness levels of both the alloys and, together with the first order term of OH, enhances to better explain the variability in the S_a values of both materials.

4.5. Validation of Results

The current section aims at providing a detailed analysis of the second experimentation in AlSi10Mg, launched with the objective of validating the complete statistical model previously identified, which includes both the design specification (overhang angle), and the in-situ information, the Time Above a Threshold (TAT) temperature. The concept behind it is a more precise and accurate estimation of the roughness values. The model depending only on the overhang indication in fact permits to estimate quite accurately the final quality of the surfaces although, strengthened with the indication of the thermal regressor, it enables to assess more punctually the S_a final value.

What it is proposed to verify with this new experimentation is the inability of the first model to fully capture the differences between the various samples by keeping constant the inclination of the specimen and inducing different thermal stresses during the print. The model depending only on the design parameter has as major limitation the direct connection with the scanning strategy: if different thermal loads and heat accumulations are experienced during the production, the model is not able to capture such changes in the estimation of the roughness.

For this reason, the new print consists of 4 samples produced in AlSi10Mg with a constant overhang angle (45°) but applying for each one a different scan strategy. The divergence lies in the adopted emission strategy of the laser source. The 4

specimens were produced, as already deepened in Section 3.2.1, with: a continuous wave emission and a power equal to 200 W for the CW 0%P specimen, a pulsed wave emission with 160 W, 200 W and 240 W laser power values, respectively for the PW -20%P, the PW +0%P and the PW +20%P samples.

With the intention of comprehending the importance of the thermal indication, the new analyzed dataset includes both the data of the first and the second experimentation in AlSi10Mg. The first needed step is the data visualization by plotting on two separate scatterplots the values of roughness, the S_a indicator measured in µm, and the thermal indication, given by the chosen index TAT measured in milliseconds, both against the different inclinations. The aim is to detect from a visual point of view the interconnections among the two. In Figure 4.40, the results are organized as follows: the blue squares represent the values of the 1st experimentation in AlSi10Mg according to the different inclinations (0°, 15°, 30°, 45° and 50°). The other points, represented as dots, instead come from the second job in aluminum alloy: the angle of the down-facing surface is kept fixed at 45° and the different colors represent the distinctions according to the scan strategy used.

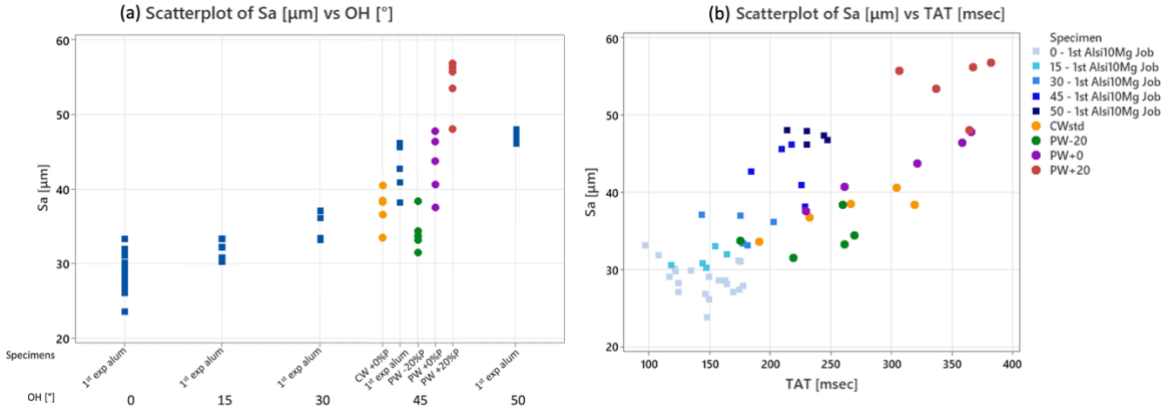

Figure 4.40: (a) Scatterplot of S_a [µm] vs Overhang values [°], including 1st and 2nd AlSi10Mg experimentations, (b) Scatterplot of S_a [µm] vs TAT [msec], including 1st and 2nd AlSi10Mg experimentations

In Figure 4.40a, a great variability for the 45° specimen is clear, coherently with the strategy adopted. The highest values of roughness, as expected, are reached for the pulsed wave emission using the highest value of power (240 W). On the contrary, S_a records a strong decrease if the used power is lowered to 160 W.

Some analogies can be drafted by the visual examination of Figure 4.40b. The red dots, representing the specimen printed using a level of power equal to 240 W, are also characterized by the highest values of the TAT. Furthermore, the specimen

printed instead with lower power has more in-control values of temperatures which reflect in quite low values of S_a.

The successive step is instead a statistical evaluation of the dataset, to study the influence and the importance of the two variables under analysis: the value of inclination and the information about the thermal conditions of the process.

The initial hypothesis that it is expected to prove is how, by including the thermal in-situ indication, the prediction of the final surface roughness significantly improves respect to consider the single parameters alone. Moreover, it can also enhance the limitations that they bear.

The first proposed regression model estimates the roughness indication based simply on the design indication (OH). The second one instead considers as unique regressor the TAT value registered during the production. The principal results are summarized in Table 4.12. Lastly, the final complete model taking as input both the information of the overhang and the in-situ parameter is provided.

	S_a [μm] vs Overhang value [°]	**S_a [μm] vs TAT [msec]**
Model equation	S_a = 28.18 + 0.3202 OH	S_a = 17.78 + 0.09073 TAT
R^2_{adj}	62.59%	64.01%
Standard deviation	5.17803	5.07894

Table 4.12: Summary of the models considering the S_a and TAT parameters individually

The general outcome proves the initial hypothesis. The two regression models which consider individually either the OH indication or the TAT parameter are barely significant if considered separately. The main drawback of the first one relies in the impossibility to capture significant changes in the estimated roughness when, for the same geometry, several thermal conditions are introduced. The second regression instead does not recognize as equal the constant overhang angles if the imposed scan strategy is different, being it dependent only on the in-situ indication.

As result of these limitations, the model combining both the two characteristics is provided. Coherently with expectations, the prediction of the roughness value is strongly enhanced if the complete model is used. The R^2_{adj} in fact is equal to 76.96%, an increase of more than ten points percentage respect to the previous single models.

The complete regression, obtained with a Box-Cox transformation with λ=-1, is reported in Equation 4.10.

$$-\frac{1}{S_a[\mu m]} = -0.03859 + 0.000025\ TAT\ [msec] + 0.000179\ OH\ [°]$$

Equation 4.10: Regression Equation of the complete model: S_a vs OH & TAT

The influence of all the regressors, confirmed by the low p-values, is deductible by the ANOVA output (Table 4.13).

Analysis of Variance for Transformed Response

Source	DF	Adj SS	Adj MS	F-Value	P-Value
Regression	2	0,001678	0,000839	99,52	0,000
TAT_puls	1	0,000090	0,000090	10,64	0,002
OH_puls	1	0,000360	0,000360	42,75	0,000
Error	57	0,000481	0,000008		
Total	59	0,002159			

Table 4.13: ANOVA of the model in Equation 4.10

The statistical significance of the model is instead verified by the normality of the residuals. The results of the Anderson-Darling test indicate a p-value equal to 0.435.

To study the influence of both the regressors on the reached S_a value, a contour plot (Figure 4.41) allows to clarify the changes in the roughness index in function of the different values of the input variables. Both the contour plot of the resulting model (Figure 4.41a) and the contour plot of the transformed dataset (Figure 4.41b) are represented. The similarities between them are evident: from the model it is clear how the lower values of S_a, thus a higher surface quality, can be reached with a reduction in the TAT, in other words by decreasing the energy input from the laser source. This phenomenon has a lower limit, deductible by the transformed dataset, dictated by lack-of-fusion defects which may occur.

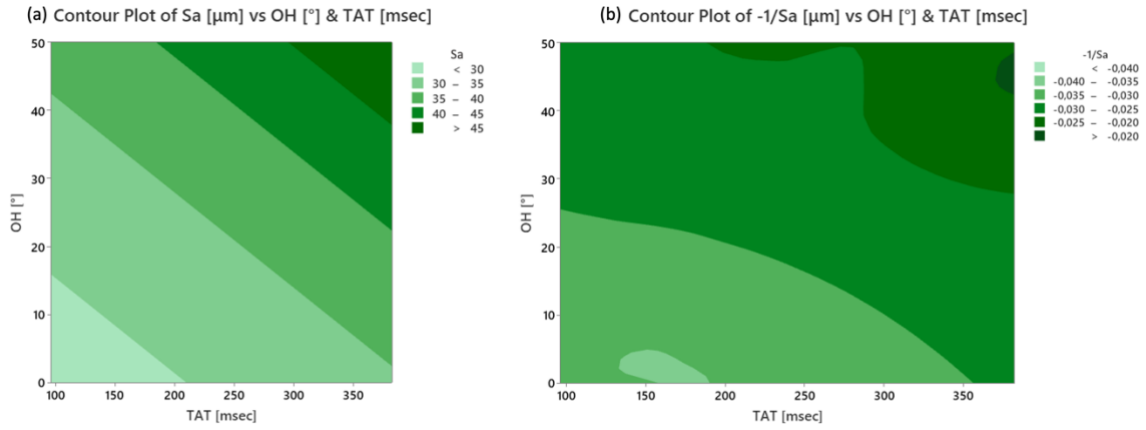

Figure 4.41: (a) Contour plot of the model in Equation 4.10, (b) contour plot of the transformed dataset ($-1/S_a$)

Overall, the results confirm the fundamental importance of taking into consideration both information, the geometrical specification indicating the value of overhang angle and the thermal parameter. The combination of such characteristics allows to significantly improve the assessment of the surface quality of L-PBF printed samples.

Conclusions

Additive Manufacturing is one of the main disruptive technologies born with Industry 4.0. Its wide application is due to its great capability of producing complex and very intricate structures with relatively low costs and time. However, one of the main concerns that AM is still facing nowadays relates to the final quality of the printed parts, in particular the roughness of down-facing surfaces. A combination of different factors such as the inclination of the surfaces, the overheating phenomena and the thermal stresses originated in these areas during the production, negatively contribute to the resulting surface quality of the printed components.

The single impact of the overhang information, the value of the inclination of the downskin surface, on the final roughness is the most studied in the literature. Although a negative correlation between them is known, meaning that more inclined surfaces result in a worst surface quality, a proper model which connects this information with the roughness itself is not found yet.

Instead, the study of the influence of thermal phenomena on the final roughness is almost completely unexplored. Only few authors examined the dependency of the surface quality from the heat accumulation. Furthermore, the majority of them correlate these in-situ characteristics with the quality of the on-going layer, without extending the analysis on the roughness of the final printed part.

The aim of this work is to cover the lack of knowledge about this topic. In this respect, the production of four geometries is analyzed. The samples were produced with the 3DNT industrial L-PBF machine in the Mechanical Department of Politecnico di Milano using two different materials, AISI 316L and AlSi10Mg. The in-situ parameters are extracted from thermal videos captured by an IR camera recording the layer-by-layer production.

The first proposed study tries to correlate the resulting roughness value with a design parameter: the value of the inclination of the tilted surface. The found regression model suggests that even though a linear correlation between the two parameters exists, the connection is not so straightforward. The two materials, then, have a different behavior. For the AISI 316L, if the linear trend is clearly visible for the first inclinations (till 30°), passing from the 30° to the 45° an evident jump in the observations is noticeable. Regarding the specimens printed using AlSi10Mg, this

linearity is absent even in the less inclined samples. The dependency, as the best fitting model suggests, is actually quadratic.

The in-situ analysis aims to examine and understand how different points on the scanned surface behave from a thermal point of view according to their relative position. Even though there is a dependency in line with the used scan strategy, a common attitude for the left pixels is found. These pixels correspond to the overhang regions and they show the highest Time Above Threshold and the slowest cooling down behavior. This latter performance is likely attributable to the fact that the overhang regions accumulate more heat respect to the other areas, and they maintain a higher temperature for a longer time. The influence of the overhang value should not be underrated: from the visual interpretation of the TAT is clear how the 50° sample shows the highest values of TAT which attenuate as the inclination reduces.

The last part of the study is dedicated to the principal focus of this work, the direct correlation between some parameters extracted during the production with the final surface quality. Initially a model which directly correlate these two information is proposed individually for the two materials. Concerning the samples produced with AISI 316L, a strong linear correlation between the parameters is visually detectable and confirmed statistically both by the Pearson Coefficient ($r = 0.960$) and the proposed regression model linking S_a with TAT. The same analysis carried out on AlSi10Mg led to a different result: there is a quadratic dependency of S_a from the TAT regressor, highlighted by both the graphical inspection and by the regression model.

A new model is then proposed for the two materials, taking as input variables both the design parameter and the in-situ measure. Such model can be considered an expanded version of the first one, leading to a more punctual and accurate estimation of S_a. Not only the two models for the two feedstocks have more similarities, but also the R^2_{adj} significantly improves for both the materials, indicating how the addition of the in-situ parameter considerably enhances the evaluation of the surface quality roughness.

The results suggest that the two materials have two different behaviors if either the design or the temperature parameter are analyzed individually. Instead, by considering these two characteristics together, these differences are less marked.

The importance of the thermal information is confirmed by a third experimentation. At the same angle of inclination of the previous tests, different thermal properties are induced, demonstrating how the design and the thermal indication, if considered individually, are not able to fully catch variations of the resulting roughness.

Limits and Future Works

This work lays the foundation for an unprecedent level of analysis. In-situ characteristics and indicators are used as basis for the estimation of the final surface quality of down-facing surfaces.

Starting from these findings, several developments can be taken into account.

It is important to take into consideration that the analyzed samples are four, one for each overhang angle, for each material, with a total of eight specimens. The repetitiveness is therefore not elevated due to a time limit. To strengthen the results, it would be useful to repeat the same experiment to have a higher number of observations, reduce the variability and increment the accuracy of the work.

Moreover, the absence of a multiple dataset for the same level of inclination does not permit to apply a Classification algorithm by exploiting Machine Learning. Since these algorithms require large amounts of input data to be considered reliable, one possible solution is again the print of other specimens with the same shape of those used in this work. The complete dataset can be then divided in a training set and a test set for the construction of a trustworthy classification algorithm, based again on the in-situ thermal information.

The different analyses performed in the present thesis can be re-proposed with the study of components printed in different materials. In such way, possible similarities and common behaviors among metals can be found.

Lastly, it is useful to focus on two important aspects which investigation was began in this Thesis and that can be continued in future works. The first one regards an interesting behavior of the variation of the heat. It was noticed how the baseline temperature curves, namely the fitting curve passing through the valleys of the temperature curves, show different trends according to the scan strategy and the position of the selected pixel. The indications about the coefficients of this curves could give attractive information on the overheating and heat dissipation.

The second requires instead a very punctual analysis. The idea is to study the transition from the bulk to the overhang area. In this case the ex-situ acquisition should be performed on the surface adjacent to the Vertical and to the Overhang one, the trapezoidal vertical surface among the two. Such acquisitions then should

be directly compared with the thermal information of the corresponding pixels along the long edge of the layer. A 1-by-1 matching between each pixel and the roughness indicator is therefore necessary.

Bibliography

Abdulhameed, O., Al-Ahmari, A., Ameen, W., & Mian, S. H. (2019). Additive manufacturing: Challenges, trends, and applications. *Advances in Mechanical Engineering*, *11*(2). https://doi.org/10.1177/1687814018822880

Altenburg, S. J., Scheuschner, N., Maierhofer, C., Mohr, G., & Hilgenberg, K. (2020). *Thermography in laser powder bed fusion of metals: time over threshold as feasible feature in thermographic data*. 1–5. https://doi.org/10.21611/qirt.2020.005

Anisotropy. (n.d.). https://www.britannica.com/science/anisotropy

Bartlett, J. L., & Li, X. (2019). An overview of residual stresses in metal powder bed fusion. *Additive Manufacturing*, *27*, 131–149. https://doi.org/10.1016/j.addma.2019.02.020

Berman, J. J. (2018). Indispensable Tips for Fast and Simple Big Data Analysis. *Principles and Practice of Big Data*, 231–257. https://doi.org/10.1016/b978-0-12-815609-4.00011-x

Bhuvanesh Kumar, M., & Sathiya, P. (2021). Methods and materials for additive manufacturing: A critical review on advancements and challenges. *Thin-Walled Structures*, *159*(October 2020), 107228. https://doi.org/10.1016/j.tws.2020.107228

Blakey-Milner, B., Gradl, P., Snedden, G., Brooks, M., Pitot, J., Lopez, E., Leary, M., Berto, F., & du Plessis, A. (2021). Metal additive manufacturing in aerospace: A review. *Materials and Design*, *209*, 110008. https://doi.org/10.1016/j.matdes.2021.110008

Calignano, F., Galati, M., & Iuliano, L. (2019). A metal powder bed fusion process in industry: Qualification considerations. *Machines*, *7*(4). https://doi.org/10.3390/machines7040072

Calignano, F., & Minetola, P. (2019). Accuracy , Roughness , and Support Structures of. *Materials*, *12*, 1–10.

Çalışkan, C. İ., Özer, G., Coşkun, M., & Koç, E. (2021). Investigation of direct metal laser sintering downskin parameters' sagging effect on microchannels. *International Journal of Advanced Manufacturing Technology*, *114*(9–10), 2567–

2575. https://doi.org/10.1007/s00170-021-07057-8

Charles, A., Bayat, M., Elkaseer, A., Thijs, L., Hattel, J. H., & Scholz, S. (2021). Elucidation of dross formation in laser powder bed fusion at down-facing surfaces: phenomenon-oriented multiphysics simulation and experimental validation. *Additive Manufacturing*, *50*(July 2021), 102551. https://doi.org/10.1016/j.addma.2021.102551

Charles, A., Elkaseer, A., Paggi, U., Thijs, L., Hagenmeyer, V., & Scholz, S. (2021). Down-facing surfaces in laser powder bed fusion of Ti6Al4V: Effect of dross formation on dimensional accuracy and surface texture. *Additive Manufacturing*, *46*(June), 102148. https://doi.org/10.1016/j.addma.2021.102148

Charles, A., Elkaseer, A., Thijs, L., Hagenmeyer, V., & Scholz, S. (2019). Effect of process parameters on the generated surface roughness of down-facing surfaces in selective laser melting. *Applied Sciences (Switzerland)*, *9*(6), 1–13. https://doi.org/10.3390/app9061256

Criales, L. E., Arısoy, Y. M., Lane, B., Moylan, S., Donmez, A., & Özel, T. (2017). Laser powder bed fusion of nickel alloy 625: Experimental investigations of effects of process parameters on melt pool size and shape with spatter analysis. *International Journal of Machine Tools and Manufacture*, *121*(March), 22–36. https://doi.org/10.1016/j.ijmachtools.2017.03.004

Danjoux, R. (2008). *Window and External Optics Transmittance Window and External Optics Transmittance*. 1–9.

DebRoy, T., Wei, H. L., Zuback, J. S., Mukherjee, T., Elmer, J. W., Milewski, J. O., Beese, A. M., Wilson-Heid, A., De, A., & Zhang, W. (2018). Additive manufacturing of metallic components – Process, structure and properties. *Progress in Materials Science*, *92*, 112–224. https://doi.org/10.1016/j.pmatsci.2017.10.001

DePond, P. J., Guss, G., Ly, S., Calta, N. P., Deane, D., Khairallah, S., & Matthews, M. J. (2018). In situ measurements of layer roughness during laser powder bed fusion additive manufacturing using low coherence scanning interferometry. *Materials and Design*, *154*, 347–359. https://doi.org/10.1016/j.matdes.2018.05.050

Eskandari Sabzi, H. (2019). Powder bed fusion additive layer manufacturing of titanium alloys. *Materials Science and Technology (United Kingdom)*, *35*(8), 875–890. https://doi.org/10.1080/02670836.2019.1602974

Feng, S., Kamat, A. M., Sabooni, S., & Pei, Y. (2021). Experimental and numerical investigation of the origin of surface roughness in laser powder bed fused

overhang regions. *Virtual and Physical Prototyping*, *16*(S1), S66–S84. https://doi.org/10.1080/17452759.2021.1896970

Fleming, T. G., Nestor, S. G. L., Allen, T. R., Boukhaled, M. A., Smith, N. J., & Fraser, J. M. (2020). Tracking and controlling the morphology evolution of 3D powder-bed fusion in situ using inline coherent imaging. *Additive Manufacturing*, *32*, 100978. https://doi.org/10.1016/j.addma.2019.100978

Foster, S. J., Carver, K., Dinwiddie, R. B., List, F., Unocic, K. A., Chaudhary, A., & Babu, S. S. (2018). Process-Defect-Structure-Property Correlations During Laser Powder Bed Fusion of Alloy 718: Role of In Situ and Ex Situ Characterizations. *Metallurgical and Materials Transactions A: Physical Metallurgy and Materials Science*, *49*(11), 5775–5798. https://doi.org/10.1007/s11661-018-4870-2

Fox, J. C., Moylan, S. P., & Lane, B. M. (2016). Effect of Process Parameters on the Surface Roughness of Overhanging Structures in Laser Powder Bed Fusion Additive Manufacturing. *Procedia CIRP*, *45*, 131–134. https://doi.org/10.1016/j.procir.2016.02.347

Gao, W., Zhang, Y., Ramanujan, D., Ramani, K., Chen, Y., Williams, C. B., Wang, C. C. L., Shin, Y. C., Zhang, S., & Zavattieri, P. D. (2015). The status, challenges, and future of additive manufacturing in engineering. *CAD Computer Aided Design*, *69*, 65–89. https://doi.org/10.1016/j.cad.2015.04.001

Gibson, I., Rosen, D., & Stucker, B. (2015). *Additive Manufacturing Technologies* (Second). Springer New York. https://doi.org/10.1007/978-1-4939-2113-3

Grasso, M., & Colosimo, B. M. (2017). Process defects and in situ monitoring methods in metal powder bed fusion: A review. *Measurement Science and Technology*, *28*(4), 0–40. https://doi.org/10.1088/1361-6501/aa5c4f

Gunenthiram, V., Peyre, P., Schneider, M., Dal, M., Coste, F., Koutiri, I., & Fabbro, R. (2018). Experimental analysis of spatter generation and melt-pool behavior during the powder bed laser beam melting process. *Journal of Materials Processing Technology*, *251*, 376–386. https://doi.org/10.1016/j.jmatprotec.2017.08.012

Guo, C., Li, S., Shi, S., Li, X., Hu, X., Zhu, Q., & Ward, R. M. (2020). Effect of processing parameters on surface roughness, porosity and cracking of as-built IN738LC parts fabricated by laser powder bed fusion. *Journal of Materials Processing Technology*, *285*(May), 116788. https://doi.org/10.1016/j.jmatprotec.2020.116788

Herzog, D., Seyda, V., Wycisk, E., & Emmelmann, C. (2016). Additive

manufacturing of metals. *Acta Materialia*, *117*, 371–392. https://doi.org/10.1016/j.actamat.2016.07.019

Hettiarachchi, B. D., Brandenburg, M., & Seuring, S. (2022). Connecting additive manufacturing to circular economy implementation strategies: Links, contingencies and causal loops. *International Journal of Production Economics*, *246*(September 2020), 108414. https://doi.org/10.1016/j.ijpe.2022.108414

Hooper, P. A. (2018). Melt pool temperature and cooling rates in laser powder bed fusion. *Additive Manufacturing*, *22*, 548–559. https://doi.org/10.1016/j.addma.2018.05.032

Infrared Imaging. (2012). https://www.vision-systems.com/cameras-accessories/image-sensors/article/16737868/infrared-imaging-superframing-increases-the-dynamic-range-of-thermal-imagers

Keyence. (n.d.). *Introduction to Surface Roughness Measurement*. https://sernia.ru/upload/pdf_files/Introduction to surface roughness measurement.pdf

Kirch, W. (2008). Hygienic Hand Disinfection, Hygienic hand disinfection. In *Encyclopedia of Public Health*.

Knaak, C., Masseling, L., Duong, E., Abels, P., & Gillner, A. (2021). Improving Build Quality in Laser Powder Bed Fusion Using High Dynamic Range Imaging and Model-Based Reinforcement Learning. *IEEE Access*, *9*, 55214–55231. https://doi.org/10.1109/ACCESS.2021.3067302

Koutiri, I., Pessard, E., Peyre, P., Amlou, O., & De Terris, T. (2018). Influence of SLM process parameters on the surface finish, porosity rate and fatigue behavior of as-built Inconel 625 parts. *Journal of Materials Processing Technology*, *255*(December 2017), 536–546. https://doi.org/10.1016/j.jmatprotec.2017.12.043

Kurzynowski, T., Chlebus, E., Kuźnicka, B., & Reiner, J. (2012). Parameters in selective laser melting for processing metallic powders. *High Power Laser Materials Processing: Lasers, Beam Delivery, Diagnostics, and Applications*, *8239*(October 2014), 823914. https://doi.org/10.1117/12.907292

Lancashire, H. T. (2017). *A simulated comparison between profile and areal surface parameters: R_a as an estimate of S_a*. 1–9.

Lane, B., Moylan, S., Whitenton, E. P., & Ma, L. (2016). Thermographic measurements of the commercial laser powder bed fusion process at NIST. *Rapid Prototyping Journal*, *22*(5), 778–787. https://doi.org/10.1108/RPJ-11-2015-0161

Leach, R. (2013). Characterisation of areal surface texture. In *Characterisation of Areal Surface Texture* (Vol. 9783642364). https://doi.org/10.1007/978-3-642-36458-7

Mahmoudi, M., Ezzat, A. A., & Elwany, A. (2019). Layerwise Anomaly Detection in Laser Powder-Bed Fusion Metal Additive Manufacturing. *Journal of Manufacturing Science and Engineering, Transactions of the ASME*, *141*(3), 1–21. https://doi.org/10.1115/1.4042108

Malekipour, E., & El-Mounayri, H. (2018). Common defects and contributing parameters in powder bed fusion AM process and their classification for online monitoring and control: a review. *International Journal of Advanced Manufacturing Technology*, *95*(1–4), 527–550. https://doi.org/10.1007/s00170-017-1172-6

Mandache, C. (2019). Overview of non-destructive evaluation techniques for metal-based additive manufacturing. *Materials Science and Technology (United Kingdom)*, *35*(9), 1007–1015. https://doi.org/10.1080/02670836.2019.1596370

Metelkova, J., Formanoir, C. De, Haitjema, H., Witvrouw, A., Pfleging, W., & Hooreweder, B. Van. (2019). Elevated edges of metal parts produced by laser powder bed fusion : characterization and post-process correction. *Proceedings of the Special Interest Group Meeting on Advancing Precision in Additive Manufacturing*, *September*, 1–4.

Milewski, J. O. (2017). Additive Manufacturing of Metals. In *Springer: Vol. Volume 258*. Springer. https://doi.org/10.1007/978-3-319-58205-4

Mohammadi, M., & Asgari, H. (2018). Achieving low surface roughness AlSi10Mg_200C parts using direct metal laser sintering. *Additive Manufacturing*, *20*, 23–32. https://doi.org/10.1016/j.addma.2017.12.012

Mohr, G., Altenburg, S. J., Ulbricht, A., Heinrich, P., Baum, D., Maierhofer, C., & Hilgenberg, K. (2020). In-situ defect detection in laser powder bed fusion by using thermography and optical tomography—comparison to computed tomography. *Metals*, *10*(1). https://doi.org/10.3390/met10010103

Mohr, G., Nowakowski, S., Altenburg, S. J., Maierhofer, C., & Hilgenberg, K. (2020). Experimental determination of the emissivity of powder layers and bulk material in laser powder bed fusion using infrared thermography and thermocouples. *Metals*, *10*(11), 1–36. https://doi.org/10.3390/met10111546

Mumtaz, K., & Hopkinson, N. (2009). Top surface and side roughness of Inconel 625 parts processed using selective laser melting. *Rapid Prototyping Journal*, *15*(2), 96–103. https://doi.org/10.1108/13552540910943397

Olympus. (n.d.). *Surface Roughness Measurement*. https://www.olympus-ims.com/ru/metrology/surface-roughness-measurement-portal/parameters/#!cms%5Bfocus%5D=022

Profillidis, V. A., & Botzoris, G. N. (2019). Statistical Methods for Transport Demand Modeling. In *Modeling of Transport Demand*. https://doi.org/10.1016/b978-0-12-811513-8.00005-4

Research and Markets. (n.d.). *Additive Manufacturing Market Analysis By Material Type, By Metal Type, By Polymer Type, By Ceramics Type, By Process, By End-use, And Segment Forecasts To 2027*. https://www.researchandmarkets.com/reports/5206602/additive-manufacturing-market-analysis-by?utm_source=BW&utm_medium=PressRelease&utm_code=psl56x&utm_campaign=1479598+-+%2423.75+Billion+Additive+Manufacturing+Market+Analysis%2C+2020-2027&utm_exec=chdo54p

Rott, S., Ladewig, A., Friedberger, K., Casper, J., Full, M., & Schleifenbaum, J. H. (2020). Surface roughness in laser powder bed fusion – Interdependency of surface orientation and laser incidence. *Additive Manufacturing*, *36*(July), 101437. https://doi.org/10.1016/j.addma.2020.101437

Sahay, C., & Ghosh, S. (2018). Understanding surface quality: Beyond average roughness (Ra). *ASEE Annual Conference and Exposition, Conference Proceedings*, *2018-June*. https://doi.org/10.18260/1-2--31176

Schoinochoritis, B., Chantzis, D., & Salonitis, K. (2017). Simulation of metallic powder bed additive manufacturing processes with the finite element method: A critical review. *Proceedings of the Institution of Mechanical Engineers, Part B: Journal of Engineering Manufacture*, *231*(1), 96–117. https://doi.org/10.1177/0954405414567522

Scime, L., & Beuth, J. (2019). Using machine learning to identify in-situ melt pool signatures indicative of flaw formation in a laser powder bed fusion additive manufacturing process. *Additive Manufacturing*, *25*, 151–165. https://doi.org/10.1016/j.addma.2018.11.010

Seabra, M., Azevedo, J., Araújo, A., Reis, L., Pinto, E., Alves, N., Santos, R., & Pedro Mortágua, J. (2016). Selective laser melting (SLM) and topology optimization for lighter aerospace componentes. *Procedia Structural Integrity*, *1*, 289–296. https://doi.org/10.1016/j.prostr.2016.02.039

Simoni, F., Huxol, A., & Villmer, F. J. (2021). Improving surface quality in selective

laser melting based tool making. *Journal of Intelligent Manufacturing*, *32*(7), 1927–1938. https://doi.org/10.1007/s10845-021-01744-9

Skalon, M., Meier, B., Gruberbauer, A., Amancio-Filho, S. T., & Sommitsch, C. (2020). Stability of a melt pool during 3D-Printing of an unsupported steel component and its influence on roughness. *Materials*, *13*(3), 1–14. https://doi.org/10.3390/ma13030808

Tan, C., Weng, F., Sui, S., Chew, Y., & Bi, G. (2021). Progress and perspectives in laser additive manufacturing of key aeroengine materials. *International Journal of Machine Tools and Manufacture*, *170*(September), 103804. https://doi.org/10.1016/j.ijmachtools.2021.103804

Teledyne. (2021). *How Does Emissivity Affect Thermal Imaging?* https://www.flir.com/discover/professional-tools/how-does-emissivity-affect-thermal-imaging/

Wiberg, A. (2019). Towards Design Automation for Additive Manufacturing A Multidisciplinary Optimization approach Anton Wiberg FACULTY OF SCIENCE AND ENGINEERING. In *Linköping Studies in Science*.

Wohlers, T. T., Campbell, I., Caffrey, T., Diegel, O., & Kowen, J. (2018). 3D Printing and Additive Manufacturing State of the Industry: Annual Worldwide Progress Report. In 2018 Wohlers Associates (Ed.), *Wohlers Report*.

Yakout, M., Elbestawi, M. A., & Veldhuis, S. C. (2018). A review of metal additive manufacturing technologies. *Solid State Phenomena*, *278 SSP*(July), 1–14. https://doi.org/10.4028/www.scientific.net/SSP.278.1

Yan, X., Gao, S., Chang, C., Huang, J., Khanlari, K., Dong, D., Ma, W., Fenineche, N., Liao, H., & Liu, M. (2021). Effect of building directions on the surface roughness, microstructure, and tribological properties of selective laser melted Inconel 625. *Journal of Materials Processing Technology*, *288*(January 2020), 116878. https://doi.org/10.1016/j.jmatprotec.2020.116878

Yang, T., Liu, T., Liao, W., Wei, H., Zhang, C., Chen, X., & Zhang, K. (2021). Effect of processing parameters on overhanging surface roughness during laser powder bed fusion of AlSi10Mg. *Journal of Manufacturing Processes*, *61*(November 2020), 440–453. https://doi.org/10.1016/j.jmapro.2020.11.030

Yasa, E., Poyraz, O., Solakoglu, E. U., Akbulut, G., & Oren, S. (2016). A Study on the Stair Stepping Effect in Direct Metal Laser Sintering of a Nickel-based Superalloy. *Procedia CIRP*, *45*, 175–178. https://doi.org/10.1016/j.procir.2016.02.068

Yin, J., Wang, D., Yang, L., Wei, H., Dong, P., Ke, L., Wang, G., Zhu, H., & Zeng, X. (2020). Correlation between forming quality and spatter dynamics in laser powder bed fusion. *Additive Manufacturing*, *31*(September 2019), 100958. https://doi.org/10.1016/j.addma.2019.100958

A Appendix A – MATLAB Scripts

An extract of the adopted MATLAB codes is reported in the Appendix to illustrate the followed procedure. Section A.1. regards the scripts used to analyze the roughness dataset, including the cleaning phase, and the extrapolation of the parameters. Instead, the scripts exploited for the thermal dataset are depicted in Section A.2.

A.1. Ex-Situ Scripts

Scripts to clean ex-situ dataset and calculate parameters (to repeat for each specimen)

```
clear all
close all
clc

oh_15_6col=importdata(oh_15_CC.txt'); %import clean file from CloudCompare
for i=1:3
   oh_15(:,i)= oh_15_6col (:,i); %select 3 coordinates, no info on colors
end
clean = oh_15;
coords = [clean(:,1),clean(:,2),clean(:,3)];
avgCoords = mean(coords);
coordsCentered = coords - avgCoords;

%% fit plane
pc = pointCloud(coordsCentered);
model = pcfitplane(pc,100);
figure
pcshow(pc)
xlabel('X(um)')
ylabel('Y(um)')
```

```
zlabel('Z(um)')
title('Plane fit on original figure')

%% fit LS plane
A = [coordsCentered(:,1), coordsCentered(:,2), ones(length(coordsCentered),1)];
Z = coordsCentered(:,3);
coeff = A\Z;
coeff = [-coeff(1); -coeff(2); 1; -coeff(3)];
Parameters = [coeff(1:3)/sqrt(coeff(1)^2+coeff(2)^2+coeff(3)^2); coeff(4)];
modelLS = planeModel(Parameters);
hold on
plot(modelLS)

%% transform pc
referenceVector = [0 0 1];
tform = normalRotation(modelLS,referenceVector);
ptCloudOut = pctransform(pc,tform);

%% fit LS plane on rotated pc
coordsCentered = ptCloudOut.Location;
A = [coordsCentered(:,1), coordsCentered(:,2), ones(length(coordsCentered),1)];
Z = coordsCentered(:,3);
coeff = A\Z;
coeff = [-coeff(1); -coeff(2); 1; -coeff(3)];
Parameters = [coeff(1:3)/sqrt(coeff(1)^2+coeff(2)^2+coeff(3)^2); coeff(4)];
modelLStr = planeModel(Parameters);
hold on
plot(modelLStr)

%% translate/rotate pointCloud in right origin
rotated(:,:) = ptCloudOut.Location(:,:);
ptCloud = pointCloud(rotated);
ptCloudOutTrans = trans_final(ptCloud.Location,ptCloud);

rad_zrot = pi;
ptCloudOutRot = rot_z(rad_zrot, ptCloudOutTrans);
```

```
clean = ptCloudOutRot.Location;
figure
scatter3(clean(:,1),clean(:,2),clean(:,3),5,clean(:,3),'.')
colorbar
caxis([-150 150])
title('Final total dataset')
xlabel("X' ")
ylabel("Y' ")
zlabel("Z' ")
lenght_x=max(clean(:,1))
lenght_y=max(clean(:,2))
lenght_z=max(clean(:,3))-min(clean(:,3))

%% divide specimens in grid ndiv x ndiv
ndiv = 5;
l_x=(max(clean(:,1)))-(min(clean(:,1)))
lpiece_x=l_x/ndiv
min_vx=zeros(ndiv,1);
min_vx(1,1)=min(clean(:,1))
minx = min_vx(1,1)
maxx=max(clean(:,1))
k=1; j=1;

% first divide in lines
while min_vx(j,1)<maxx % j counts the x lines
   minx=minx + lpiece_x;
   for i=1:size(clean,1) % i counts all points
      if clean(i,1) < minx && clean(i,1) >= (minx-lpiece_x)
         line_act(k,:)=clean(i,:); % k counts all points that enter if
         xline(j).vv(k,:)=line_act(k,:);
         k=k+1;
      end
   end
   k=1; j=j+1;
   min_vx(j,1)=minx;
end
```

```
l_y=(max(clean(:,2)))-(min(clean(:,2)))
lpiece_y=l_y/ndiv
min_vy=zeros(ndiv,1);
min_vy(1,1)=min(clean(:,2)) % vector of ndiv minima
miny = min_vy(1,1) % first minimum
maxy=max(clean(:,2)) % maximum
j=1;k=1;n=1;

% then divide in squares
for m=1:size(xline,2)
   while min_vy(j,1)<maxy % j da 1 a 10
      miny=miny + lpiece_y;
      for i=1:size(xline(m).vv,1)
         if xline(m).vv(i,2) < miny && xline(m).vv(i,2) >= (miny-lpiece_y)
            sq_act(k,:)=xline(m).vv(i,:); %to save points of line in 1 sq
            l(m).sq(j).c(k,:)=sq_act(k,:);
                  % line info, square info and coordinates
            k=k+1;
         end
      end
      k=1;j=j+1;
      min_vy(j,1)=miny;
   end
   min_vy=zeros(ndiv,1);
   min_vy(1,1)=min(clean(:,2)); % vector of ndiv minima
   miny = min_vy(1,1); % first minimum
   j=1;
end

%% represent squares in graphs
k=1; m=2;
figure
for i=1:ndiv
   for j=1:ceil((ndiv)/2)
      if floor(i/2)*2~=i && j<= ceil(ndiv/2)
         scatter3(l(i).sq(k).c(:,1),l(i).sq(k).c(:,2),l(i).sq(k).c(:,3), '.');
         colorbar
```

```
            caxis([-150 150])
            hold on
            title('Plot of squares - start from 1 (view XZ)')
            xlabel("X' ")
            ylabel("Y' ")
            zlabel("Z' ")
            view(0,90)
            k=k+2;

        elseif floor(i/2)*2==i && j<= floor(ndiv/2)
            scatter3(l(i).sq(m).c(:,1),l(i).sq(m).c(:,2),l(i).sq(m).c(:,3), '.');
            colorbar
            caxis([-150 150])
            view(0,90)
            m=m+2;
        end
    end
    m=2; k=1;
end

%% calculate parameters
k=1;
for i=1:ndiv
    for j=1:ndiv
        l(i).s(j).yinfo = j;
        l(i).s(j).xinfo = i;
        % Move z-data to the average line.
        l(i).s(j).zavg=l(i).sq (j).c(:,3) mean(l(i).sq(j).c(:,3),'omitnan');
        % Sa - arithmetical mean height
        l(i).s(j).Sa=mean(abs(l(i).s(j).zavg),'omitnan');
        Sa(k,1)=l(i).s(j).Sa;
        % Sq - root mean square
        l(i).s(j).Sq=rms(l(i).s(j).zavg,'omitnan');
        % Sv - maximum pit height
        l(i).s(j).Sv=abs(min(l(i).s(j).zavg,[],'omitnan'));
        % Sp - maximum peak height
        l(i).s(j).Sp=abs(max(l(i).s(j).zavg,[],'omitnan'));
```

```
        % Sz - maximum height of the surface
        l(i).s(j).Sz=l(i).s(j).Sp+l(i).s(j).Sv;
        k=k+1;
    end
end

%% represent individual plots of Sa
clear xline
k=1;
for i=1:ndiv
    for j=1:ndiv
        matrix_Sa(k,i)=l(i).s(j).Sa;
        k=k+1;
    end
    avg_line_Sa(1,i)= mean(matrix_Sa(1:k-1,i));
    k=1;
end
k=1;
for i=1:ndiv
    for j=1:ndiv
        vector_Sa(k,1)=l(i).s(j).Sa;
        k=k+1;
    end
end
mean_Sa = mean(vector_Sa);

degree=15; % oh specimen
individual_plot_Sa_5_xprime(l,ndiv,avg_line_Sa,degree)
individual_plot_Sa_5_yprime(l,ndiv,avg_line_Sa,degree)
```

A.2. Ex-Situ Scripts

Scripts to clean in-situ dataset and calculate coordinates of pixels and TAT = 500 K (to repeat for each thermal video)

```
imtool close all
```

```
close all
clear all
clc

load('frames_c_000014_OH15.mat')
frames_c_15=frames_c;
load('frames_c_000014_OH30.mat')
frames_c_30=frames_c;
load('frames_c_000014_OH45.mat')
frames_c_45=frames_c;
load('frames_c_000014_OH50.mat')
frames_c_50=frames_c;
clear frames_c

%% obtain contour of specimens
d=3; %distance from overhang
clean_thresh = 600;
pos_15 = zeros(size(frames_c_15,1,2)); % 2D, it is 1 frame only
for i=1:size(frames_c_15,1)
    for j=1:size(frames_c_15,2)
        pos_thist = find(frames_c_15(i,j,:)>clean_thresh,1);
        if ~isempty(pos_thist)
            pos_15(i,j) = pos_thist;
        end
    end
end

pos_30 = zeros(size(frames_c_30,1,2));
for i=1:size(frames_c_30,1)
    for j=1:size(frames_c_30,2)
        pos_thist = find(frames_c_30(i,j,:)>clean_thresh,1);
        if ~isempty(pos_thist)
            pos_30(i,j) = pos_thist;
        end
    end
end
```

```
pos_45 = zeros(size(frames_c_45,1,2));
for i=1:size(frames_c_45,1)
   for j=1:size(frames_c_45,2)
      pos_thist = find(frames_c_45(i,j,:)>clean_thresh,1);
      if ~isempty(pos_thist)
         pos_45(i,j) = pos_thist;
      end
   end
end

pos_50 = zeros(size(frames_c_50,1,2));
for i=1:size(frames_c_50,1)
   for j=1:size(frames_c_50,2)
      pos_thist = find(frames_c_50(i,j,:)>clean_thresh,1);
      if ~isempty(pos_thist)
         pos_50(i,j) = pos_thist;
      end
   end
end

%% clean single layers outlines and save coordinates of pixels
pos_bw_15=imbinarize(pos_15);
SE=strel('square',5);
close(:,:,1)=imclose(pos_bw_15,SE);
open(:,:,1)=imopen(close(:,:,1),SE);
[L,N]=bwlabel(open(:,:,1));
stats=regionprops('table',open(:,:,1),'Area','BoundingBox','Centroid');
idx=find([stats.Area]>450);
area(1)=stats.Area(idx);
new(:,:,1)=1-(imbinarize(im2double(im2gray(label2rgb(ismember(L,idx))))));
imtool(new(:,:,1),[])
mid_y(1,:)=round(stats.Centroid(idx,2));
mid_x_r(1,:)=round(stats.Centroid(idx,1)+(stats.BoundingBox(idx,3)/2))-d;
mid_x_l(1,:)=round(stats.Centroid(idx,1)-(stats.BoundingBox(idx,3)/2))+d;
mid_x(1,:)=round(stats.Centroid(idx,1));
mid_y_b(1,:)=round(stats.Centroid(idx,2)+(stats.BoundingBox(idx,4)/2))-d;
mid_y_t(1,:)=round(stats.Centroid(idx,2)-(stats.BoundingBox(idx,4)/2))+d;
```

```
pos_bw_30=imbinarize(pos_30);
SE=strel('square',5);
close(:,:,2)=imclose(pos_bw_30,SE);
open(:,:,2)=imopen(close(:,:,2),SE);
[L,N]=bwlabel(open(:,:,2));
stats=regionprops('table',open(:,:,2),'Area','BoundingBox','Centroid');
idx=find([stats.Area]>500);
area(1)=stats.Area(idx);
new(:,:,2)=1-(imbinarize(im2double(im2gray(label2rgb(ismember(L,idx))))));
imtool(new(:,:,2),[])
mid_y(2,:)=round(stats.Centroid(idx,2));
mid_x_r(2,:)=round(stats.Centroid(idx,1)+(stats.BoundingBox(idx,3)/2))-d;
mid_x_l(2,:)=round(stats.Centroid(idx,1)-(stats.BoundingBox(idx,3)/2))+d;
mid_x(2,:)=round(stats.Centroid(idx,1));
mid_y_b(2,:)=round(stats.Centroid(idx,2)+(stats.BoundingBox(idx,4)/2))-d;
mid_y_t(2,:)=round(stats.Centroid(idx,2)-(stats.BoundingBox(idx,4)/2))+d;

pos_bw_45=imbinarize(pos_45);
SE=strel('square',5);
close(:,:,3)=imclose(pos_bw_45,SE);
open(:,:,3)=imopen(close(:,:,3),SE);
[L,N]=bwlabel(open(:,:,3));
stats=regionprops('table',open(:,:,3),'Area','BoundingBox','Centroid');
idx=find([stats.Area]>500);
area(1)=stats.Area(idx);
new(:,:,3)=1-(imbinarize(im2double(im2gray(label2rgb(ismember(L,idx))))));
imtool(new(:,:,3),[])
mid_y(3,:)=round(stats.Centroid(idx,2));
mid_x_r(3,:)=round(stats.Centroid(idx,1)+(stats.BoundingBox(idx,3)/2))-d;
mid_x_l(3,:)=round(stats.Centroid(idx,1)-(stats.BoundingBox(idx,3)/2))+d;
mid_x(3,:)=round(stats.Centroid(idx,1));
mid_y_b(3,:)=round(stats.Centroid(idx,2)+(stats.BoundingBox(idx,4)/2))-2;
mid_y_t(3,:)=round(stats.Centroid(idx,2)-(stats.BoundingBox(idx,4)/2))+2;

pos_bw_50=imbinarize(pos_50);
SE=strel('square',5);
```

```
close(:,:,4)=imclose(pos_bw_50,SE);
open(:,:,4)=imopen(close(:,:,4),SE);
[L,N]=bwlabel(open(:,:,4));
stats=regionprops('table',open(:,:,4),'Area','BoundingBox','Centroid');
idx=find([stats.Area]>500);
area(1)=stats.Area(idx);
new(:,:,4)=1-(imbinarize(im2double(im2gray(label2rgb(ismember(L,idx))))));
imtool(new(:,:,4),[])
mid_y(4,:)=round(stats.Centroid(idx,2));
mid_x_r(4,:)=round(stats.Centroid(idx,1)+(stats.BoundingBox(idx,3)/2))-d;
mid_x_l(4,:)=round(stats.Centroid(idx,1)-(stats.BoundingBox(idx,3)/2))+d;
mid_x(4,:)=round(stats.Centroid(idx,1));
mid_y_b(4,:)=round(stats.Centroid(idx,2)+(stats.BoundingBox(idx,4)/2))-d;
mid_y_t(4,:)=round(stats.Centroid(idx,2)-(stats.BoundingBox(idx,4)/2))+d;

%% represent cleaned contours in image
for i=1:size(new,1)
   for j=1:size(new,2)
      if new(i,j,1)==1 || new(i,j,2)==1 || new(i,j,3)==1 || new(i,j,4)==1
         tot(i,j)=1;
      else
         tot(i,j)=0;
      end
   end
end
imtool(tot)

%% pixel visualization
oh15 =1; oh30=2; oh45=3; oh50=4;
for k=1:size(frames_c_15,3)-1
   pix_r(1,k)=frames_c_15(mid_y(oh15,:),mid_x_r(oh15,:),k);
   pix_l(1,k)=frames_c_15(mid_y(oh15,:),mid_x_l(oh15,:),k);
   pix_t(1,k)=frames_c_15(mid_y_t(oh15,:),mid_x(oh15,:),k);
   pix_b(1,k)=frames_c_15(mid_y_b(oh15,:),mid_x(oh15,:),k);
end

for k=1:size(frames_c_30,3)-1
```

```
    pix_r(2,k)=frames_c_30(mid_y(oh30,:),mid_x_r(oh30,:),k);
    pix_l(2,k)=frames_c_30(mid_y(oh30,:),mid_x_l(oh30,:),k);
    pix_t(2,k)=frames_c_30(mid_y_t(oh30,:),mid_x(oh30,:),k);
    pix_b(2,k)=frames_c_30(mid_y_b(oh30,:),mid_x(oh30,:),k);
end

for k=1:size(frames_c_45,3)-1
    pix_r(3,k)=frames_c_45(mid_y(oh45,:),mid_x_r(oh45,:),k);
    pix_l(3,k)=frames_c_45(mid_y(oh45,:),mid_x_l(oh45,:),k);
    pix_t(3,k)=frames_c_45(mid_y_t(oh45,:),mid_x(oh45,:),k);
    pix_b(3,k)=frames_c_45(mid_y_b(oh45,:),mid_x(oh45,:),k);
end

for k=1:size(frames_c_50,3)-1
    pix_r(4,k)=frames_c_50(mid_y(oh50,:),mid_x_r(oh50,:),k);
    pix_l(4,k)=frames_c_50(mid_y(oh50,:),mid_x_l(oh50,:),k);
    pix_t(4,k)=frames_c_50(mid_y_t(4,:),mid_x(oh50,:),k);
    pix_b(4,k)=frames_c_50(mid_y_b(4,:),mid_x(oh50,:),k);
end

pixel_oh15 = [pix_b(oh15,:); pix_r(oh15,:); pix_l(oh15,:); pix_t(oh15,:)];
pixel_oh30 = [pix_b(oh30,:); pix_r(oh30,:); pix_l(oh30,:); pix_t(oh30,:)];
pixel_oh45 = [pix_b(oh45,:); pix_r(oh45,:); pix_l(oh45,:); pix_t(oh45,:)];
pixel_oh50 = [pix_b(oh50,:); pix_r(oh50,:); pix_l(oh50,:); pix_t(oh50,:)];

%% peak allignment for each OH
% oh15
for j=1:size(pixel_oh15,1)
    [val_oh(j),array_oh(oh15,j)]=max(pixel_oh15(j,:));
end
[M_pk,I_oh]=max(array_oh(oh15,:));
for i=1:4
    diff_oh(oh15,i)=array_oh(oh15,I_oh)-array_oh(oh15,i);
    single_oh = [zeros(1, diff_oh(oh15,i)), pixel_oh15(i,:)];
    pixel_pk_oh15(i,1:size(single_oh,2)) = single_oh;
end
% oh30
```

```
for j=1:size(pixel_oh30,1)
    [val_oh(j),array_oh(oh30,j)]=max(pixel_oh30(j,:));
end
[M_pk,I_oh]=max(array_oh(oh30,:));
for i=1:4
    diff_oh(oh30,i)=array_oh(oh30,I_oh)-array_oh(oh30,i);
    single_oh = [zeros(1, diff_oh(oh30,i)), pixel_oh30(i,:)];
    pixel_pk_oh30(i,1:size(single_oh,2)) = single_oh;
end
% oh45
for j=1:size(pixel_oh45,1)
    [val_oh(j),array_oh(oh45,j)]=max(pixel_oh45(j,:));
end
[M_pk,I_oh]=max(array_oh(oh45,:));
for i=1:4
    diff_oh(oh45,i)=array_oh(oh45,I_oh)-array_oh(oh45,i);
    single_oh = [zeros(1, diff_oh(oh45,i)), pixel_oh45(i,:)];
    pixel_pk_oh45(i,1:size(single_oh,2)) = single_oh;
end
% oh50
for j=1:size(pixel_oh50,1)
    [val_oh(j),array_oh(oh50,j)]=max(pixel_oh50(j,:));
end
[M_pk,I_oh]=max(array_oh(oh50,:));
for i=1:4
    diff_oh(oh50,i)=array_oh(oh50,I_oh)-array_oh(oh50,i);
    single_oh = [zeros(1, diff_oh(oh50,i)), pixel_oh50(i,:)];
    pixel_pk_oh50(i,1:size(single_oh,2)) = single_oh;
end

%% represent graphs aligned to pixel, b = bottom, r = right, l = left, t = top
b=1; r=2; l=3; t=4;

figure
subplot(2, 2, 1);
plot(pixel_pk_oh15(b,:)), hold on, plot(pixel_pk_oh15(r,:)), hold on, plot(pixel_pk_oh15(l,:)), hold on,
plot(pixel_pk_oh15(t,:))
```

```
hold on
title('OH15 pix'), xlabel('Frames'), ylabel('T [K]'), legend('B', 'R', 'L', 'T')

subplot(2, 2, 2);
plot(pixel_pk_oh30(b,:)), hold on, plot(pixel_pk_oh30(r,:)), hold on, plot(pixel_pk_oh30(l,:)), hold on,
plot(pixel_pk_oh30(t,:))
hold on
title('OH30 pix'), xlabel('Frames'), ylabel('T [K]'), legend('B', 'R', 'L', 'T')

subplot(2, 2, 3);
plot(pixel_pk_oh45(b,:)), hold on, plot(pixel_pk_oh45(r,:)), hold on, plot(pixel_pk_oh45(l,:)), hold on,
plot(pixel_pk_oh45(t,:))
hold on
title('OH45 pix'), xlabel('Frames'), ylabel('T [K]'), legend('B', 'R', 'L', 'T')

subplot(2, 2, 4);
plot(pixel_pk_oh50(b,:)), hold on, plot(pixel_pk_oh50(r,:)), hold on, plot(pixel_pk_oh50(l,:)), hold on,
plot(pixel_pk_oh50(t,:))
hold on
title('OH50 pix'), xlabel('Frames'), ylabel('T [K]'), legend('B', 'R', 'L', 'T')

%% TAT CALCULATION
th1=500; % threshold 500 K for AISI316L and 200 K for AlSi10Mg
width=224; % 224 pixels for AISI316L and 192 for AlSi10Mg
height=72;
tat1_15 = zeros(height,width);
for k=1:size(frames_c_15,3)
   for i=1:size(new,1)
      for j=1:size(new,2)
         if new(i,j,1) ~= 0
            t_15(i,j,k) = frames_c_15(i,j,k);
         else
            t_15(i,j,k) = 0;
         end
      end
   end
   i=1; j=1;
```

```
end

tat1_30 = zeros(height,width);
for k=1:size(frames_c_30,3)
   for i=1:size(new,1)
      for j=1:size(new,2)
         if new(i,j,2) ~= 0
            t_30(i,j,k) = frames_c_30(i,j,k);
         else
            t_30(i,j,k) = 0;
         end
      end
   end
   i=1; j=1;
end

tat1_45 = zeros(height,width);
for k=1:size(frames_c_45,3)
   for i=1:size(new,1)
      for j=1:size(new,2)
         if new(i,j,3) ~= 0
            t_45(i,j,k) = frames_c_45(i,j,k);
         else
            t_45(i,j,k) = 0;
         end
      end
   end
   i=1; j=1;
end

tat1_50 = zeros(height,width);
for k=1:size(frames_c_50,3)
   for i=1:size(new,1)
      for j=1:size(new,2)
         if new(i,j,4) ~= 0
            t_50(i,j,k) = frames_c_50(i,j,k);
         else
```

```
            t_50(i,j,k) = 0;
          end
        end
      end
      i=1; j=1;
end

%Calculate moving mean of temp for each OH and use it as new matrix
for i = 1:size(t_15,1)
  for j = 1:size(t_15,2) % i and j along pixels
      for k=1:size(t_15,3) % k along frames
          col(k)=t_15(i,j,k);
      end
            col_mm=movmean(col,3); % move mean of step = 3
      for k=1:size(t_15,3)
          MMt_15(i,j,k)=col_mm(k);
      end
      clear col_mm col
    end
end

for i = 1:size(t_30,1)
  for j = 1:size(t_30,2)
      for k=1:size(t_30,3)
          col(k)=t_30(i,j,k);
      end
            col_mm=movmean(col,3);
      for k=1:size(t_30,3)
          MMt_30(i,j,k)=col_mm(k);
      end
      clear col_mm col
    end
end

for i = 1:size(t_45,1)
  for j = 1:size(t_45,2)
```

```
      for k=1:size(t_45,3)
         col(k)=t_45(i,j,k);
      end
           col_mm=movmean(col,3);
      for k=1:size(t_45,3)
         MMt_45(i,j,k)=col_mm(k);
      end
      clear col_mm col
   end
end

for i = 1:size(t_50,1)
  for j = 1:size(t_50,2)
      for k=1:size(t_50,3)
      for k=1:size(t_50,3)
         col(k)=t_50(i,j,k);
      end
           col_mm=movmean(col,3);
      for k=1:size(t_50,3)
         MMt_50(i,j,k)=col_mm(k);
      end
      clear col_mm col
   end
end

% Matrix for values above TH1 = 500 K (sequential) for each OH
fps= 667; % 667 fps for AISI316L and 500 fps for AlSi10Mg
% SPECIMEN 15°
x=1;
for i = 1:size(MMt_15,1)
  for j = 1:size(MMt_15,2)
      clear array
      array(1,1) = 0;
      for k=1:size(MMt_15,3)-1
         if MMt_15(i,j,k)>=th1
            array(x,1)=array(x,1)+1;
```

```
            array(x,2)=k;
            if MMt_15(i,j,k+1)<th1
               x=x+1;
               array(x,1)=0;
            end
         end
      end
      x=1;
      for k=1:size(array,1)-2
         array(k,3)=array(k+1,2)-array(k+1,1)-array(k,2);
      end
      tat1_15(i,j)=max(array(:,1));
   end
end
tat1_15(:,:) = (tat1_15(:,:)/fps)*1000; % in [ms]
k=1;
for i=1:size(tat1_15,1)
   for j=1:size(tat1_15,2)
      if tat1_15(i,j) ~= 0
         tat1_15_pop(k,:) = tat1_15(i,j);
         k=k+1;
      end
   end
end

% SPECIMEN 30°
x=1;
for i = 1:size(MMt_30,1)
  for j = 1:size(MMt_30,2)
      clear array
      array(1,1) = 0;
      for k=1:size(MMt_30,3)-1
         if MMt_30(i,j,k)>=th1
            array(x,1)=array(x,1)+1;
            array(x,2)=k;
            if MMt_30(i,j,k+1)<th1
               x=x+1;
```

```
            array(x,1)=0;
          end
        end
      end
      x=1;
      for k=1:size(array,1)-2
        array(k,3)=array(k+1,2)-array(k+1,1)-array(k,2);
      end
      tat1_30(i,j)=max(array(:,1));
    end
end
tat1_30(:,:) = (tat1_30(:,:)/fps)*1000; % in [ms]
k=1;
for i=1:size(tat1_30,1)
  for j=1:size(tat1_30,2)
    if tat1_30(i,j) ~= 0
      tat1_30_pop(k,:) = tat1_30(i,j);
      k=k+1;
    end
  end
end

% SPECIMEN 45°
x=1;
for i = 1:size(MMt_45,1)
  for j = 1:size(MMt_45,2) % i e j scorrono i pixel
    clear array
    array(1,1) = 0;
    for k=1:size(MMt_45,3)-1 % scorre i frames
      if MMt_45(i,j,k)>=th1
        array(x,1)=array(x,1)+1;
        array(x,2)=k;
        if MMt_45(i,j,k+1)<th1
          x=x+1;
          array(x,1)=0;
        end
      end
```

```
        end
        x=1;
        for k=1:size(array,1)-2
            array(k,3)=array(k+1,2)-array(k+1,1)-array(k,2);
        end
        tat1_45(i,j)=max(array(:,1));
    end
end
tat1_45(:,:) = (tat1_45(:,:)/fps)*1000; % in [ms]
k=1;
for i=1:size(tat1_45,1)
    for j=1:size(tat1_45,2)
        if tat1_45(i,j) ~= 0
            tat1_45_pop(k,:) = tat1_45(i,j);
            k=k+1;
        end
    end
end

% SPECIMEN 50°
x=1;
for i = 1:size(MMt_50,1)
  for j = 1:size(MMt_50,2) % i e j scorrono i pixel
        clear array
        array(1,1) = 0;
        for k=1:size(MMt_50,3)-1 % scorre i frames
            if MMt_50(i,j,k)>=th1
                array(x,1)=array(x,1)+1;
                array(x,2)=k;
                if MMt_50(i,j,k+1)<th1
                    x=x+1;
                    array(x,1)=0;
                end
            end
        end
        x=1;
        for k=1:size(array,1)-2
```

```
            array(k,3)=array(k+1,2)-array(k+1,1)-array(k,2);
        end
        tat1_50(i,j)=max(array(:,1));
    end
end
tat1_50(:,:) = (tat1_50(:,:)/fps)*1000; % in [ms]
k=1;
for i=1:size(tat1_50,1)
    for j=1:size(tat1_50,2)
        if tat1_50(i,j) ~= 0
            tat1_50_pop(k,:) = tat1_50(i,j);
            k=k+1;
        end
    end
end

%% choosing the right scale
M15 = ceil(max(tat1_15,[],'all'));
M30 = ceil(max(tat1_30,[],'all'));
M45 = ceil(max(tat1_45,[],'all'));
M50 = ceil(max(tat1_50,[],'all'));

Mtot = [M15, M30, M45, M50];
M_l3 = ceil(mean(Mtot));
M=400; % 400 K for AISI316L and 200 K for AlSi10Mg

% threshold 1 - clean (sequential)
for i=1:size(tat1_15,1)
    for j=1:size(tat1_15,2)
        if tat1_15(i,j)~=0
            tat1(i,j)=tat1_15(i,j);
        elseif tat1_30(i,j)~=0
            tat1(i,j)=tat1_30(i,j);
        elseif tat1_45(i,j)~=0
            tat1(i,j)=tat1_45(i,j);
        elseif tat1_50(i,j)~=0
            tat1(i,j)=tat1_50(i,j);
```

```
        else
            tat1(i,j)=0;
        end
    end
end
figure
image(tat1)
c = hot(M);
colormap(c)
colorbar
hold on
title(['All OH clean (sequential): TAT = ', num2str(th1), 'K']);
hold on
title(colorbar,'ms');
```

List of Figures

List of Tables

List of Symbols

Variable	Description	SI unit
Sa	Arithmetic mean height	µm
Sq	Square root version of Sa	µm
Sv	Height of the lowest point	µm
Sp	Height of the highest point	µm
TAT	Time Above Threshold	msec
OH	Overhang angle	°
E	Energy density	J/mm^2
P	Laser power	W
h	Hatch spacing	mm
v	Scan speed	mm/s
Te	Exposure time	µs
Pd	Point distance	µm

Acknowledgments

Firstly, we would like to thank Professor Bianca Maria Colosimo and PhD Candidate Matteo Bugatti who drove us through all the difficulties we found working on this thesis, sharing precious pieces of advice. A special mention goes to Add.Me laboratories that allowed us to get in contact with the tools and technologies that made possible the realization of our project.